THERMAL CONDUCTIVITY SWITCHING OF POLYMERS AND LITHIUM-ION BATTERY ELECTRODE MATERIALS IN RESPONSE TO EXTERNAL STIMULI

BY

JUNGWOO SHIN

DISSERTATION

Submitted in partial fulfillment of the requirements
for the degree of Doctor of Philosophy in Materials Science and Engineering
in the Graduate College of the
University of Illinois at Urbana-Champaign, 2019

Urbana, Illinois

Doctoral Committee:

Professor David G. Cahill, Chair
Professor Paul V. Braun, Director of Dissertation Research
Assistant Professor Qian Chen
Associate Professor Randy H. Ewoldt

ABSTRACT

Advances in technologies have led to a utilization of a wide range of transport, storage and release of energy as a form of heat. Researchers in electronics, thermoelectrics, energy science and biomaterials seek for materials with either high or low thermal conductivity as they help to manage heat in the device and the system. However, traditional materials can only provide thermal functionality in one way—thermal conductor or insulator—to prevent or facilitate heat transport. Therefore, a discovery of materials that have a bifunctional thermal transport property in which materials can switch between more than one thermal conductivity state (high and low states) can provide a desirable thermal transport property on-demand. Although there have been attempts to control thermal conductivity of materials using external stimuli, many have failed to show a high and fast thermal property switching of material.

In this dissertation, I present novel stimuli-responsive polymers and Li-ion battery electrode materials that involve a wide range of thermal conductivity modulation in response to external stimuli. I describe thermal conductivity switching between high and low states of these thermal switching materials (TSMs) with structural changes in electronic, atomic and/or molecular levels that are associated with the fundamental thermal transport property.

First, stimuli-responsive liquid crystal networks (LCNs) and light-sensitive azobenzene polymers (azopolymers) were designed and synthesized. Thermal conductivity and macromolecular structure transitions of LCNs and azopolymers were studied by *in-situ* time-domain thermoreflectance (TDTR) and *in-situ* synchrotron X-ray scattering techniques under external stimuli. I observed thermal conductivity switching contrast $r = \Lambda_{high}/\Lambda_{low} \approx 1.5–3.5$ on a switching time of $\tau \approx 10$ s – 10 min for LCNs and azopolymers. This thermal conductivity

switching resulted from an alignment of the backbone and side-chain mesogen groups with applied magnetic and electromagnetic fields in LCNs and azopolymers.

Then, thermal conductivity and elastic modulus changes of metal and metal oxides Li-ion electrode materials were studied during electrochemical reaction with Li^+ ions. Five electrode materials with three electrochemical phase transition mechanisms with Li^+ ions were chosen: Fe_2O_3 and NiO as conversion reaction systems, V_2O_5 and TiO_2 as intercalation systems and Sb as an alloying reaction system. These electrode materials involve characteristic lattice and electronic band structure transitions with respect to their phase transition mechanisms. For conversion materials, 200~300% volume changes were observed due to the large amount of Li^+ ion intake. This large volume changes were associated with an irreversible decrease in thermal conductivity $r \approx 2.5–7.5$ due to the lattice disordering by Li^+ ion. Intercalating V_2O_5 and TiO_2 showed reversible $r \approx 1.6–1.8$ along with small volume changes and stable crystal structure up to 1 mole of Li^+ ($x \leq 1$) intake. Alloying Sb showed the largest volume change of ~300% up to 3 moles of Li^+ intake in the lithiated state with the semimetal (Sb) to semiconductor (Li_3Sb) transition. The large lattice and electronic transition resulted in the largest value $r \approx 30$.

ACKNOWLEDGEMENTS

It is hard to find a great adviser, but I am lucky enough to have two. Prof. David Cahill stands unrivaled in his field, who has kept me motivated, has supported me to never give up and has continuously challenged me. Prof. Paul Braun has always been a great mentor who has shown me his philosophy of science, vision, and insight to think out of the box.

I would like to thank current and previous group members in the Cahill group: En Ju Cho, Sushant Mahat, Yoshinaga Taizo, Jordan Dennison, Akash Rai, Rana Nazifi, Renee Harton, Guangxin Lyu, Qiye Zheng, Kexin Yang, Gyungmin Choi, Jiung Cho, Jongro Park, Johannes Kimling, Judith Kimling, Dongyao Li, Joseph Feser, Richard Wilson and Gregory Hohensee, for their help with experiments and discussions. I give my special thanks to Xu Xie, Zhu Diao, Hyejin Jang and Ella Pek for they are not only talented people I want to work with but people I enjoy working with.

I would like to thank current and previous group members in the Braun group: Ashish Kulkarni, Jin Gu Kang, Christian Ocier, Corey Richards, Kali Serrano, Subing Qu, Michael Caple, Julia Kohanek, Osman Safa Cifci, Michael Caple, Kaitlin Tyler, Daniel Bacon-Brown, Eric Epstein, Yavuz Savsatli, Tsung-Han Tsai, Pengcheng Sun, Zhao Li, Zhenxing Yu, Min Ho Yang, Sung-Kon Kim, Xuejiao Li, Junjie Wang, Neil Krueger, James Pikul, Chunjie Zhang, Matthew Goodman. Jinwoo Kim, Jaewon Choi, Jun-Hee Choi, Hyung-Jun Koo, Jaewon Yoon, Chaeryong Cho and Marta Hatzell.

I am grateful that I met good friends at Illinois: Sanghyeon Kim and Jaeuk Sung. We not only spent days and nights experimenting and discussing, but we shared valuable memories from the first days at Illinois, talked about our dreams and futures, and supported each other. I enjoyed my collaborations with Prof. Cecilia Leal and her students: Dylan Steer, Hojun Kim and

Yookyung Go. Especially I thank Minjee Kang for offering me a great opportunity to learn X-ray scattering techniques and spending a significant amount of her time and efforts, which led to many exciting findings during my Ph.D. studies; she has been a great friend to me and a respectable researcher, too. I want to give my special thanks to Qiujie Zhao, Prof. Christopher Evans, Bong Hoon Kim, Tae Ann Kim, Aram Yoon and Prof. Nancy Sottos for valuable discussions and experiments. I am grateful to collaborate with Dr. Kyung Min Lee and Dr. Timothy White at the Air Force Research Laboratory, Dr. Byeongdu Lee at the Argonne National Laboratory and Xingfei Wei and Prof. Tengfei Luo at Notre Dame University for their significant help in experiments and discussions.

Finally, I like to thank my mother. Her endless support, love, belief in me and philosophy of life has become a part of me, which I have valued since my childhood. Without her, I would not be half the man I am today.

To my family,

for their love and support

TABLE OF CONTENTS

CHAPTER 1: INTRODUCTION

1.1 MOTIVATION

Heat is a fundamental form of energy transferred through materials and interfaces. For heat conduction, I start with Fourier's law $q = -\Lambda \nabla T$, which states that the heat flux q through a material is proportional to the thermal conductivity Λ of the material and the temperature gradient ∇T. This simple equation dictates a ubiquitous phenomenon that the heat transport property is defined by thermal conductivity of materials (a convention to express the rate of heat transfer is thermal diffusivity $\alpha = \sqrt{\Lambda / C}$ where C is the heat capacity per unit volume of the material). In general, thermal conductivity of a material is considered as a sum of the electronic thermal conductivity Λ_e and the lattice thermal conductivity Λ_L(*1*):

$$\Lambda = \Lambda_e + \Lambda_L \tag{1.1}$$

$$\Lambda_L \approx \int \frac{1}{3} C_\omega v_\omega l_\omega d\omega \tag{1.2}$$

$$\Lambda_e = \sigma L T \tag{1.3}$$

where C_ω, v_ω, and l_ω are the volumetric heat capacity, the group velocity, and the mean free path (MFP) of phonons associated with a mode at the angular frequency ω, respectively; σ is the electric conductivity. Equation 1.3 is the Wiedemann-Franz law where L is the Lorentz number and considered as a constant (L_0) for many materials. However, L_0 is the quantum mechanical limit (Sommerfeld value) and $L = L_0$ only applies if the electron scattering is nearly elastic. L can

deviate from L_0 for materials having inelastic electron-phonon scattering and scattering with other carriers (magnons)(*2*).

Most materials exhibit a gradual change in thermal conductivity $\Lambda(T)$ near room temperature(*3-5*). Λ_L increases with T^3 where C follows the Debye model at the low $T << \Theta_D$ where Θ_D is the Debye temperature of materials. Above $T > 0.2\,\Theta_D$, $\Lambda_L(T)$ decreases with temperature (T^{-1}) for crystals due to phonon scattering ($l \propto \Theta_D/T$). $\Lambda_L(T)$ of amorphous solids shows a little to moderate temperature dependency since l does not change much with T. $\Lambda_e(T)$ of metal alloys increases with T according to the Wiedemann-Franz Law (eq. 1.3) while $\Lambda_e(T)$ of pure metals is approximately independent of temperature where the factor of T is canceled out due to the decrease in electron MFP by lattice vibrations. Throughout my dissertation, I also discuss important figures of merit—thermal switching ratio r and switching time τ—to compare various thermal switching materials and to design a fast, high contrast thermal switching material:

$$r = \frac{\Lambda_{\text{high}}}{\Lambda_{\text{low}}} \tag{1.4}$$

$$\tau = t(\Lambda_{\text{high}}) - t(\Lambda_{\text{low}}) \tag{1.5}$$

where Λ_{high} and Λ_{low} are the high and low thermal conductivity values of the material and τ is a time required to switch from the high thermal conductivity state at $t(\Lambda_{\text{high}})$ to the low thermal conductivity state at $t(\Lambda_{\text{low}})$, or vice versa.

Materials with an abrupt change in $\Lambda(T)$ (non-linear temperature dependency) have been studied for their potential as thermal regulators. For example, $\Lambda(T)$ of VO_2 increases abruptly by

50% (r = 1.5) at the metal-to-insulator transition temperature, T_{MI} (340 K), as the electric conductivity increases along with the phase transition(*6, 7*). Liquid-to-solid transition of organic materials(*8*) and phase change memory alloys(*9*) can also exhibit $r \approx 2–3$ at the melting and phase transition point, respectively. Antimony-based alloys (Zn_3Sb, GaSb, CdSbAg) exhibit liquid-to-solid transitions along with the semiconductor-metal transition, which is predicted to exhibit $r \approx 10–15$ as they involve transitions in both Λ_e and Λ_L at melting points above 600 K*(10)*. These materials can be utilized as thermal regulators where the heat flow is passively controlled at a narrow temperature range near the phase transition temperature(*11*).

More advanced materials that respond to non-thermal stimuli, such as electric and magnetic fields with a change in thermal conductivity are sought as "thermal switching materials (TSMs)," which can actively control heat flow at a wide temperature range, analogous to those in the electric circuit(*12-14*). Nonetheless, TSMs have shown limited thermal conductivity contrasts compared to thermal regulators. So far, r of a giant-magneto-thermoresistive Co/Cu multilayer is ≈ 1.8(*15*); r of ferroelectric $Pb(Zr_{0.3}Ti_{0.7})O_3$ film is ≈ 1.1(*16*); and r of electrochemically lithiated/delithiated Li_xCoO_2, Li_xMoS_2 and Li_xP are ≈ 1.5(*17*), ≈ 2(*18*) and ≈ 1.7(*19*), respectively.

To overcome the limits of the current TSMs, I focused on developing systems that can exhibit improved r and t accompanied with the dramatic change in Λ_e and Λ_L, similar to those observed in phase changing thermal regulators. Throughout my dissertation, I describe novel thermal switching polymers and Li-ion electrode materials showing solid-solid and solid-liquid transitions, discuss heat conduction in these materials under external stimuli, advance a structure-property relationship and explain the role of micro- and macromolecular structures in thermal transport properties. I also discuss important figures of merit—thermal switching ratio r and

switching time τ—to compare various thermal switching materials and to design a fast, high contrast thermal switching material.

1.2 THERMAL CONDUCTIVITY SWITCHING IN POLYMERS

Heat is carried as diffusion of vibrational modes in insulating polymers, a process which is highly dependent on the macromolecular ordering of a polymer. While disordered molecular chains dissipate heat by strong phonon scattering, ordered and oriented molecular chains effectively transport heat through the oriented direction(*20*), which I refer as "intrachain thermal transport." As a result, changes in macromolecular ordering have potential to significantly change the thermal transport property of a polymer. For example, the thermal conductivity of polyethylene varies from 0.1 W m^{-1} K^{-1}, when randomly oriented to 90 W m^{-1} K^{-1} along the draw direction of a highly oriented crystalline fiber(*21, 22*). Another important factor contributing to the thermal conductivity of polymers is interchain interaction of polymers. This interchain thermal transport can add up to 0.5 W m^{-1} K^{-1} change in thermal conductivity in addition to the intrachain thermal transport(*23*).

To utilize the advantage of the large thermal conductivity contrast of polymers, I searched polymers that can change macromolecular ordering and interchain interaction in response to external stimuli. In general, these properties of polymers are premarily dictated by the chemical structure (*24*). Recently, studies have shown a number of "smart polymers" which can be modulated by stimuli-modulated reversible chemical transitions(*25*). For example, light(*26-28*), electric(*29*) and magnetic fields(*30*), temperature(*31*), redox reactions(*32*), mechanical force(*33*), and changes in pH(*34*) have all been demonstrated as triggers for

reversible physical and chemical property transitions for applications of polymers in sensing, drug delivery, actuation, and self-healing(*35*-*37*).

Among them, what I found intriguing are order-disorder transitions of liquid crystals (LCs) and liquid crystal polymers which have led to a huge success in an electronic display market. Addition of these LC mesogenic units to polymer chains enabled us to modulate the molecular ordering of polymeric materials by external stimuli, such as electric and magnetic fields.

First of all, I describe a novel thermal switching polymer based on liquid crystal networks (LCNs) modulated by a magnetic field. Aligned LCNs exhibit thermal conductivity switching as a function of macromolecular ordering states controlled by the direction of magnetic fields. The LCNs exhibit $r \approx 1.5$ and $\tau \approx 10$ min. I constructed an effective medium model to describe thermal conductivity changes in LCNs as a function of the orientational order parameter S of aligned mesogen units. I describe the details of the magnetic modulation of LCNs in Chapter 3.

Then, I design and synthesize a thermally switchable azobenzene polymer that exhibits a reversible crystal-to-liquid transition in response to UV and visible light in collaboration with Jaeuk Sung in Sottos research group at UIUC. Azobenzene showed fast and reversible structural transitions between the planar (*trans*) and non-planar (*cis*) conformational states. I hypothesized that addition of azobenzene groups to the side chains of polymers could modulate the intrachain thermal transport property and interchain π-π bonding strength, and thus drive thermal conductivity switching in a fast and reversible manner. I found that this conformational transition between *trans* and *cis* azobenzene moieties resulted in an extreme change in macromolecular

ordering, in response to ultraviolet (UV) and green light, resulting in thermal switching contrast $r \approx 3.5$ and $\tau \approx 10$ s at room temperature. Detail of this research is described in Chapter 4.

1.3 THERMAL CONDUCTIVITY SWITCHING IN LITHIUM-ION BATTERY ELECTRODE MATERIALS

Dynamic thermal transport changes in Li-ion battery electrode materials have been studied as insertion/desertion of Li ions can induce remarkable changes in microstructure as well as the electronic band structure of electrode materials. Nonetheless, except a few intercalating materials, $LiCoO_2$(*17*), MoS_2(*18, 38*) and black phosphorus(*19*), little has been studied for thermal transport properties of Li-ion battery electrodes materials during electrochemical cycling. Especially, dramatic structural and chemical transitions in alloying and conversion electrode materials associated with phase transition induced by Li^+ ions make the accurate thermal measurement difficult.

In Chapter 5, I present a thorough study on the thermal and structural evolution of five Li-ion electrode materials under electrochemical redox reaction with Li^+ ions. Those five electrode materials represent three electrochemical phase transition mechanisms: Fe_2O_3 and NiO for conversion reaction systems, TiO_2 and V_2O_5 for intercalation systems and Sb for an alloying reaction system(*39*).

Each system exhibits characteristic phase transition mechanisms with an electrochemical reaction with Li ions. Conversion materials undergo amorphization at the first discharge caused by an insertion of a large amount of Li^+ ion. Further cycling with Li ions leads to the amorphous solid-solid phase transition between a metal-oxide (MO_x) and metal (M) + xLi_2O phases:

$$MO_x + 2xLi \leftrightarrow xLi_2O + M \quad \text{(conversion)} \tag{1.6}$$

where M can be Fe and Ni. This leads to a large volume changes of ~200% for Fe_2O_3 and NiO, which is associated with an irreversible thermal conductivity decreases at the first cycle (r ~ 1.5–7). After the first cycle, thermal conductivity of NiO and Fe_2O_3 showed a small fluctuation during further cycles. This fluctuation can be attributed to the density changes with varying Li^+ ion concentration predicted by the minimum lattice thermal conductivity $\Lambda_{L,min}$ (*40*)

$$\Lambda_{L,min} = \left(\frac{\pi}{6}\right)^{1/3} k_B n^{3/2} \sum_{i=1}^{3} v_i \left(\frac{T}{\Theta_i}\right)^2 \int_0^{\Theta_i/T} \frac{x^3 e^x}{(e^x - 1)} dx \tag{1.7}$$

where k_B is the Boltzmann constant, n is the atomic number density, v_i is the longitudinal (i = 1) and transverse (i = 2,3) speed of sound, and Θ_i is the Debye temperature. n can be calculated as $n = \rho N_A / M$ where ρ is the density, M is the molecular weight of compounds and N_A is the Avogadro number. v_i can be reduced from the longitudinal modulus C_{11} and the transverse elastic modulus C_{44} as $v_1 = \sqrt{C_{11}/\rho}$ and $v_{2,3} = \sqrt{C_{11}/\rho}$.

Intercalation materials, on the other hand, act as a host material that can provide energetically favorable spots for guest Li^+ ions where insertion and desertion of Li^+ ions into the host are assisted by a charge transfer reaction between the host and Li^+ ions. This charge transfer reaction involves a molecular orbital formation between Li(2s) orbital and host orbital, resulting in an electronic band structure transition. Furthermore, the phonon dispersion of host material changes with varying Li contents. Therefore, r can be defined by both lattice (Λ_L) and electronic contributions (Λ_e). As a result, intercalating TiO_2 and V_2O_5 showed a reversible thermal conductivity switching $r \approx 1.3$–1.4 up to 0.5 and 1 moles of Li^+ intake, respectively.

$$MO_y + xLi \leftrightarrow Li_xMO_y \text{ (intercalation)} \quad (1.8)$$

where M can be Ti and V. These intercalating electrode materials showed stable thermal conductivity values over many cycling, suggesting that intercalating mechanisms are the most thermally stable system during electrochemical cycling with a very small volume change of <10 %.

Lastly, an alloying Sb shows the markedly large $r \approx$ 15-30 during the first few cycles. This large contrast can be attributed to changes in Λ_L and Λ_e during phase transition between semimetal (Sb) and semiconductor (Li_3Sb) states (*41*, *42*).

$$Sb+3Li \leftrightarrow Li_3Sb \text{ (alloying)} \quad (1.9)$$

where Sb exhibits electric contributions of $\Lambda_e \approx 15$ W m^{-1} K^{-1} due to the overlap of valence and conduction bands and lattice contribution of $\Lambda_L \approx 7$ W m^{-1} K^{-1}. As Li ions are inserted to the system, electric conductivity decreases along with separation of valence and conduction bands. The lattice contribution is also dramatically suppressed at Li_3Sb state (*43*). Further details of this study are described in Chapter 5.

1.4 REFERENCES

1. J. M. Ziman, Electrons and Phonons. *Oxford University Press, Oxford, United Kingdom*, (1960).
2. I. Y. Korenblit, Kuznetso.Me, V. M. Muzhdaba, S. S. Shalyt, Electron Heat Conductivity and Wiedemann-Franz Law for Bi. *Sov Phys Jetp-Ussr* **30**, 1009 (1970).
3. G. A. Slack, Thermal Conductivity of MgO, Al_2O_3, $MgAl_2O_4$, and Fe_3O_4 Crystals from 3 Degrees to 300 Degrees K. *Phys Rev* **126**, 427-441 (1962).
4. G. A. Slack, Thermal Conductivity of CaF_2, MnF_2, CoF_2, and ZnF_2 Crystals. *Phys Rev* **122**, 1451-1464 (1961).
5. C. Y. Ho, M. W. Ackerman, K. Y. Wu, S. G. Oh, T. N. Havill, Thermal conductivity of ten selected binary alloy systems. *Journal of Physical and Chemical Reference Data* **7**, 959-1177 (1978).
6. H. Kizuka *et al.*, Temperature dependence of thermal conductivity of VO_2 thin films across metal–insulator transition. *Japanese Journal of Applied Physics* **54**, 053201 (2015).
7. D.-W. Oh, C. Ko, S. Ramanathan, D. G. Cahill, Thermal conductivity and dynamic heat capacity across the metal-insulator transition in thin film VO_2. *Applied Physics Letters* **96**, 151906 (2010).
8. C. Velez, M. Khayet, J. M. O. de Zarate, Temperature-dependent thermal properties of solid/liquid phase change even-numbered n-alkanes: n-Hexadecane, n-octadecane and n-eicosane. *Appl Energ* **143**, 383-394 (2015).
9. J. P. Reifenberg *et al.*, Thickness and stoichiometry dependence of the thermal conductivity of GeSbTe films. *Applied Physics Letters* **91**, 111904 (2007).
10. K. Kim, M. Kaviany, Thermal conductivity switch: Optimal semiconductor/metal melting transition. *Phys Rev B* **94**, 155203 (2016).
11. G. Wehmeyer, T. Yabuki, C. Monachon, J. Q. Wu, C. Dames, Thermal diodes, regulators, and switches: Physical mechanisms and potential applications. *Appl Phys Rev* **4**, 041304 (2017).
12. S. Dhara *et al.*, Tunable thermal conductivity in defect engineered nanowires at low temperatures. *Physical Review B* **84**, 121307 (2011).

13. A. J. Kulkarni, M. Zhou, Tunable thermal response of ZnO nanowires. *Nanotechnology* **18**, 435706 (2007).
14. R. W. Keyes, R. J. Sladek, Piezo-Thermal Conductivity Effect in Germanium. *Phys Rev* **125**, 478-483 (1962).
15. J. Kimling *et al.*, Spin-dependent thermal transport perpendicular to the planes of Co/Cu multilayers. *Phys Rev B* **91**, 144405 (2015).
16. J. F. Ihlefeld *et al.*, Room-Temperature Voltage Tunable Phonon Thermal Conductivity via Reconfigurable Interfaces in Ferroelectric Thin Films. *Nano Lett* **15**, 1791-1795 (2015).
17. J. Cho *et al.*, Electrochemically tunable thermal conductivity of lithium cobalt oxide. *Nat Commun* **5**, 4035 (2014).
18. G. H. Zhu *et al.*, Tuning thermal conductivity in molybdenum disulfide by electrochemical intercalation. *Nat Commun* **7**, 13211 (2016).
19. J. S. Kang, M. Ke, Y. J. Hu, Ionic Intercalation in Two-Dimensional van der Waals Materials: In Situ Characterization and Electrochemical Control of the Anisotropic Thermal Conductivity of Black Phosphorus. *Nano Lett* **17**, 1431-1438 (2017).
20. H. Y. Chen *et al.*, Thermal conductivity of polymer-based composites: Fundamentals and applications. *Prog Polym Sci* **59**, 41-85 (2016).
21. X. J. Wang, V. Ho, R. A. Segalman, D. G. Cahill, Thermal Conductivity of High-Modulus Polymer Fibers. *Macromolecules* **46**, 4937-4943 (2013).
22. R. Shrestha *et al.*, Crystalline polymer nanofibers with ultra-high strength and thermal conductivity. *Nat Commun* **9**, 1664 (2018).
23. X. Xie *et al.*, High and low thermal conductivity of amorphous macromolecules. *Physical Review B* **95**, 035406 (2017).
24. W. J. Koros, S. K. Burgess, Z. Chen, Polymer Transport Properties. *Encyclopedia of Polymer Science and Technology*, 1–96 (2015).
25. M. A. C. Stuart *et al.*, Emerging applications of stimuli-responsive polymer materials. *Nat Mater* **9**, 101-113 (2010).
26. T. J. White, D. J. Broer, Programmable and adaptive mechanics with liquid crystal polymer networks and elastomers. *Nat Mater* **14**, 1087-1098 (2015).

27. M. Burnworth *et al.*, Optically healable supramolecular polymers. *Nature* **472**, 334-337 (2011).
28. A. Suzuki, T. Tanaka, Phase-Transition in Polymer Gels Induced by Visible-Light. *Nature* **346**, 345-347 (1990).
29. T. Tanaka, I. Nishio, S. T. Sun, S. Uenonishio, Collapse of Gels in an Electric-Field. *Science* **218**, 467-469 (1982).
30. J. Thevenot, H. Oliveira, O. Sandre, S. Lecommandoux, Magnetic responsive polymer composite materials. *Chem Soc Rev* **42**, 7099-7116 (2013).
31. M. G. Heskins, J. E., Solution Properties of Poly(N-isopropylacrylamide). *Journal of Macromolecular Science—Chemistry* **2**, 1441-1455 (1968).
32. M. R. Gandhi, P. Murray, G. M. Spinks, G. G. Wallace, Mechanism of Electromechanical Actuation in Polypyrrole. *Synthetic Met* **73**, 247-256 (1995).
33. D. A. Davis *et al.*, Force-induced activation of covalent bonds in mechanoresponsive polymeric materials. *Nature* **459**, 68-72 (2009).
34. S. Dai, P. Ravi, K. C. Tam, pH-Responsive polymers: synthesis, properties and applications. *Soft Matter* **4**, 435-449 (2008).
35. C. D. H. Alarcon, S. Pennadam, C. Alexander, Stimuli responsive polymers for biomedical applications. *Chem Soc Rev* **34**, 276-285 (2005).
36. L. Zhai, Stimuli-responsive polymer films. *Chem Soc Rev* **42**, 7148-7160 (2013).
37. M. L. Wei, Y. F. Gao, X. Li, M. J. Serpe, Stimuli-responsive polymers and their applications. *Polym Chem-Uk* **8**, 127-143 (2017).
38. A. Sood *et al.*, An electrochemical thermal transistor. *Nat Commun* **9**, 4510 (2018).
39. V. Etacheri, R. Marom, R. Elazari, G. Salitra, D. Aurbach, Challenges in the development of advanced Li-ion batteries: a review. *Energ Environ Sci* **4**, 3243-3262 (2011).
40. D. G. Cahill, S. K. Watson, R. O. Pohl, Lower Limit to the Thermal-Conductivity of Disordered Crystals. *Phys Rev B* **46**, 6131-6140 (1992).
41. S. Y. Wang *et al.*, Anisotropic Multicenter Bonding and High Thermoelectric Performance in Electron-Poor CdSb. *Chem Mater* **27**, 1071-1081 (2015).
42. A. Bath, J. G. Gasser, R. Kleim, Electrical-Resistivity of Zn-Sb and Cd-Sb Liquid Alloys in the Compound-Forming Concentration Range. *Phys Lett A* **91**, 355-357 (1982).

43. X. X. Yang, Z. H. Dai, Y. C. Zhao, J. Y. Liu, S. Meng, Low lattice thermal conductivity and excellent thermoelectric behavior in Li_3Sb and Li_3Bi. *J Phys-Condens Mat* **30**, 425401 (2018).

CHAPTER 2: EXPERIMENTAL METHODS

Parts of Chapter 2 were published in "Light-triggered thermal conductivity switching in azobenzene polymers," Jungwoo Shin, Jaeuk Sung, Minjee Kang, Xu Xie, Byeongdu Lee, Kyung Min Lee, Timothy J. White, Cecilia Leal, Nancy R. Sottos, Paul V. Braun, David G. Cahill, *Proceedings of the National Academy of Sciences* ***in press***, (2019).

Parts of Chapter 2 were published in "Measurement of water vapor diffusion in nanoscale polymer film by frequency domain probe beam deflection," Xu Xie, Jordan M. Dennison, Jungwoo Shin, Zhu Diao, David G. Cahill*," Review of Scientific Instruments* **89**, 104904, (2018).

In Chapter 2, I describe experimental methods to characterize the thermal and physical properties of thermal switching materials (TSMs) including stimuli-responsive polymers and Li-ion battery electrode materials that switch between the high and low thermal conductivity states. First, I describe time-domain thermoreflectance (TDTR) which was used to study thermal conductivity changes of TSMs under external stimuli. I used a backside TDTR with a bidirectional heat transport model to calculate thermal conductivity changes of TSMs and the sensitivity and substrates were optimized for such measurements. In addition, I used a frequency-domain probe beam deflection (FD-PBD) to measure low thermal conductivity states of polymers where the backside TDTR measurement is not sensitive. The rest of chapter describes the synchrotron X-ray scattering techniques which were used to study the macromolecular ordering transition of polymers, and the electrochemical experiments designed for real-time thermal conductivity measurement of Li-ion battery electrode materials during charge/discharge cycling.

2.1 TIME-DOMAIN THERMOREFLECTANCE (TDTR)

With the advance of ultra-fast pump-probe laser techniques, TDTR has become a versatile and high-throughput tool to measure thermal conductivity of materials from the ultralow thermal conductivity of fullerene derivatives (*1*) to the ultrahigh thermal conductivity of BAs (*2*). Throughout my Ph.D. studies, I used two time-domain thermoreflectance (TDTR1 and TDTR2) systems at the Materials Research Laboratory at the UIUC. Figure 2.1A shows the optical layout of the TDTR. I used 785 nm mode-locked Ti-sapphire laser pulses (~ 200 fs duration) with a broad spectrum of a full width at half maximum (FWHM) bandwidth of 10–20 nm (*3*). Then, I used a polarized beam splitter (PBS) and sharp-edged optical filters with a cut-off wavelength of 785 nm to create and separate spectrally distinct pump (long-pass filter) and probe beams (short-pass filter). The repetition frequencies of mode-locked Ti-sapphire lasers were 80 MHz for TDTR1 and 74.8 MHz for TDTR2. The pump beam was modulated by an electro-optical (EO) modulator which is connected to a function generator (SR DS345 programmable function generator) imposing a square wave modulation at f = 1–11 MHz. The probe beam was modulated by a mechanical chopper operated at a fixed frequency at 200 Hz. A set of PBS and beam splitter (BS) were used to align the pump and probe beams after the modulation. Both pump and probe beams were then focused on the sample with an objective lens. The typical $1/e^2$ intensity radii of the pump (w_0) and probe beams (w_1) at the transducer surface were 5–10 μm with 5× and 10× objective lenses, respectively; and the intensities of the pump and probe beam were modulated by λ/2 plates to 5–10 mW and 3–5 mW, respectively.

TDTR heats and senses the temperature excursions of a transducer metal film on a multi-layer sample in response to a train of femtosecond pump and probe laser pulses (*4*). The pump

pulses absorbed in the transducer layer result in a transient temperature rise (a few ps) followed by a decay of temperature over a relatively long times scale (a few ns) as heat diffuses into the sample. Figure 2.1B shows a typical sample configuration optimized for the backside TDTR measurements of thermal switching materials (TSMs). The temperature change of the transducer film was detected as an optical reflectance changes ΔR of the transducer which is linearly dependent to the temperature change ΔT at the chosen wavelength (dR/dT = constant at 785 nm for Al transducer). An optical delay stage was used to delay the arrival time of the probe beam with respect to the pump beam. The temperature profile was carried as an intensity change of the probe beam with a varying delay time, giving the temperature profile of the transducer film before and after the arrival of the pump pulse at t = 0 ps. The reflected pump beam was detected by a Si photodiode detector at varying delay time from t = –20 ps to t = 3.6 ns.

An additional short-pass filter next to the PBS was used to block the reflected pump beam. To maximize the signal to noise ratio an RF amplifier (SR 445A, with a gain of G = 5) was used to amplify the signal from the photodiode with an RF resonance filter with a maximum Q-factor (~10) at the modulation frequency f. The amplified signal was sent to a radio frequency (RF) lock-in amplifier (SR 844) synchronized to the function generator at f. The in-phase voltage (V_{in}) and out-of-phase voltage (V_{out}) from the lock-in amplifier were then sent to a computer which is equipped with a LabVIEW software-based AF lock-in synchronized with the mechanical chopper at 200 Hz.

The V_{in} and V_{out} carry information of ΔR which is associated with the amplitude and phase of the temperature wave, as a form of the in-phase and out-of-phase temperature ΔT_{in} and

ΔT_{out} at f. To be specific, the lock-in amplifier picks up the convoluted frequency components at f and $-f$ in real and imaginary domains at each delay time t:(*4*)

$$\mathrm{Re}[\Delta R_M(t)] = \frac{dR}{dT}\left\{\sum_{m=-M}^{M} \Delta T\left(\frac{m}{\tau}+f\right)+\Delta T\left(\frac{m}{\tau}-f\right)\right\}e^{i2\pi mt/\tau} \tag{2.1}$$

$$\mathrm{Im}[\Delta R_M(t)] = -i\frac{dR}{dT}\left\{\sum_{m=-M}^{M} \Delta T\left(\frac{m}{\tau}+f\right)-\Delta T\left(\frac{m}{\tau}-f\right)\right\}e^{i2\pi mt/\tau} \tag{2.2}$$

where τ is the repetition time of the mode-locked Ti-sapphire laser and M = 10τ/t and dR/dT is the thermoreflectance of the transducer at λ = 785 nm. These reflectance changes are measured as the lock-in amplifier voltages as in the following:

$$V_{\mathrm{in}}(t) = \frac{GV_0Q}{\sqrt{2}}\frac{\mathrm{Re}[\Delta R_M(t)]}{R}e^{i2\pi ft} \tag{2.3}$$

$$V_{\mathrm{out}}(t) = \frac{GV_0Q}{\sqrt{2}}\frac{\mathrm{Im}[\Delta R_M(t)]}{R}e^{i2\pi ft} \tag{2.4}$$

Throughout the dissertation, V_{in} was divided by V_{out} to cancel out the dR/dT, average output voltage V_0, the quality factor Q = 10 of the resonance filter, the gain of the amplifier G and the reflectance of the transducer R.

The ratio $V_{\mathrm{in}}/V_{\mathrm{out}}$ is sensitive to the thermal effusivity $e = \sqrt{\Lambda C}$ at high frequencies $f > \Lambda/(\pi C d^2)$ and proportional to Λ and inversely proportional to C and at low frequencies $f \le \Lambda/(\pi C d^2)$ where d is the thickness of the TSM. I modulated the thermal penetration depths $d_T = \sqrt{\Lambda/(f\pi C)}$ to separate the thermal conductivity Λ and the heat capacity per unit volume C of TSMs(*5, 6*). These penetration depths are much smaller than the size of the focused beam, and consequently, the measured thermal conductivity represents the through-plane thermal transport across interfaces. In the rest of the dissertation, I fitted $-V_{\mathrm{in}}/V_{\mathrm{out}}$ curves to calculate thermal properties of TSMs using the bidirectional heat flow model described in Chapter 2.2.

2.2 BIDIRECTIONAL HEAT TRANSPORT MODEL

In Chapter 2.2, I expand a heat diffusion model from a unidirectional(*4*) to bidirectional by considering upward and downward heat propagations from the heating layer ($j = h$) to the top ($j = 1$) and the bottom layers ($j = N$), respectively (*5, 7*). First, I use a Hankel transform to convolute Gaussian-shaped beam and the periodic point heat source to calculate the temperature solution of layered materials at spatial and temporal frequency domain with a spatial frequency k and an angular frequency ω. The temperature of the heating interface (interface between the transducer and the substrate) heated by the pump beam with w_0 and measured by the probe beam with w_1 is:

$$\Delta T_0 = 2\pi A \int_0^\infty G_0(k) e^{-\pi^2 k^2 (w_0^2 + w_1^2)/2} dk \tag{2.5}$$

where A is the absorbed heat at ω, which is defined as $A = (1 - R - Tr)P_0$ where Tr is the transmittance of the sample and P_0 is the pump beam intensity(*8, 9*). $G_0(k)$ is a propagator function of thermal parameters including Λ, C and d of each layer.

For the bidirectional model, I took account of both upward G_{up} and downward G_{down} propagators, considering a heating source sandwiched by a substrate and a thermally functional material with a total number of layers N. $G_{up}(k)$ represents the upward heat flow from the lower interface of Al transducer film to the TSM and beyond (h to 1). $G_{down}(k)$ represents the downward heat flow from the heating layer to the substrate (h–1 to N). I consider the top (j =1) and the bottom ($j = N$) layers thermally thick.

$$G_{up}(k) = \frac{1}{\gamma_h}\left(\frac{A_h^+ + A_h^-}{A_h^- - A_h^+}\right) \tag{2.6}$$

$$\begin{pmatrix} A^+ \\ A^- \end{pmatrix}_j = \frac{1}{2\gamma_j}\begin{pmatrix} e^{-u_j d_j} & 0 \\ 0 & e^{u_j d_j} \end{pmatrix}\begin{pmatrix} \gamma_j + \gamma_{j-1} & \gamma_j - \gamma_{j-1} \\ \gamma_j - \gamma_{j-1} & \gamma_j + \gamma_{j-1} \end{pmatrix}\begin{pmatrix} A^+ \\ A^- \end{pmatrix}_{j-1} \tag{2.7}$$

$$\begin{pmatrix} A^+ \\ A^- \end{pmatrix}_1 = \begin{pmatrix} 1 \\ 0 \end{pmatrix} \tag{2.8}$$

$$G_{\text{down}}(k) = \frac{1}{\gamma_{h+1}}\left(\frac{B_{h+1}{}^{+} + B_{h+1}{}^{-}}{B_{h+1}{}^{-} - B_{h+1}{}^{+}}\right) \tag{2.9}$$

$$\begin{pmatrix} B^+ \\ B^- \end{pmatrix}_j = \frac{1}{2\gamma_j}\begin{pmatrix} e^{-u_j d_j} & 0 \\ 0 & e^{u_j d_j} \end{pmatrix}\begin{pmatrix} \gamma_j + \gamma_{j+1} & \gamma_j - \gamma_{j+1} \\ \gamma_j - \gamma_{j+1} & \gamma_j + \gamma_{j+1} \end{pmatrix}\begin{pmatrix} B^+ \\ B^- \end{pmatrix}_{j+1} \tag{2.10}$$

$$\begin{pmatrix} B^+ \\ B^- \end{pmatrix}_N = \begin{pmatrix} 0 \\ 1 \end{pmatrix} \tag{2.11}$$

where $\gamma_j = \Lambda_j \mu_j$, $\mu_j = \sqrt{4\pi^2 k^2 + q_j{}^2}$, $q_j = \sqrt{i\omega C_j / \Lambda_j}$ and N is the total number of layers. $G_0(k)$ of the bidirectional model is calculated as

$$G_0(k)^{-1} = G_{\text{up}}(k)^{-1} + G_{\text{down}}(k)^{-1} \tag{2.12}$$

Note that G_0 is calculated at each value of k and ω before integrating with respect to k. Figure 2.2 shows the schematic illustration for the bidirectional heat transport model described above. The interfaces between dissimilar materials are considered to have a typical interfacial thermal resistance of 20–200 MW m^{-2} K^{-1}, which is equivalent to a thin layer of material with Λ = 0.02–0.2 W m^{-1} K^{-1} and d = 1 nm with a negligible C = 0.1 J cm^{-3} K^{-1}.

2.3 SUBSTRATES PREPARATION

In Chapter 2.3 I describe methods to prepare and characterize substrates for the backside TDTR measurements of TSMs. The substrates were prepared by i) spin-coating with polyimide (PI) precursor solution (PI2545, HD Microsystems) on sapphire substrates, ii)

curing at vacuum oven at 200 ºC for 2 h, and iii) subsequent Al thin film deposition by a magnetron sputtering. The cured PI film provides thermal insulation between the Al transducer and the sapphire substrate, thereby increasing the sensitivity of the measurement to the thermal conductivity of the TSMs(*10*). The thickness of the PI layers was measured by ellipsometry (200–400 nm). These values are greater than the heat penetration depth and can be considered as an infinitely thick insulating layer in our modeling of the TDTR data. The thickness of the PI layer does, however, play a dominant role in the steady-state temperature rise. I calculated that the fraction of steady-state temperature rise due to the PI layer is 84 % by comparing ΔT_{ss} with and without the PI layer. In this dissertation, typical per-pulse heating and steady-state heating by the accumulation of pulses are $\Delta T_{pp} < 1$ K and $\Delta T_{ss} = 1$–2 K, respectively.

I calculate the sensitivity S_X from the ratio of the change in a quantity X to a change in the ratio ($-V_{in}/V_{out}$) for Al/PI/sapphire substrates where X can be any thermal parameter such as thermal conductivity, heat capacity or thickness of each layer.

$$S_X = \frac{d \ln\left(-\frac{V_{in}}{V_{out}}\right)}{d \ln X} \tag{2.13}$$

Since S_X is highly dependent to the modulation frequency, beam spot size and thickness of each layer, I chose the optimum condition in which the sensitivity of a thermal parameter (usually Λ of TSMs) dominates others. Figure 2.3 shows a calculated sensitivity plot for a typical polymer film ($\Lambda = 0.2$ W m^{-1} K^{-1}, $C = 1.8$ J cm^3 K^{-1}, $d = 200$ nm) on an Al (50 nm)/PI (400 mm)/sapphire substrate.

I found that the most significant contribution to $-V_{in}/V_{out}$ other than the thermal properties of samples comes from the thermal properties of Al transducer (d_{Al}, C_{Al}). I performed an optical transfer-matrix calculation with sapphire/PI/Al film to estimate the effect of dn/dT of the PI

layer. Assuming that PI layer with dn/dT = -10^{-4} K^{-1} is equally heated as Al, the thermoreflectance (ΔR) only changed by 2% compared with the calculated ΔR without considering dn/dT of the PI layer.

In the dissertation, I measured d_{Al} by picosecond acoustics to calculate accurate thermal properties of samples. Figure 2.4A shows the measured curve for Al (48 nm)/PI (400 mm)/sapphire substrate. I observed a signal oscillation at the frequency of Γ (t < 100 ps, Figure 2.4B) created by the reflection of the longitudinal acoustic wave in Al at interfaces:

$$\Gamma = v_{Al} / 2d_{Al?} \tag{2.14}$$

where v_{Al} is the longitudinal speed of sound (6.42 nm ps^{-1}) and d_{Al} is the thickness of Al.

The Fourier transformed $-V_{in}/V_{out}$ data (Figure 2.4C) shows a maximum at Γ = 74 GHz, which can be converted to d_{Al} = 44 nm. I typically add a 3–4 nm to the d_{Al} to take account of an Al_2O_3 native oxide layer. The solid line in Figure 2.4A is a fitted TDTR curve using the following parameters: Λ_{Al} (180 W m^{-1} K^{-1}) was calculated by the Wiedemann-Franz law from the electrical conductivity measured by four-point probes; C_{Al} = 2.49 J cm^{-3} K^{-1} was obtained from the literature; the thermal properties of sapphire (Λ = 35 W m^{-1} K^{-1}, C = 3.08 J cm^{-3} K^{-1}) and PI (Λ = 0.2 W m^{-1} K^{-1}, C = 1.80 J cm^{-3} K^{-1}) were obtained from the literature and independent measurements, respectively.

For an accurate analysis of thermal conductivity with a wide temperature window, I first tested the thermal stability and measured temperature-dependent thermal properties of the Al/PI/sapphire substrate. Figure 2.5A shows measured TDTR curves of Al/PI/sapphire substrate signals from –50 ºC up to 150 ºC using a temperature controlled INSTEC HOT/COLD stage with an optical window allowing TDTR measurements during heating/cooling cycles. Figure 2.5B shows $-V_{in}/V_{out}$ values of Al/PI/sapphire substrate at fixed t = 100 ps from – 50 ºC up to

150 °C. Small changes in $-V_{in}/V_{out}$ with respect to temperature were interpreted as a change of thermal effusivity of PI layer $e_{PI}(T)$ along with heat capacity changes of Al and sapphire.

I fitted $-V_{in}/V_{out}$ using the bidirectional heat transport model with the thermal effusivity of a TSM, e_{TSM}, as the only free parameter. For *in situ* TDTR measurements, I collected $-V_{in}/V_{out}$ values continuously at fixed t = 60 – 200 ps and I calculated Λ_{TSM} by using a relationship $\Lambda_{TSM} = e_{TSM}{}^2 / C_{TSM}$ where C_{TSM} was measured by an independent TDTR measurement at low $f \leq \Lambda_{TSM} / (\pi C_{TSM} d_{TSM}{}^2)$ or a differential scanning calorimetry (DSC).

2.4 FREQUENCY-DOMAIN PROBE BEAM DEFLECTION (FD-PBD)

For TSMs that exhibit Λ_{low} lower than the thermal conductivity of the thermal blocking layer (polyimide = 0.2 W m^{-1} K^{-1}, SiO_2 = 1.3 W m^{-1} K^{-1}), a majority of the heat deposited by the pump beam flows to the substrate side. Therefore, the sensitivity of backside TDTR measurements to the thermal conductivity of TSMs is significantly decreased. In collaboration with Xu Xie in Cahill group, we developed frequency-domain probe beam deflection (FD-PBD) to accurately measure thermal conductivity of low-Λ materials (especially for liquids). The FD-PBD is based on the measurement of the deflection of the probe beam caused by the refractive index (n_l) gradient of the liquid under the periodic heating by the pump beam (*7*). This technique is sensitive to the thermo-optic coefficient dn_l/dT and the thermal diffusivity $\alpha_l = \sqrt{\Lambda_l / C_l}$ of the liquid.

The model for the FD-PBD follows previous works in Cahill group on time-domain probe beam deflection(*7, 11, 12*). First, I used the transducer temperature solution from the bidirectional model (Chapter 2.2) where the temperature flow in j^{th} layer can be expressed as

$$T_j(k,z) = T_j^+(k)\exp(\mu_j z) + T_j^-(k)\exp(-\mu_j z) \tag{2.15}$$

where z is the directional coordinator from the interface. I consider a heat from the transducer to a thermally thick material with α_1 ($T^+ = 0$). Then, the temperature profile from the surface of the transducer film to the material in the z-direction is

$$T(k,z) = \Delta T_0(k)\exp(-\mu_1 z) \tag{2.16}$$

which causes changes in the beam path displacement Z_1 through the liquid with a refractive index n_1 by

$$Z_1(k) = 2\frac{dn_1}{dT}\int_0^\infty \Delta T_0(k)\exp(-\mu_1 z)dz \tag{2.17}$$

$$Z_1(k) = -\frac{2}{\mu_1}\frac{dn_1}{dT}\Delta T_0(k) \tag{2.18}$$

where $\mu_1 = \sqrt{4\pi^2 k^2 + i\omega/\alpha_1}$).

The approximate solution for the probe beam deflection $\Delta\theta$ at a beam offset distance r_0 is, therefore:

$$\Delta\theta = 4\pi^2 n_1 \int_0^\infty Z_1(k)S(k)J_1(2\pi k r_0)k^2 dk \ , \tag{2.19}$$

where the Hankel transformed probe beam profile *S(k)* is defined as

$$S(k) = A\exp(-\pi^2 k^2 w_1^2/2) \tag{2.20}$$

I modified TDTR system to detect the probe beam deflection (Figure 2.6A) by replacing the Si photodiode with a position sensitive detector (PSD, Visible Quadrant Cell Photoreceiver Model 2901, New Focus). I removed the mechanical chopper and the focusing lens before the detector. I fixed the time delay at t = –50 ps during measurements. The EO modulator was used to modulate the pump beam at frequency f = 10 Hz–100 kHz and a motorized actuator was used to steers the pump beam by an offset r_0 with respect to the probe beam. I used a 5× objective lens with a focal length D = 40 mm in these experiments where the objective lens converts the angular deflection of the probe beam to a displacement $\Delta x = D\Delta\theta$ of the probe beam.

Then, the frequency dependent probe beam displacement was measured as the differential voltage output of the PSD, which is converted to the RMS voltage of the AF lock-in amplifier.

$$V_{RMS} = \frac{D\Delta\theta}{\sqrt{2}W}\frac{G}{0.65}V_{sum} \tag{2.21}$$

where W is the free-space laser size, G is the second-stage gain of the PSD, V_{sum} is the total voltage output from the PSD, and a prefactor 0.65.

I validated the FD-PBD setup using liquid cells consisting of 1-mm thick DI-water and EtOH liquids sandwiched by a 100 nm Au-coated fused silica substrate and a glass cover slide (Figure 2.6B). Then, I measured the exact beam radius with the beam offset TDTR(*13*). Figure 2.7A shows measured beam offset TDTR data and the Gaussian fitted curve with varying beam offset distance. Immediately following, I switched from TDTR setup to FD-PBD setup and calibrated the beam offset center. Figure 2.7B shows measured and fitted FD-PBD curves for DI-water with varying beam offset distance from −20 μm to 20 μm at f = 300 Hz. I chose $f \approx D_{\mathrm{H_2O}} / (2\pi w_0^2)$ where $D_{\mathrm{H_2O}}$ is the thermal diffusivity of water (1.43 10^{-7} m^2 s^{-1}). Note that the

beam deflection signal goes to zero at r = 0 since the beam offset center where the pump and probe beams overlap perfectly.

To maximize the sensitivity of FD-PBS, I calculated the normalized in-phase and out-of-phase sensitivities to the parameter X as

$$S_{\text{in}}(X) = \frac{X}{\Delta\theta_{\text{out}}(500\text{ Hz})}\frac{\partial\Delta\theta_{\text{in}}}{\partial X} \tag{2.22}$$

$$S_{\text{out}}(X) = \frac{X}{\Delta\theta_{\text{in}}(500\text{ Hz})}\frac{\partial\Delta\theta_{\text{in}}}{\partial X} \tag{2.23}$$

where I used X as Λ and C of liquids, w_0, $r_{0,}$ and Λ of Al transducer. The calculated $S_{\text{in}}(X)$ and $S_{\text{out}}(X)$ plots are shown in Figure 2.8.

Since the FD-PBD curves at a fixed beam offset r_0 and $-r_0$ are symmetric with respect to r = 0, I balanced the FD-PBD signals by using the following equation to offset non-thermal signals.

$$V_{\text{in,balanced}} = \frac{V_{\text{in}}(r_0) - V_{\text{in}}(-r_0)}{2} \tag{2.24}$$

$$V_{\text{out,balanced}} = \frac{V_{\text{out}}(r_0) - V_{\text{out}}(-r_0)}{2} \tag{2.25}$$

Figure 2.9 shows measured (balanced) and fitted FD-PBD curves for DI-water and EtOH on Au (100 nm)/SiO_2 substrates at a fixed beam offset at 10 μm and −10 μm. I fixed C and n_l values for DI-water and EtOH (C_{H_2O} = 4.13 J cm^{-3} K^{-1}, C_{EtOH} = 1.94 J cm^{-3} K^{-1}, n_{H_2O} = 1.32, n_{EtOH} = 1.36 at 785 nm), and used Λ and dn_l/dT as free parameters for H_2O and EtOH. The

calculated thermal conductivity from the curve fitting (solid lines) matched with the literature values (Λ_{H_2O} = 0.60 W m^{-1} K^{-1}, Λ_{EtOH} = 0.17 W m^{-1} K^{-1}).

2.5 ELECTROCHEMICAL MODULATION OF LITHIUM-ION BATTERY ELECTRODE MATERIALS

Measurement of thermoreflectance signal without optical artifacts is critical for the analysis of thermal properties of electrode materials. The electrode materials and electrolytes exhibit large thermo-optic constant, dR/dT, which can add a significant thermal response of materials other than the transducer when the transducer is not opaque. The TDTR model assumes that the reflected probe beam only carries the temperature of the transducer layer. Depending on the signal of dR/dT of the electrodes and electrolytes, non-opaque transducer film would end up with overestimation or underestimation of thermal conductivity of the electrode materials.

Since the thickness of the transducer film for the backside TDTR measurement is inversely proportional to the sensitivity of the thermal properties of electrode materials, there is a certain range of the transducer thickness to achieve high sensitivity as well as optical opacity. In this dissertation, I chose 60–80 nm as an optimum thickness for the backside TDTR analysis. For this range, Au and Pt are partially transparent and dR/dT is about an order of magnitude smaller than Al at λ = 785 nm (*8, 9*). I also observed a significant optical artifact (~ 20% of the total TDTR signal) from Au transducer with organic electrolytes due to the fraction of light transmitted and reflected through the electrolytes. Throughout the dissertation, I chose Al transducer film for the *in situ* backside TDTR measurement of electrode materials.

Al has been utilized as a current collector for cathode materials where Al film is stable in the range of 0.5–5 V vs Li/Li^+. Below 0.5 V vs Li/Li^+, Al forms a binary alloy with Li by an electrochemical reaction (*14, 15*). For this potential range, all cathode materials and some of the anode materials for Li-ion battery electrodes are safe. For example, 3-*d* metal oxides, Sn and Sb-based anode materials are stable in this range, but carbon and Si-based anode materials, which undergo discharge reaction below 0.5 V vs Li/Li^+ are incompatible with Al film. Figure 2.10 shows cyclic voltammetry (CV) curves of Al film with varying cut-off voltages from 0.5 to 0 V vs Li/Li^+. Li metal foil was used as a counter electrode. CV curves suggested that the Al film is stable above 0.2 V vs Li/Li^+, which is slightly lower than the standard potential of LiAl reaction due to the presence of a native oxide layer.

Contrary to many cathode materials, which undergo intercalation reaction with negligible volume change during electrochemical reaction with Li ions, anode materials exhibit moderate (~100 %) to the extreme (~300 %) volume changes associated with an insertion of Li ions to the materials (*16*). This large volume expansion resulted in delamination and destruction of electrode materials, which not only deteriorates the electrochemical capacity and cyclability of electrodes but also makes impossible for TDTR measurements. In collaboration with Sanghyeon Kim in Braun group, we designed two types of electrochemical cells for real-time TDTR measurements of electrode materials under continuous cycling with large volume changes.

Figure 2.11 shows liquid and solid electrochemical cells which are designed for electrode materials with little or moderate (<100 %) volume changes and extreme volume changes (>100 %), respectively. Liquid electrochemical cells allow free volume expansion of electrode materials. Solid electrochemical cells were designed to prevent delamination of

electrode materials upon volume changes by pressurizing the cell. For both setups, I used Al/SiO_2/sapphire substrates as a working electrode and optical transducer, which were prepared by plasma-enhanced chemical vapor deposition (PECVD) of SiO_2 film (~200 nm) on sapphire substrates followed by Al magnetron sputtering (60 nm). 15-nm Au film was deposited for the solid electrochemical cell experiments to provide better adhesion. The methods depositing electrode materials are described in Chapter 5.

For liquid electrochemical cells, I used 1 M lithium perchlorate ($LiClO_4$) dissolved in ethylene carbonate (EC) and dimethyl carbonate (DMC) (1:1 by volume) solution as a liquid electrolyte and Li metal foil (Alfa Aesar, 99.9%) as the counter electrode for the two-electrode setup. The home-made liquid cell was assembled in the Ar-filled glove box with custom made glass jar sealed with the electrode material/Al/SiO_2/sapphire substrate and rubber O-rings.

Solid electrochemical cells consist of a Li_2S-P_2S_5 solid electrolyte and the In-Li alloy counter electrode, which suppresses Li dendrite formation during cycling (*17*). The solid electrolytes were prepared by high-energy ball milling (8000M Mixer/Mill, SPEX SamplePrep) Li_2S (Sigma, 99.98%) and P_2S_5 (Sigma, 99%) with a 77.5 to 22.5 molar ratio for 10 h in a stainless-steel vial under Ar atmosphere. A home-made solid-state cell consists of polyaryletheretherketone (PEEK) cell die with two Ti metal rods as current collectors for both working and counter electrode. One of the Ti metal rods was modified with a small hole to load a sample and to ensure laser beam pathway.

A solid-state cell was assembled in the Ar-filled glove box as follows. The electrode/Al/SiO_2/sapphire substrate (2 mm diameter), was inserted into the hole in a Ti metal rod. Then, 100 mg of 77.5Li_2S-22.5P_2S_5 solid electrolytes was spread on the top of the sample

and pressed at 1 metric ton in the PEEK cell die to form a pellet (1-inch diameter). Finally, In-Li alloy counter electrode was attached to the other side of the solid electrolyte pellet and pressed at 0.5 metric tons. The solid-state cell was then sealed with a 3M adhesive tape before taken out of the glove box. The solid-state cell was placed between two jaws in a vise which was hand-tightened during TDTR measurements.

The thermal properties of electrode materials with varying Li ion contents were measured by *in situ* TDTR measurements under galvanostatic cycling (charge/discharge with a constant current) and cycling voltammetry (linear voltage sweeps in a certain voltage window). The electrochemical potential and capacity of the working electrode were converted to the Li ion contents in the electrode materials. All electrochemical experiments were conducted and measured by a portable potentiostat (SP-200, Bio-Logic) for both liquid and solid-state cell at room temperature.

2.6 SYNCHROTRON X-RAY SCATTERING TECHNIQUES

In Chapter 2.6, I describe small and wide-angle X-ray scattering (SAXS and WAXS) and grazing incident small and wide-angle X-ray scattering (GISAXS and GIWAXS) to study macromolecular ordering change of TSMs, especially for polymer films.

Synchrotron X-ray scattering techniques are powerful tools to understand the structure, shape and periodicity of nanostructures in polymer films due to the superior brilliance (~10^{10} times higher than the lab source), monochromatic ($\Delta\lambda/\lambda \sim 10^{-5}$) and coherent X-ray beam source with a small divergence $\Delta\theta \sim 10^{-7}$. The bright, monochromatic X-ray source allows us to measure complex macromolecular structures of polymers in a few angstroms to tens of

nanometer scale with a time scale of milliseconds (*18*). In collaboration with Minjee Kang in Leal group, we carried out synchrotron X-ray scattering experiment at the 12-ID-B and 12-ID-C beamlines at the Advanced Photon Source, Argonne National Laboratory, with 13 –18 keV photons with a beam width of 200 μm. The 2-D GIWAXS scattering data were collected with a PerkinElmer XRD 1621 CN detector. The 2-D WAXS scattering data were collected with a Pilatus 300k detector; SAXS and GISAXS data were collected with Pilatus 2M large area detector. The temperature of the sample was controlled by an INSTEC temperature-controlled stage during measurements. For GIWAXS and GISAXS measurements, the incident angle of the beam was varied from 0.1° to 0.25° to find the optimum angle for each sample (which is slightly larger than the critical total reflection angle α_c of the film).

For 2-D reciprocal space, the scattering intensity $I(\vec{q})$ carries important information regarding the structure of materials with respect to the scattering vector $\vec{q}$

$$\vec{q} = \vec{k}' - \vec{k} \tag{2.26}$$

where $\vec{k}$ is the incident wavevector and $\vec{k}'$ is the scattered wavevector. For elastic scattering, $I(\vec{q})$ is maximized when the reciprocal lattice meets the Ewald sphere with radius $|k|$. For crystals, $I(\vec{q})$ depends on the structure factor of the unit cell, resulting in 3-D interference function as follows.

$$I(\vec{q}) = I_0 r_e^2 \frac{\sin^2\alpha}{R^2}\left|\sum_{j=1}^{Nc} f_j(\vec{q}) e^{i\vec{q}\cdot\vec{r_j}}\right|^2 \cdot \frac{\sin^2\frac{1}{2}N_1\vec{q}\cdot\vec{a}_1}{\sin^2\frac{1}{2}\vec{q}\cdot\vec{a}_1} \cdot \frac{\sin^2\frac{1}{2}N_2\vec{q}\cdot\vec{a}_2}{\sin^2\frac{1}{2}\vec{q}\cdot\vec{a}_2} \cdot \frac{\sin^2\frac{1}{2}N_3\vec{q}\cdot\vec{a}_3}{\sin^2\frac{1}{2}\vec{q}\cdot\vec{a}_3} \tag{2.27}$$

where I_0 is the intensity of incident X-ray, r_e is Thomson scattering length, α is the polarization angle, R is the radius of the scattered plane wave (or distance from the sample), $f_j(\vec{q})$ is the

atomic form factor, $\vec{r}_j$ is the position of j^{th} atom relative to the origin in 3-D real space with unit vectors of a_1, a_2 and a_3; N_c is the total number of the unit cell; and N_1,N_2 and N_3 are the numbers of unit cells in each direction. $I(\vec{q})$ is maximized when

$$\vec{q} \cdot \vec{g}_{hkl} = 2\pi \tag{2.28}$$

where $\vec{g}_{hkl}$ is the reciprocal lattice vector of the *hkl* plane.

In real space, $I(\vec{q})$ is measured with 2-D CCD detector as a function of incident angle and scattered angle where the scattering vector is presented as q_x, q_y and q_z with respect to the incident angle. For transmission X-ray scattering experiment, q is isotropic because of the random orientation of the lattice plane of powders. For grazing incident X-ray scattering experiments, q_x and q_y are scattering components in in-plane direction while q_z is the out-of-plane scattering component. For grazing incident measurement, the incident angle is set close to the α_c because the penetration depth of X-ray is typically much larger than the thickness of the polymer films (*19*).

Due to the limited pixel size of the CCD detector, sample-to-detector (SSD) distance was modulated from 20 cm (GIWAXS, WAXS) to 3 m (SAXS, GISAXS) to maximize the resolution of the data. For long SSD distance, the detector is placed inside a vacuum flight tube because of absorption of X-ray in air. The typical q-ranges of 12-ID-B beamline at APS are 0.0035–0.9 $Å^{-1}$ for SAXS and GISAXS measurements and 0.4–2.8 $Å^{-1}$ to WAXS and GIWAXS measurements. Figure 2.12 shows a schematic illustration for GIWAXS and GISAXS measurements of polymer films.

Throughout the dissertation, the 2-D X-ray scattering data were converted to 1-D scattering profiles using Igor-pro based software NIKA(*20*). I used 2-D and 1-D X-ray scattering

data to characterize and analyze the structure factor and dynamics of thermal switching polymers under external stimuli, including magnetic field dependent molecular orientation (Chapter 3) and time-dependent structural evolution of polymers (Chapter 4).

2.7 FIGURES

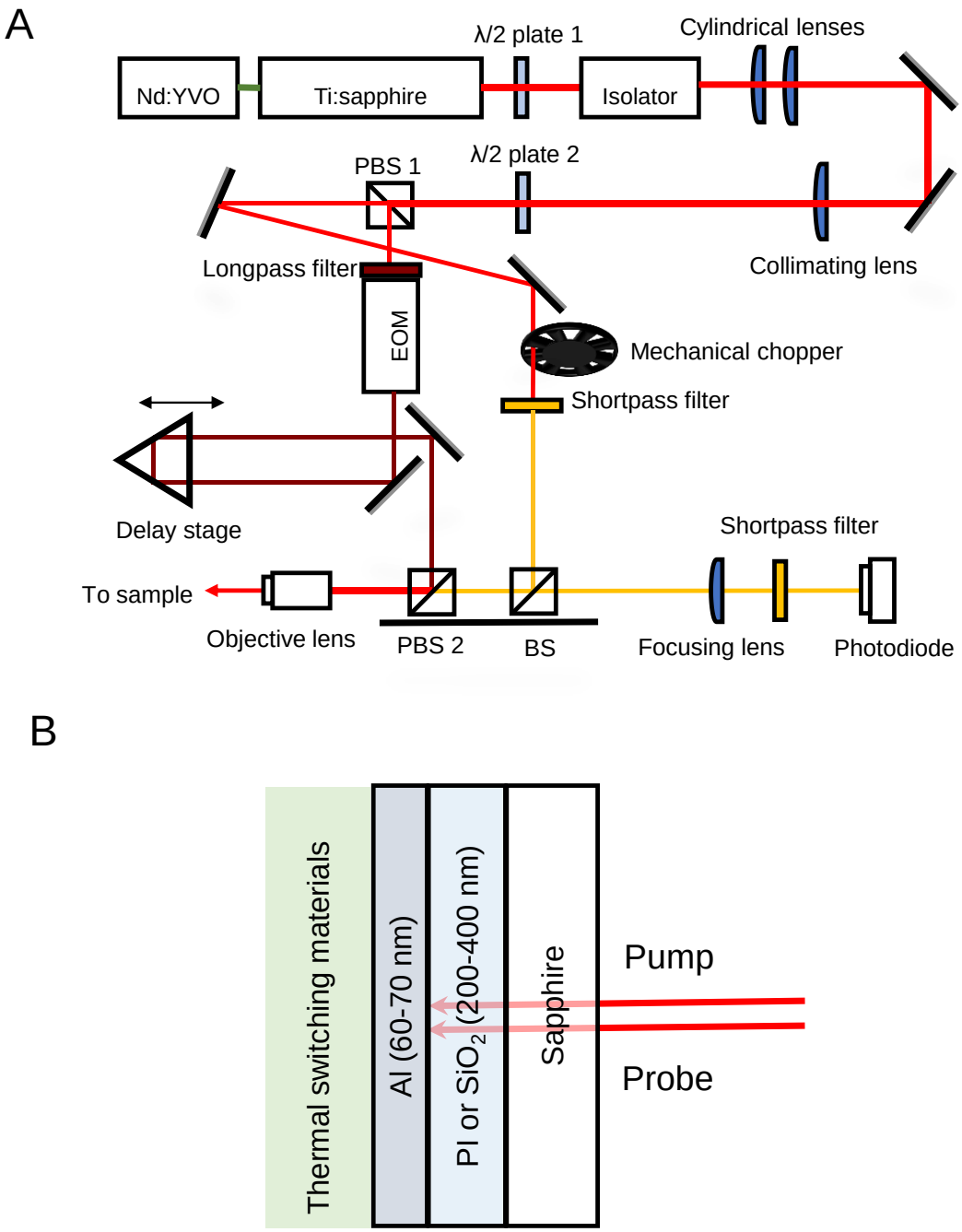

Figure 2.1. Thermal conductivity measurements of thermal switching materials (TSMs). **A.** Optical layout of TDTR system. **B.** Typical sample configuration for the backside TDTR measurements of TSMs.

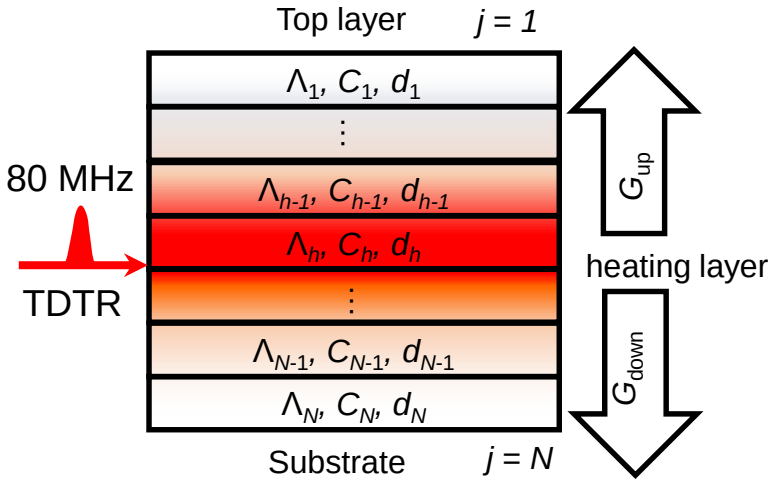

Figure 2.2. Schematic illustration of the bidirectional heat transport model. A train of pump pulses (f = 80 MHz) results in upward and downward heat flows from the lower interface of the heating layer (transducer film, $j = h$) to the top (j = 1) and bottom ($j = N$) layers with individual thermal parameters (Λ_j, C_j, d_j).

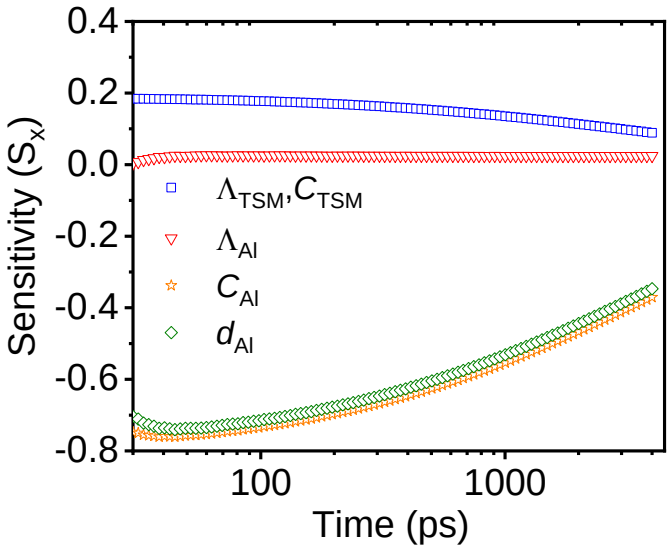

Figure 2.3. Calculated sensitivity curves for a polymer TSM/Al/PI/sapphire substrate at f = 10 MHz. Note that Λ_{TSM} and C_{TSM} exhibit identical sensitivity values as $f > \Lambda_{TSM} / (\pi C_{TSM} d_{TSM}^{2})$.

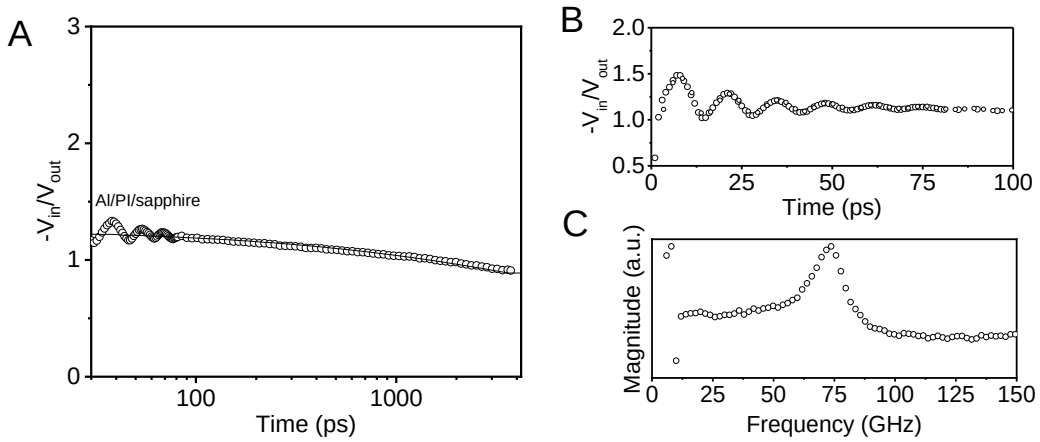

Figure 2.4. Characterization of Al/PI/sapphire substrates. **A.** Measured and fitted TDTR curves for an Al (50 nm)/PI (400 nm)/sapphire substrate at f = 10 MHz. **B.** A magnified TDTR curve shows a picosecond acoustic oscillation at low time delay. **C.** Fourier transformed TDTR signal in panel B.

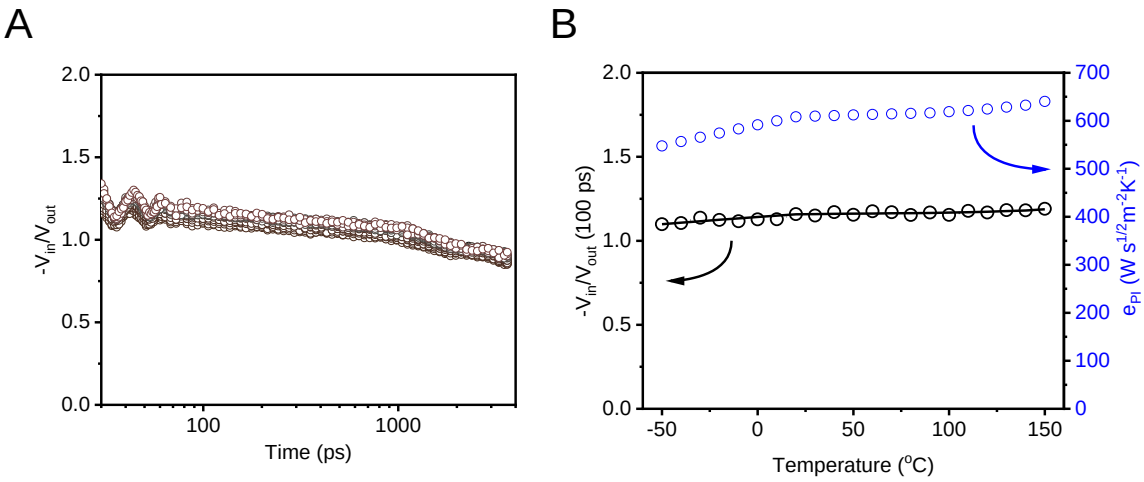

Figure 2.5. Thermal stability test of Al/PI/sapphire substrates. **A.** Measured TDTR curves for an Al/PI/sapphire substrate from –50 ºC to 150 ºC with temperature interval of 10 ºC. **B.** $-V_{in}/V_{out}$ values for an Al/PI/sapphire at t = 100 ps and calculated e_{PI} values of the PI layer as a function of temperature.

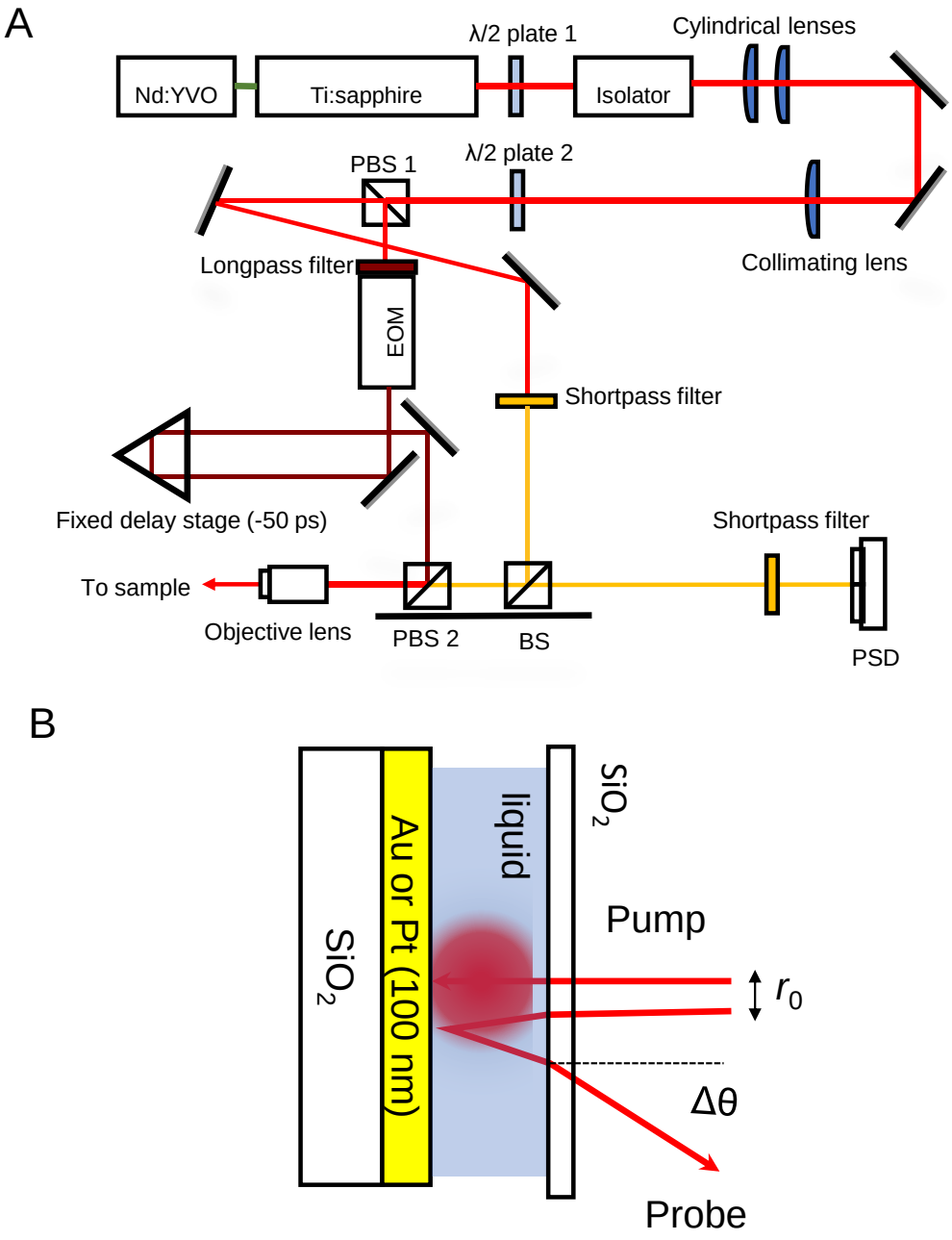

Figure 2.6. Thermal conductivity measurements for low Λ materials. **A.** Optical layout of FD-PBD system. **B.** Typical sample configuration for a FD-PBD measurement of a liquid.

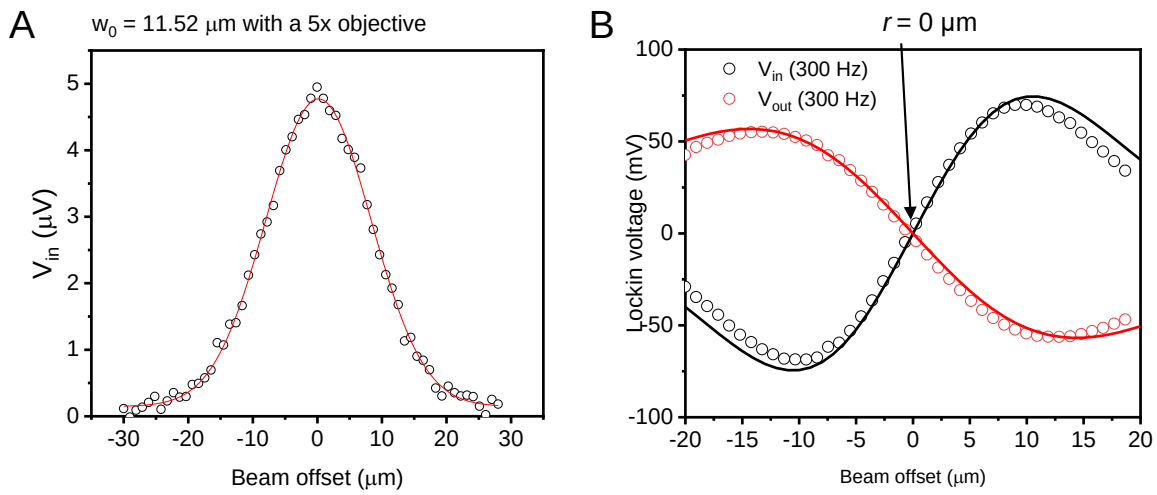

Figure 2.7. Beam size and beam offset calibrations for FD-PBD measurements. **A.** A measured beam offset TDTR curve and the Gaussian fitting for beam size calculation. **B.** Measured and fitted FD-PBD curves for DI-water/Au (100 nm)/SiO_2.

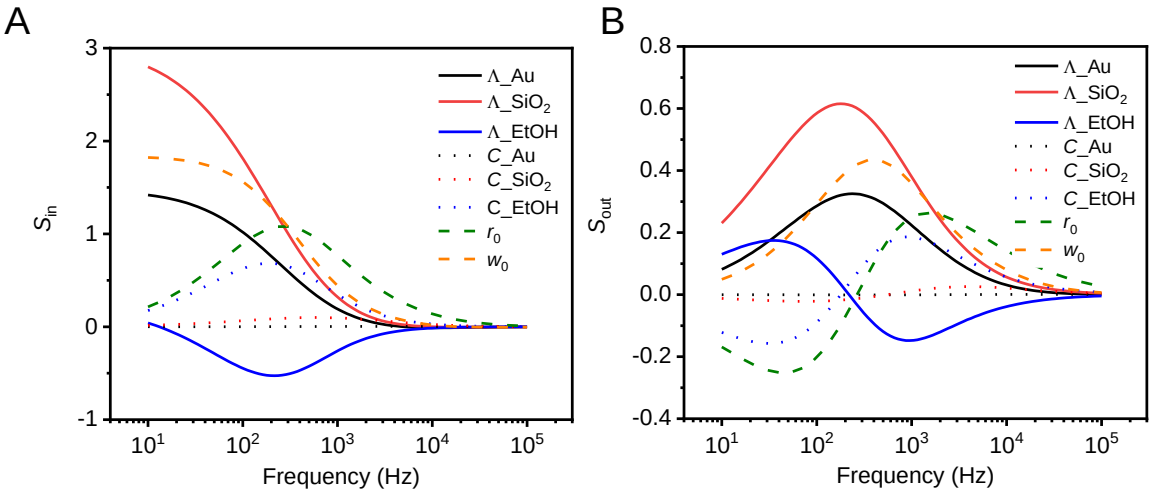

Figure 2.8. Sensitivity calculation for FD-PBD. **A.** In-phase and **B.** Out-of-phase FD-PBD sensitivity plots for r_0, w_0, and Λ and C of each layer (sample configuration: EtOH/Au/SiO_2).

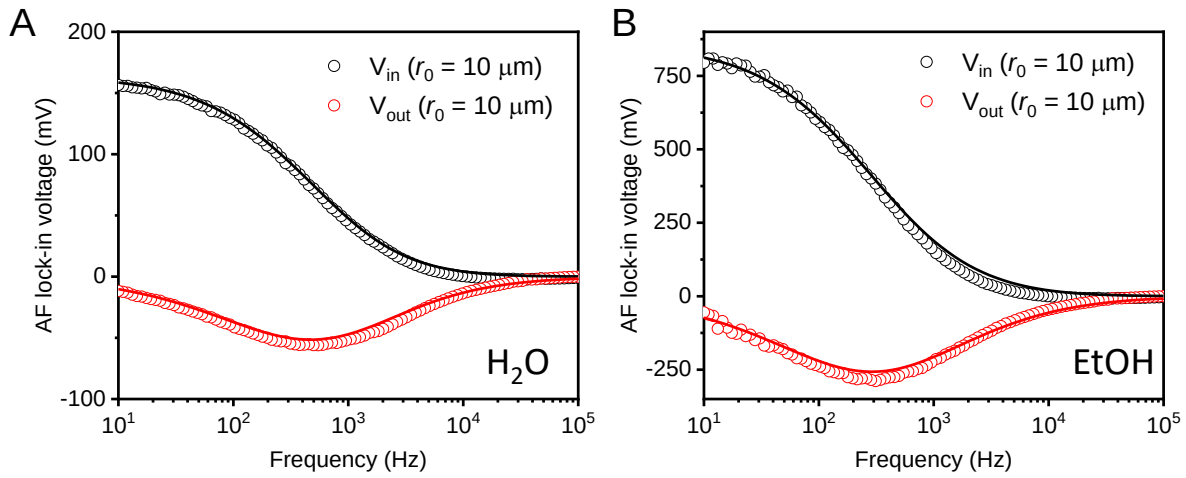

Figure 2.9. FD-PBD measurements for liquids. Measured and fitted FD-PBD curves for **A.** DI-water and **B.** EtOH at r_0 = 10 μm.

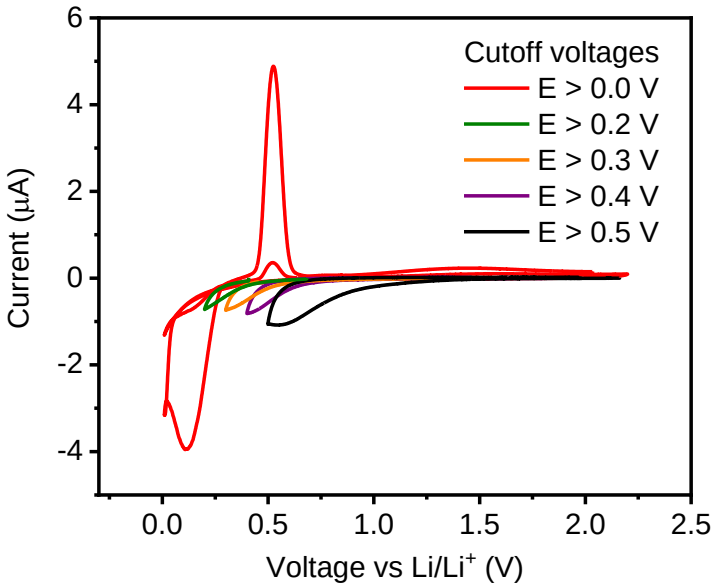

Figure 2.10. Electrochemical stability of Al film. Cyclic voltammetry data shows electrochemical redox peaks of Al below 0.2 V vs Li/Li^+. Above 0.2 V vs Li/Li^+, there is no specific redox peaks, indicating that Al film is electrochemically stable.

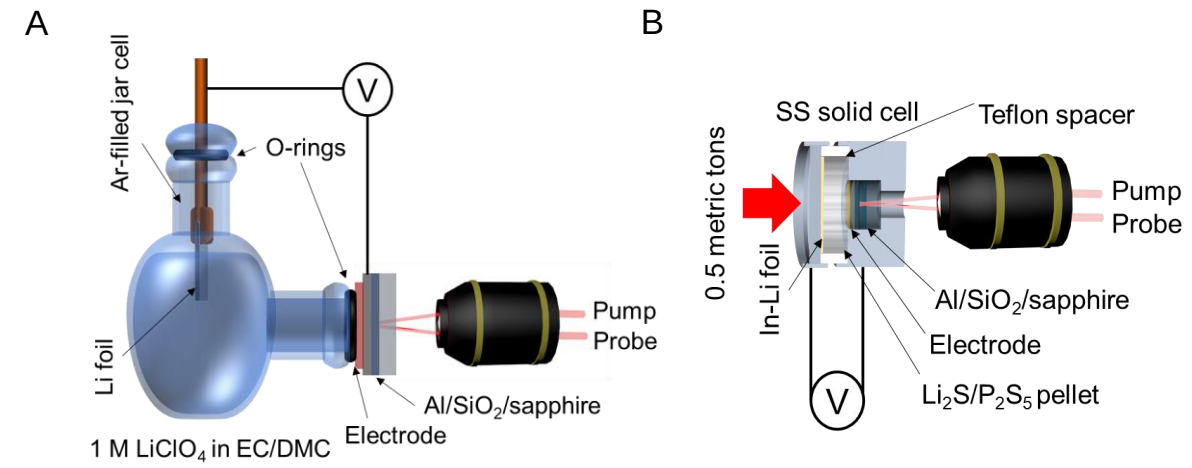

Figure 2.11. Schematic illustration for *in situ* TDTR measurement with custom-made liquid and solid electrochemical cells with Li-ion battery electrodes. **A.** Liquid electrolyte cells consist of Li metal foil as the counter electrode and the electrode material/Al/SiO_2/sapphire electrode as a working electrode. **B.** Solid electrolyte cells consist of Li metal foil as the counter electrode and the electrode material/Al/SiO_2/sapphire electrode as a working electrode. The transparent side of the electrode material/Al/SiO_2/sapphire substrate works as an optical window for the backside TDTR measurements.

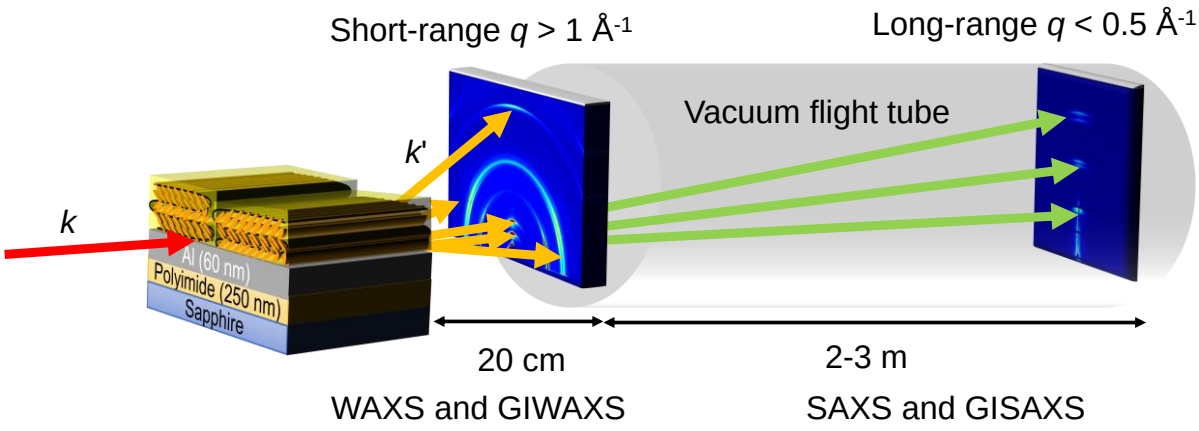

Figure 2.12. Schematic illustration for GIWAXS and GISAXS measurements of polymer film. The incident X-ray beam with a very small incident angle scattered on a surface of polymer film. The scattered X-ray intensity can be detected close to the sample (wide angle) and far from the sample (small angle). The pixel size and SSD of 2-D CCD detector define the resolution and *q*-range of the data.

2.8 REFERENCES

1. X. J. Wang, C. D. Liman, N. D. Treat, M. L. Chabinyc, D. G. Cahill, Ultralow thermal conductivity of fullerene derivatives. *Physical Review B* **88**, 075310 (2013).
2. S. Li *et al.*, High thermal conductivity in cubic boron arsenide crystals. *Science* **361**, 579-581 (2018).
3. K. Kang, Y. K. Koh, C. Chiritescu, X. Zheng, D. G. Cahill, Two-tint pump-probe measurements using a femtosecond laser oscillator and sharp-edged optical filters. *Rev Sci Instrum* **79**, 114901 (2008).
4. D. G. Cahill, Analysis of heat flow in layered structures for time-domain thermoreflectance. *Rev Sci Instrum* **75**, 5119 (2004).
5. J. Shin *et al.*, Thermally Functional Liquid Crystal Networks by Magnetic Field Driven Molecular Orientation. *Acs Macro Lett* **5**, 955-960 (2016).
6. X. Xie *et al.*, High and low thermal conductivity of amorphous macromolecules. *Physical Review B* **95**, 035406 (2017).
7. X. Xie, J. D. Dennison, J. Shin, Z. Diao, D. G. Cahill, Measurement of water vapor diffusion in nanoscale polymer films by frequency domain probe beam deflection. *Rev Sci Instrum* **89**, 104904 (2018).
8. Y. X. Wang, J. Y. Park, Y. K. Koh, D. G. Cahill, Thermoreflectance of metal transducers for time-domain thermoreflectance. *J Appl Phys* **108**, 043507 (2010).
9. R. B. Wilson, B. A. Apgar, L. W. Martin, D. G. Cahill, Thermoreflectance of metal transducers for optical pump-probe studies of thermal properties. *Opt Express* **20**, 28829 (2012).
10. Z. B. Ge, D. G. Cahill, P. V. Braun, Thermal conductance of hydrophilic and hydrophobic interfaces. *Phys Rev Lett* **96**, 186101 (2006).
11. X. Zheng, D. G. Cahill, R. Weaver, J. C. Zhao, Micron-scale measurements of the coefficient of thermal expansion by time-domain probe beam deflection. *J Appl Phys* **104**, 073509 (2008).
12. X. Xie, X. Zheng, R. Weaver, J. C. Zhao, D. G. Cahill, Micron-scale measurements of the coefficient of thermal expansion by time-domain probe beam deflection (vol 104, 073509, 2008). *J Appl Phys* **122**, 219901 (2017).

13. J. P. Feser, D. G. Cahill, Probing anisotropic heat transport using time-domain thermoreflectance with offset laser spots. *Rev Sci Instrum* **83**, 104901 (2012).
14. S. T. Myung, Y. Hitoshi, Y. K. Sun, Electrochemical behavior and passivation of current collectors in lithium-ion batteries. *J Mater Chem* **21**, 9891-9911 (2011).
15. D. W. Liu, G. Z. Cao, Engineering nanostructured electrodes and fabrication of film electrodes for efficient lithium ion intercalation. *Energ Environ Sci* **3**, 1218-1237 (2010).
16. M. Ko, S. Chae, J. Cho, Challenges in Accommodating Volume Change of Si Anodes for Li-Ion Batteries. *Chemelectrochem* **2**, 1645-1651 (2015).
17. X. H. Wu, M. El Kazzi, C. Villevieille, Surface and morphological investigation of the electrode/electrolyte properties in an all-solid-state battery using a Li_2S-P_2S_5 solid electrolyte. *J Electroceram* **38**, 207-214 (2017).
18. P. Willmott, An Introduction to Synchrotron Radiation: Techniques and Applications. *John Wiley and Sons Ltd*, (2011).
19. K. Yamamoto, Grazing-Incidence Small Angle X-Ray Scattering in Polymer Thin Films Utilizing Low-Energy X-Rays, X-ray Scattering. *Alicia Esther Ares, IntechOpen*, Chapter 3 (2017).
20. J. Ilavsky, Nika: software for two-dimensional data reduction. *J Appl Crystallogr* **45**, 324-328 (2012).

CHAPTER 3: THERMAL CONDUCTIVITY SWITCHING IN LIQUID CRYSTAL NETWORKS BY MAGNETIC FIELD DRIVEN MOLECULAR ORIENTATION

Chapters 3.1-3.6 were published in "Thermally functional liquid crystal networks by magnetic field driven molecular orientation," Jungwoo Shin, Minjee Kang, Tsunghan Tsai, Cecilia Leal, Paul V. Braun, David G. Cahill, *ACS Macro Lett*. **5**, 955−96. (2016).

In Chapter 3, I designed and synthesized aligned liquid crystal networks by photopolymerization of liquid crystal (LC) monomers in the presence of magnetic fields. Grazing incident wide-angle X-ray scattering (GIWAXS) and TDTR were used to characterize the degree of molecular alignment of mesogen chains and thermal conductivity. Liquid crystal networks (LCNs) with mesogenic units aligned perpendicular and parallel to the substrate exhibit thermal conductivity of 0.34 W m^{-1} K^{-1} and 0.22 W m^{-1} K^{-1}, respectively. The thermal conductivity and orientational order of liquid crystal networks vary as a function of temperature, which can be also manipulated by a magnetic field at above the glass transition temperature (65 ^{o}C) where the reduced viscosity enables molecular reorientation on the time scale of 10 min.

3.1 ANISOTROPIC THERMAL CONDUCTIVITY OF LIQUID CRYSTALS

Liquid crystals (LCs) have an anisotropic thermal conductivity that can be switched through changes in molecular ordering (*1, 2*). 1,4-bis-[4-(3-acryloyloxypropyloxy)benzo-yloxy]-2-methylbenzene (RM257, Wilshire Technologies) is a polymerizable nematic liquid crystal reactive mesogen in the temperature range of 67 – 130 ^{o}C, which can be oriented by magnetic fields due to the anisotropic magnetic susceptibility $\Delta\chi = 1.1\times10^{-3}$ cm^{3} mol^{-1} (Figure 3.1) (*3*). Figure 3.2 shows optical microscopy (OM) images of RM257 at crystalline, nematic and isotropic liquid phases at each phase.

First of all, I measured the anisotropic thermal conductivity of nematic RM257 in the presence of magnetic fields perpendicular ($B_{\perp}$) and parallel ($B_{\parallel}$) to the Al/PI/sapphire substrate. RM257 was melted at 80 ^{o}C and injected into a cell consisting of an Al/PI/sapphire substrate and a glass slide. Figure 3.3A shows the thermal conductivity of RM257 under magnetic fields ($B_{\perp}$ and $B_{\parallel}$). Open circles and squares are independent data points measured by a continuous TDTR scan with a heating rate of 4 ^{o}C min^{-1} up to 120 ^{o}C and independent TDTR measurements at a fixed temperature (Figure 3.3B) at up to 110 ^{o}C, respectively in the presence of the perpendicular field ($B_{\perp}$). At the crystalline phase there is no difference in thermal conductivity values under $B_{\perp}$ and $B_{\parallel}$. The anisotropic thermal conductivity of nematic RM257 was 0.24 W m^{-1} K^{-1} and 0.14 W m^{-1} K^{-1} at 80 ^{o}C under $B_{\perp}$ and $B_{\parallel}$, respectively. The thermal conductivity of RM257 under $B_{\perp}$ and $B_{\parallel}$ converges as it reaches the clearing temperature. This degree of anisotropy, approximately a factor of 2, is similar to other reported values of nematic LCs(*1, 2*).

3.2 SYNTHESIS OF MAGNETICALLY ALIGNED LIQUID CRYSTAL NETWORKS (LCNS)

As discussed in Chapter 3.1, the anisotropic thermal conductivity of LCs can be utilized for thermally switching materials. When polymerized, the molecular ordering of LC mesogen units in LCNs can be manipulated by external stimuli such as thermal, electric, magnetic and optical fields (*4*). In Chapter 4.1, I describe a method to prepare thermally switching polymeric materials based on RM257 LCNs modulated by a magnetic field.

The magnetically aligned LCNs were prepared by photopolymerization of RM257 with a thiol cross-linker (pentaerythritol tetrakis[3-mercaptopropionate]) (PETMP, Sigma Aldrich) in the presence of magnetic fields. The thiol-ene cross-linking reaction between PETMP and RM257 results in an increase of the toughness of the material at $T<T_g$ and creates an elastomer at $T>T_g$. Without the cross-linking agent, RM257 forms a brittle solid up to 250 ^oC.

First, an LC solution was prepared by mixing RM257 with 5 mol% of PETMP and photoinitiator (2-hydroxy-2-methylpropiophenone, HHMP, 0.3 wt%) at 80 ^oC. Then, I prepared a thin film of LC solution by a drop-casting method. Figure 3.4 shows the drop-casting procedure: i) the LC solution was first dropped onto a glass slide; ii-iii) the glass slide was placed onto an Al/PI/sapphire substrate; iv) and the glass slide was used to cast an LC film across the Al/PI/sapphire substrate.

After the LC film casting, photopolymerization was performed for 20 min using a UV lamp (nominal wavelength 365 nm with a nominal power at the substrate of 3-20 mW cm^{-2}) at 80 ^oC forming a randomly cross-linked LCN film. A magnetic field was applied to the sample by N52 grade NdFeB magnets during photopolymerization. Figure 3.5 shows a schematic

illustration of molecular alignments of LCNs under magnetic fields perpendicular ($B_{\perp}$) and parallel ($B_{//}$) to the substrate (*5-7*). The typical sizes of samples are 1×1 cm^2 and 1×0.2 cm^2 for perpendicular ($B_{\perp}$) and parallel ($B_{//}$) field alignments, respectively. The magnetic field strength at the surface of a SmCo magnet is 0.4 T and the magnet field between two parallel NdFeB magnets is 0.7 T as measured by a DC gaussmeter (AlphaLab, GM-1-ST).

3.3 THERMAL CONDUCTIVITY OF ALIGNED LCNS

Thermal conductivity of aligned LCNs was measured by the backside TDTR with f = 9.1 MHz and w_0 and w_1 = 10 μm (*8, 9*). During the measurement, I manipulated molecular orientation using the magnetic field by SmCo permanent magnets (B ~ 0.4 T), which can operate at elevated temperatures up to 320 ºC (Figure 3.6A). The measured and fitted TDTR data are shown in Figure 3.6B. Compared with the RM257 monomer, thermal conductivity was increased by 0.1 $W\,m^{-1}\,K^{-1}$ in both directions with the formation of chemical bonds between the monomers (*10*). The thermal conductivity of LCNs aligned perpendicular and parallel to the substrate was measured to be 0.34 ± 0.05 $W\,m^{-1}\,K^{-1}$ and 0.22 ± 0.02 $W\,m^{-1}\,K^{-1}$, respectively, with a standard deviation of ~ 10 % for 10 samples.

Due to the thermotropic nature of LCN, the molecular ordering and thermal conductivity of LCNs depend on temperature. Figure 3.7 shows two sets of TDTR data measured at from the room temperature to 200 °C for LCNs aligned perpendicular to the substrate. First, individual measurements were done at fixed temperatures (Figure 3.8) and converted to thermal conductivity (open squares) with time intervals of 10 min. The thermal conductivity measured by *in situ* TDTR measurement with a constant heating and cooling rate of 4 °C min^{-1} is plotted in the same graph (small circles). Both measurements showed that that

the high thermal conductivity state is lost at above 120 ºC followed by a large hysteresis on cooling. I attribute this decrease in thermal conductivity to the loss of molecular ordering at above glass transition temperature (*11*).

The glass transition temperature of LCN of LCN was characterized by Differential Scanning Calorimetry (DSC) (Q20 DSC, TA instruments). An endothermic peak marked with an arrow in Figure 3.9 indicates the glass transition temperature at 65 ºC, which is in the typical range of 40–120 ºC for LCNs (*4*).

On the contrary, LCNs can maintain the thermal conductivity up to 200 ºC when a constant magnetic field is applied in the aligned directions upon heating. The thermal conductivity change can be suppressed in the presence of magnetic fields. Figure 3.10 shows that the thermal conductivity of LCNs polymerized under $B_{\parallel}$ and $B_{\perp}$ at temperatures up to 200 ºC. Contrary to the thermal conductivity decrease of LCNs without a magnetic field, the LCN polymerized under $B_{\perp}$ exhibited a slight increase in the thermal conductivity up to 150 ºC (blue dots) in the presence of $B_{\perp}$. Likewise, LCN polymerized under $B_{\parallel}$ exhibits a slight decrease in the thermal conductivity up to 150 ºC under the constant magnetic field ($B_{\parallel}$).

3.4 MAGNETIC FIELD DRIVEN MOLECULAR REORIENTATION OF LCNS

In collaboration with Minjee Kang in Leal group at Illinois, we performed GIWAXS measurement at 12-ID-B beamline at Advanced Photon Source. Figure 3.11 shows GIWAXS data and corresponding schematics of the mesogenic unit ordering of LCNs under $B_{\perp}$ and $B_{\parallel}$. Note that the backbone chains connecting mesogen units are omitted for clarity. The observed scattering peaks are typical of magnetically-aligned LCNs (*11*). Since three phenyl rings at the

core of RM257 are rotated by 24° with respect to each other (*5*) the primary GIWAXS peak at q ~ 1.53 $Å^{-1}$ corresponds to a plane spacing of 4.1 Å, 0.3 Å larger than typical for π-π stacking (*12, 13*). With the magnetic field applied perpendicular to the substrate ($B_{\perp}$) during polymerization, the π-π stacking peaks appear along the direction parallel to the substrate, indicating the vertical alignment of mesogen units in the LCN, see Figure 3.11A.

Perpendicular and parallel GIWAXS measurements with respect to the magnetic field direction ($B_{//}$) were performed to prove in-plane anisotropy of mesogens in LCN films. The different features of π-π stacking orientation distribution in Figure 3.11B-C reveal the nature of in-plane anisotropic alignment of mesogen units. The long optical axis of mesogens in each domain is aligned in the direction of the magnetic field while π-π stacks have no preferential orientation around the optical axis, resulting in the isotropic ring pattern with an incident beam along with the aligned direction (Figure 3.11C). Note that GIWAXS data of RM257 solidified in a magnetic field show similar molecular order as LCNs that are lightly cross-linked.

When heated above the glass transition temperature magnetically aligned LCNs can lose their nematic ordering. Figure 3.12A-B shows GIWAXS data for LCNs aligned perpendicular to the substrate at 25 °C and 150 °C. We observed an isotropic ring at 150 °C suggesting a loss of orientational and positional order. Unlike the sharp nematic-to-isotropic transition of small molecule LCs, the order-disorder transition of LCNs is gradual with temperature (*14*). We examined chain reorientation kinetics of LCNs by switching the magnetic field direction at the elevated temperature. The LCN aligned perpendicular to the substrate ($B_{\perp}$) was first heated to 200 °C and slowly cooled to room temperature in the presence of a magnetic field applied parallel to the substrate ($B_{//}$). The GIWAXS patterns

(Figure 3.12C) and azimuthal intensity at $q \sim 1.53$ Å^{-1} (Figure 3.12D) show that the scattering peak becomes wider and the center is tilted by 32° with respect to the initial state (Figure 3.12A).

Figure 3.13 shows thermal conductivity of LCN during magnetic reorientation. First, the LCN polymerized under a magnetic field parallel to the substrate ($B_{//}$) was heated to 150 °C (Figure 3.13A) followed by switching the orientation of the magnetic field ($B_{\perp}$). After the magnetic reorientation, the thermal conductivity of LCN increased gradually over a time span of 1500 s, see Figure 3.13B. The thermal conductivity shows a pronounced hysteresis upon cooling, resulting the room temperature thermal conductivity of 0.30 W m^{-1} K^{-1}, comparable to LCNs polymerized under a magnetic field ($B_{\perp}$, 0.34 W m^{-1} K^{-1}). The GIWAXS pattern after reorientation shows vertical molecular alignment as well (Figure 3.14).

The reorientation kinetics is controlled by the competition between the magnetic torque, $\Gamma_M = -1/2\mu_0^{-1}\Delta\chi B^2 sin(2\varphi)$ and the viscous drag $\Gamma_{vis} = -\eta_1(d\varphi/dt)$ where μ_0 is the permeability of vacuum, η_1 is the rotational viscosity, $\Delta\chi$ is the anisotropy of the magnetic susceptibility of the mesogen, and B is the applied magnetic field (*15, 16*). The relaxation time constant τ is (*17, 18*)

$$\tau = \left(\frac{2\mu_0\eta}{\Delta\chi B^2}\right) \tag{3.1}$$

The theoretical value of $\Delta\chi$ of RM257 is 1.1×10^{-3} cm^3 mol^{-1} (*3*). I measured the dynamic viscosity of the LCN by rotational oscillatory rheometry at 150 °C and found 4.5×10^3 Pa s. The rheological characterization of LCNs was carried out by a rotational rheometer (AR-G2, TA instruments) with coin-shaped LCN samples (25 mm in diameter, 1 mm in thickness). The

measurement was done in a linear viscoelastic regime with an oscillation strain of 1% and frequency of 10 rad s^{-1}. I calculate the average molecular weight between the cross-linkers, M_C, using an equation $M_C = \rho RT / G'$ where ρ is the density, R is the gas constant, T is the temperature and G' is the storage modulus. Samples show a slight variation about ~35% in G' indicating variations in the average distance between cross-linkers (in average, ~14 units of RM257).

Equation 3.1 predicts $\tau \sim 8\times10^3$ s (Figure 3.15), an order of magnitude higher than what I observe in the thermal conductivity measurements ($\tau \sim 700$ s, see Figure 3.13B). An order of magnitude discrepancy between measurements and the theory has been observed in other liquid crystal polymer systems which range from a few minutes for liquid crystal elastomers to a few tens of hours for block copolymers (*11, 15, 16, 18-22*).

3.5 THERMAL TRANSPORT MODEL FOR LCNS

To relate thermal conductivity and mesogen orientation of LCNs, I construct an effective medium model to provide insights into the dependence of thermal conductivity on molecular orientation. The model describes the LCN material as comprised of partially-ordered, cylindrical mesogens embedded in an isotropic amorphous polymer matrix. The fundamental thermal conductivity tensors of the mesogen are $\Lambda_{\text{In-plane}}$ and $\Lambda_{\text{Out-of-plane}}$.

The thermal conductivity of a partially-aligned aggregate of mesogens is a function of the order parameter S (*23-27*):

$$\Lambda_{B\perp}^{-1} = \frac{1}{3}\left(\Lambda_{\text{In-plane}}^{-1} + 2\Lambda_{\text{Out-of-plane}}^{-1}\right) + \frac{2}{3}S\left(\Lambda_{\text{In-plane}}^{-1} - \Lambda_{\text{Out-of-plane}}^{-1}\right) \tag{3.2}$$

$$\Lambda_{B//}^{-1} = \frac{1}{3}\left(\Lambda_{\text{In-plane}}^{-1} + 2\Lambda_{\text{Out-of-plane}}^{-1}\right) - \frac{1}{3}S\left(\Lambda_{\text{In-plane}}^{-1} - \Lambda_{\text{Out-of-plane}}^{-1}\right) \tag{3.3}$$

$$S = \frac{1}{2}\left(3\left\langle\cos^2\varphi\right\rangle - 1\right) \tag{3.4}$$

where φ is the angle between the long axis of the molecules and the magnetic field (*28*).

$$\left\langle\cos^2\varphi\right\rangle = \frac{\int_0^{\pi/2} f(\beta)\cos^2\beta\sin\beta d\beta}{\int_0^{\pi/2} f(\beta)\sin\beta d\beta} \tag{3.5}$$

where the orientational distribution function of the mesogen molecules *f(β)* is obtained from the azimuthal intensity *I(θ)* of the primary scattering peak (*28*).

$$I(\theta) = \sum_{i=0}^{\infty} f_{2i}\frac{2^i i!}{(2i+1)!!}cos^{2i}\theta \tag{3.6}$$

$$f(\beta) = \sum_{i=0}^{\infty} f_{2i}cos^{2i}\theta \tag{3.7}$$

The measured azimuthal intensity $I_{exp}(\theta)$ is a sum of *I(θ)* and background intensity I_{BG}. Here, I subtracted I_{BG} from the average value from the diffuse ring. Figure 3.16 shows the measured azimuthal intensity $I_{exp}(\theta)$ and calculated order parameters from curve fitting (solid line). Small deviations at the edge (θ = 0 ^{o} and 180^{o}) are attributed to the shaded area of the detector at lower angles. In both cases, I calculate S = 0.6 as the order parameters for LCNs aligned parallel ($B_{\parallel}$) and perpendicular ($B_{\perp}$) to the substrate (Figure 3.16).

I included the flexible chain segments of the mesogens and cross-linkers to the effective medium model as an isotropic polymer matrix. The constructed effective medium model for cylindrical LC molecules embedded in an isotropic matrix (*29*, *30*) predicts that the effective thermal conductivity of LCNs under magnetic field parallel ($B_{\parallel}$) and perpendicular ($B_{\perp}$) is:

$$\Lambda_{\mathrm{LCN},B//} = (1-\Phi)\Lambda_{\mathrm{medium}} + \Phi\Lambda_{B//} \tag{3.8}$$

$$\Lambda_{\mathrm{LCN},B\perp} = (1-\Phi)\Lambda_{\mathrm{medium}} + \Phi\Lambda_{B\perp} \tag{3.9}$$

where Φ is the volume fraction of rigid core of mesogen and $\Lambda_{\mathrm{medium}}$ is thermal conductivity of the isotropic polymer matrix. I estimate Φ by

$$\Phi = \frac{(1-C)(M_{\mathrm{RC}}/\rho_{\mathrm{RC}})}{(1-C)(M_{\mathrm{LC}}/\rho_{\mathrm{LC}}) + C(M_{\mathrm{C}}/\rho_{\mathrm{C}})} \tag{3.10}$$

where M_{LC} M_{RC} and M_{C} are the molecular weights of the LC monomer, rigid core of mesogen, and cross-linker, respectively; ρ_{LC}, ρ_{RC} and ρ_{C} are their mass densities; and C is the cross-linker concentration. The volume fraction taken by rigid cores is Φ = 0.6 for LCN with 5 mol% cross-linker. M_{LC} M_{RC} and M_{C} we used are 588.6, 488.7 and 362 g mol^{-1}; and ρ_{LC}, ρ_{RC} and ρ_{C} are 1.22, 1.28 and 1.20 g cm^{-3}, respectively.

Here, I modulated *S* of LCNs with a higher cross-linker concentration (up to 20 mol% PETMP) (*11*, *31*). GIWAXS data confirm the loss of orientational ordering at the high cross-linking density (Figure 3.17), which shows a ring pattern which indicates the absence of molecular ordering as shown at the 20 mol% cross-linker concentration. The thermal

conductivity of LCN with the 20 mol% cross-linker concentration is 0.2 W m^{-1} K^{-1} independent of the magnetic field during polymerization.

Figure 3.18A shows a schematic illustration of an isotropic medium of thermal conductivity Λ_{medium} embedding partially-ordered mesogens with the fundamental in-plane thermal conductivity, $\Lambda_{In\text{-}plane}$, and out-of-plane thermal conductivity, $\Lambda_{Out\text{-}of\text{-}plane}$. Figure 3.18B shows the measured and fitted azimuth integrated intensities and corresponding order parameters for magnetically aligned LCNs with different cross-linker concentrations. Figure 3.18C shows measured and calculated $\Lambda_{LCN,B\parallel}$ and $\Lambda_{LCN,B\perp}$ of LCNs with different cross-linker concentrations (circles) under magnetic fields by the constructed effective medium model (dashed lines). Here, I adjusted $\Lambda_{In\text{-}plane}$ and $\Lambda_{Out\text{-}of\text{-}plane}$ to match $\Lambda_{LCN,\,B\perp}$ for different values of S and Φ. Assuming Λ_{medium} = 0.2 W m^{-1} K^{-1}, a typical value of amorphous polymer chains, I estimate the fundamental in-plane thermal conductivity, $\Lambda_{In\text{-}plane,}$ and out-of-plane thermal conductivity, $\Lambda_{Out\text{-}of\text{-}plane}$, of perfectly aligned rigid core of LCN of 1.5 W m^{-1} K^{-1} and 0.15 W m^{-1} K^{-1}. Thus, I conclude that the contrast in the thermal conductivity change can be improved with a larger order parameter S and smaller isotropic component $(1-\Phi)$ but the upper limit on the contrast will be a factor of 10.

3.6 MESOGEN ORDERING NEAR THE SURFACE AND BULK

Near the surface, within the boundary layer, mesogenic units can exhibit local orientation that deviates from the bulk. The thickness of the boundary layer can make up a significant portion of the thermal penetration depth of the TDTR measurement (*3*). The effect of surface effect on thermal conductivity was examined by using surface-functionalized substrates. Al films with and without hydrophobic surface functional groups were prepared. The hydrophobic surface was

prepared by soaking a substrate in the 10 mM PFDTES (1H,1H,2H,2H-perfluorodecyltriethoxy-silane, Sigma Aldrich) in toluene for 4 h at room temperature. Then, the substrates were rinsed with toluene and ethanol and dried in a stream of dry N2 gas. The substrates were then heated in an oven at 100 ^{o}C for 1 h. Then I compared the TDTR data between LCNs on bare and functionalized substrates. However, I did not observe a significant difference in thermal conductivity for LCNs with or without surface functionalization of the substrates by PFDTES which greatly lowers surface anchoring energy. The lack of dependence on surface anchoring energy indicates that surface interactions are not affecting the TDTR measurement of the LCNs.

In the bulk state, I confirmed that mesogen units do not have preferential ordering without an aid of magnetic fields. To test the molecular ordering of LCNs prepared without magnetic fields, I carried out transmittance WAXS. I prepared bulk LCNs samples by filling an LC solution with a 0, 5 and 20 mol % cross-linker in capillary tubes followed by UV polymerization at nematic (80 ^{o}C) and isotropic (140 ^{o}C) temperatures. Figure 3.19 shows that bulk LCNs at the nematic temperature (80 ^{o}C) and isotropic temperature (140 ^{o}C) exhibited isotropic ring patterns in WAXS measurements without preferred orientation. A slight decrease in diffraction intensity was observed for LCNs prepared at 140 ^{o}C compared to 80 ^{o}C. Although the bulk LCNs might comprise a substantial amount of unreacted RM257 monomer, I observed that they evolve to an isotropic state without displaying residual ordering.

3.7 SUMMARY

In summary, magnetically aligned LCNs were synthesized via photo-polymerization of RM257 LCs in the presence of a magnetic field. Magnetically-aligned LCNs showed thermal conductivity of 0.34 W m^{-1} K^{-1} and 0.22 W m^{-1} K^{-1}, respectively, for magnetic fields applied

perpendicular and parallel to the substrate during polymerization. The 50% increase in thermal conductivity depends on the molecular orientation assisted by magnetic fields, which can be further manipulated by temperature and magnetic field at above the glass transition temperature on a time scale of tens of minutes.

3.8 FIGURES

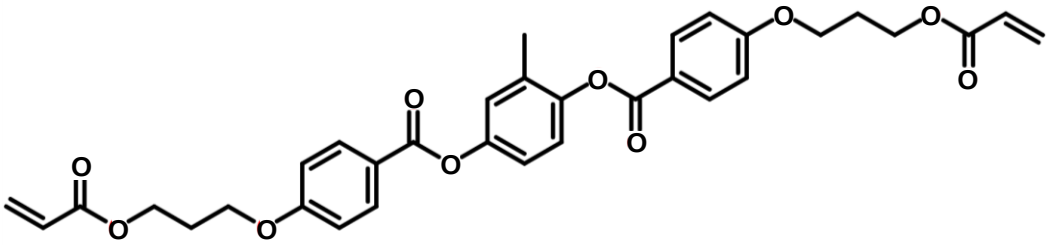

Figure 3.1. Chemical structure of RM257.

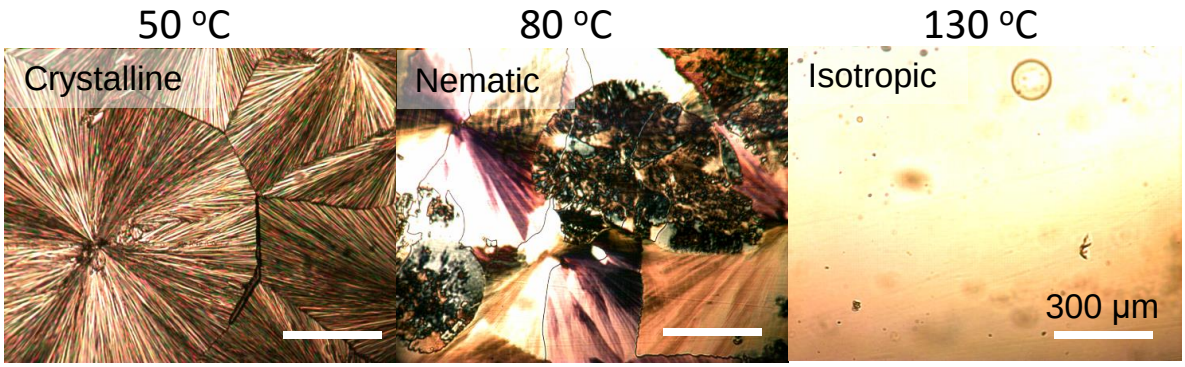

Figure 3.2. Optical microscopy (OM) images of RM257 at the crystalline phase (50 °C), nematic phase (80 °C) and isotropic liquid phase (130 °C).

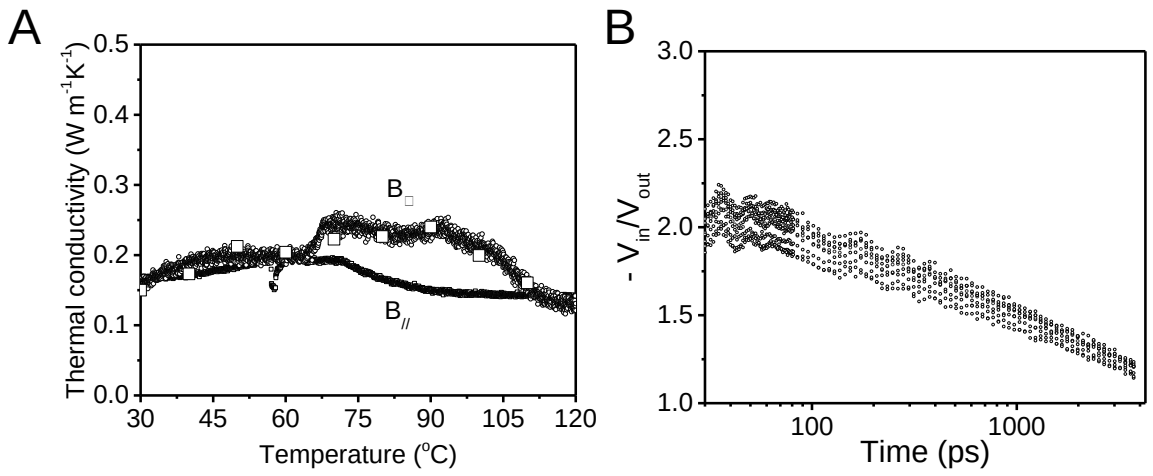

Figure 3.3. Anisotropic thermal conductivity of RM257. **A.** Thermal conductivity of RM257 in the presence of magnetic fields parallel ($B_{\parallel}$) and perpendicular ($B_{\perp}$) to the Al/PI/sapphire substrate. **B.** Independent TDTR data at fixed temperatures from 30 °C to 110 °C in the presence of a perpendicular field ($B_{\perp}$). Thermal conductivity values of each measurement are plotted as open squares in panel A.

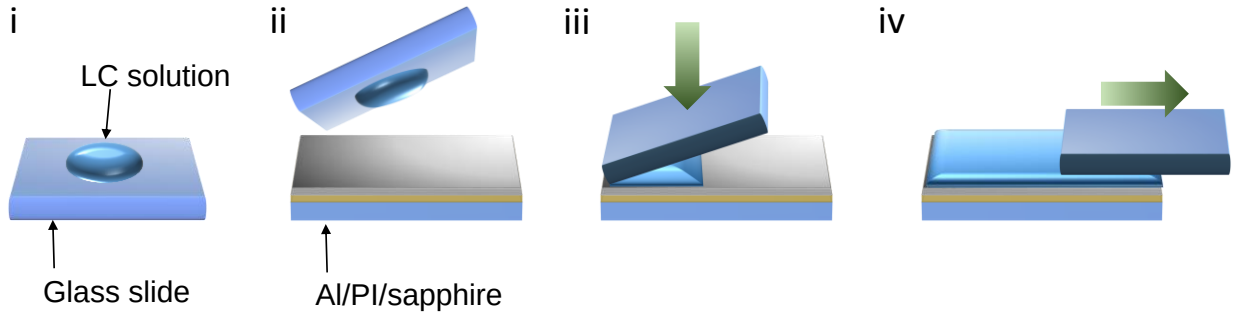

Figure 3.4. Schematic illustration for casting a LC solution on an Al/PI/sapphire substrate.

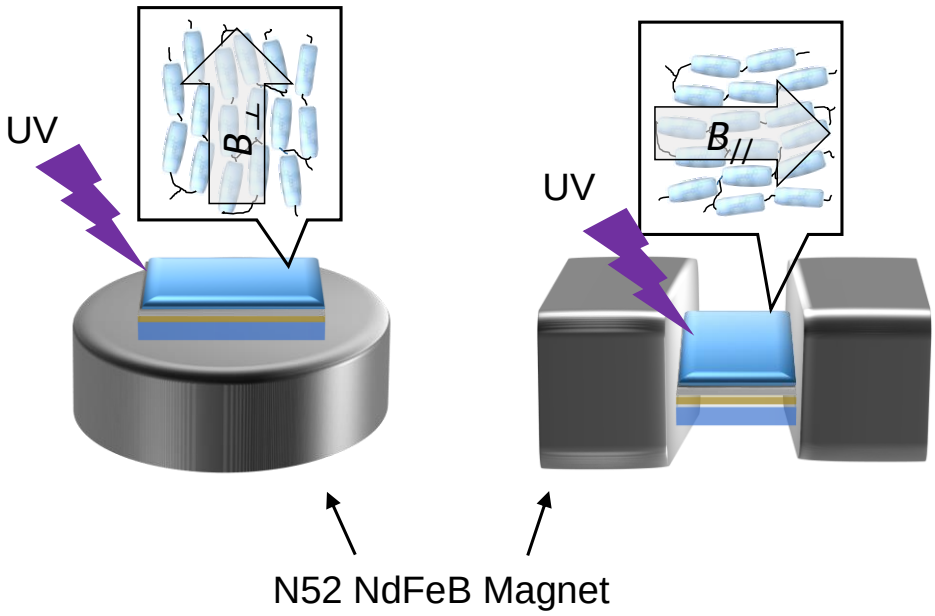

Figure 3.5. Schematic illustration for molecular alignments of LCNs during UV photopolymerization of drop-casted LC films under perpendicular ($B_{\perp}$) and parallel ($B_{\parallel}$) magnetic fields.

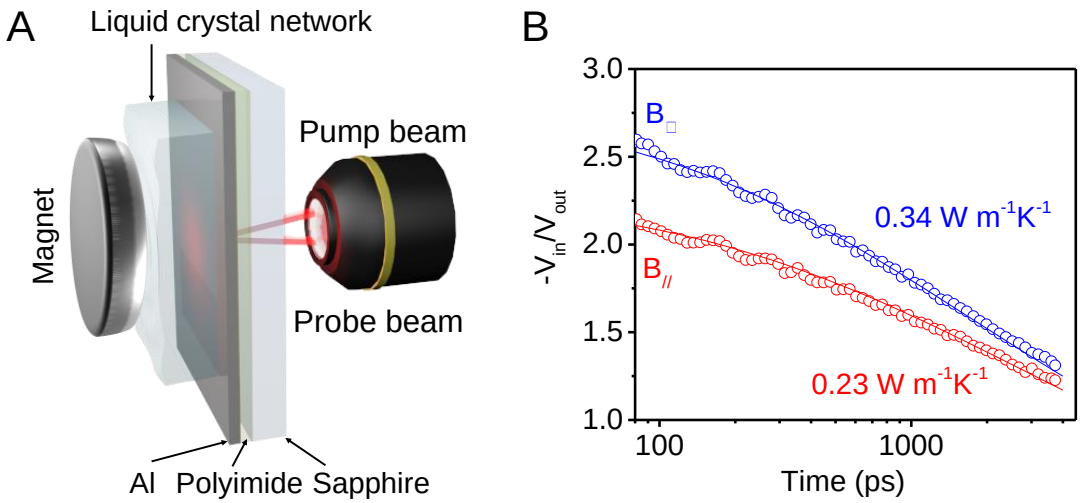

Figure 3.6. Thermal conductivity measurement of aligned LCNs by backside TDTR. **A.** Schematic illustration of TDTR measurement for LCN/Al/polyimide/sapphire samples under a perpendicular magnetic field $B_{\perp}$ applied by a permanent magnet. **B.** Measured and fitted TDTR data for LCNs polymerized under parallel ($B_{\parallel}$) and perpendicular ($B_{\perp}$) magnetic fields.

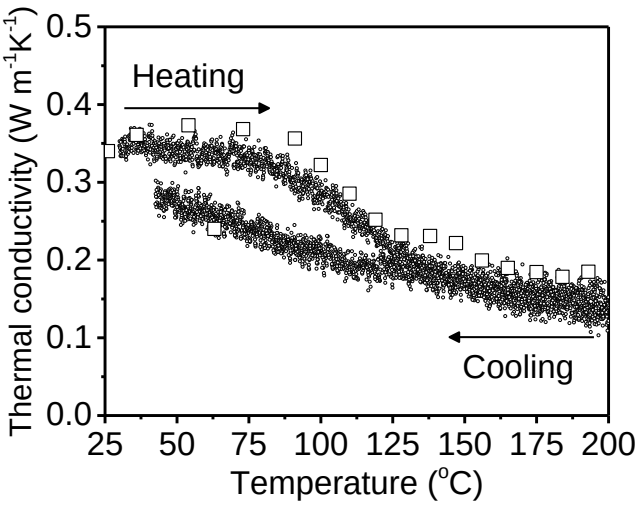

Figure 3.7. Temperature effect on thermal conductivity of LCNs. TDTR data for the perpendicularly aligned LCN ($B_{\perp}$) measured at fixed temperatures from room temperature to 200 ^{o}C (open squares) and continuous temperature measured by a continuous measurement with a heating rate of 4 ^{o}C min^{-1} (dots).

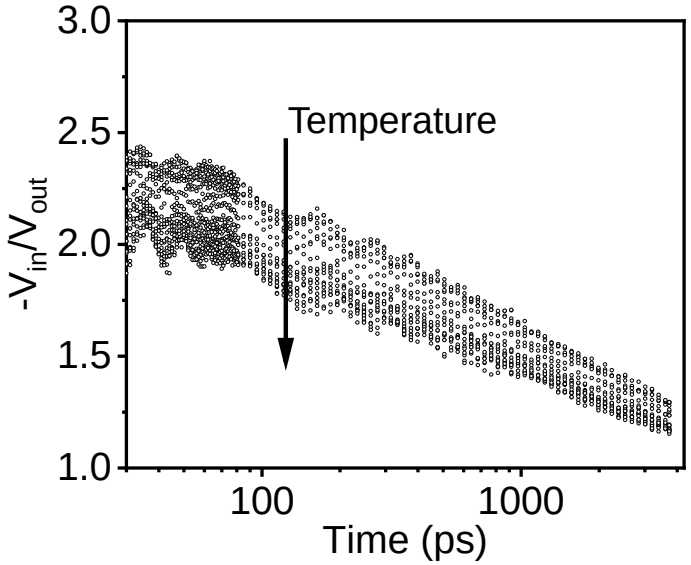

Figure 3.8. A set of TDTR data for LCN polymerized under $B_{\perp}$ at fixed temperatures from room temperature to 200 ^{o}C. Each data set is converted to the open squares in the thermal conductivity plot in Figure 3.7.

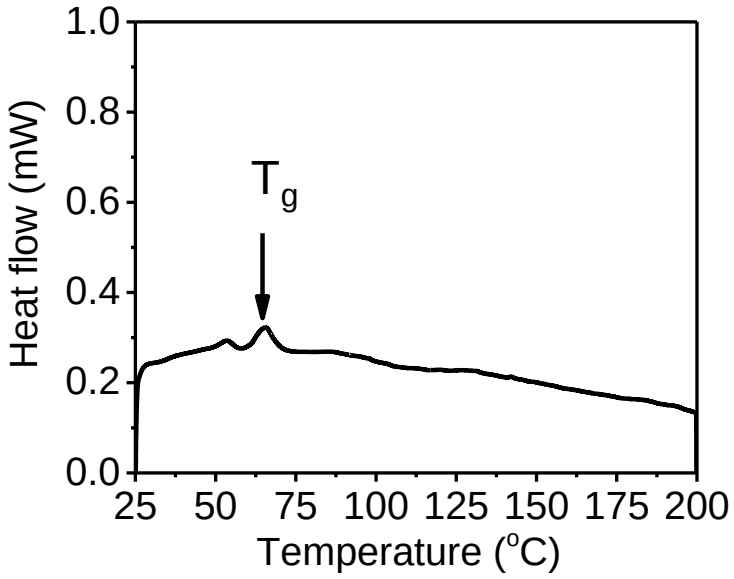

Figure 3.9. DSC data of LCN with a scanning rate of 4 °C min^{-1}.

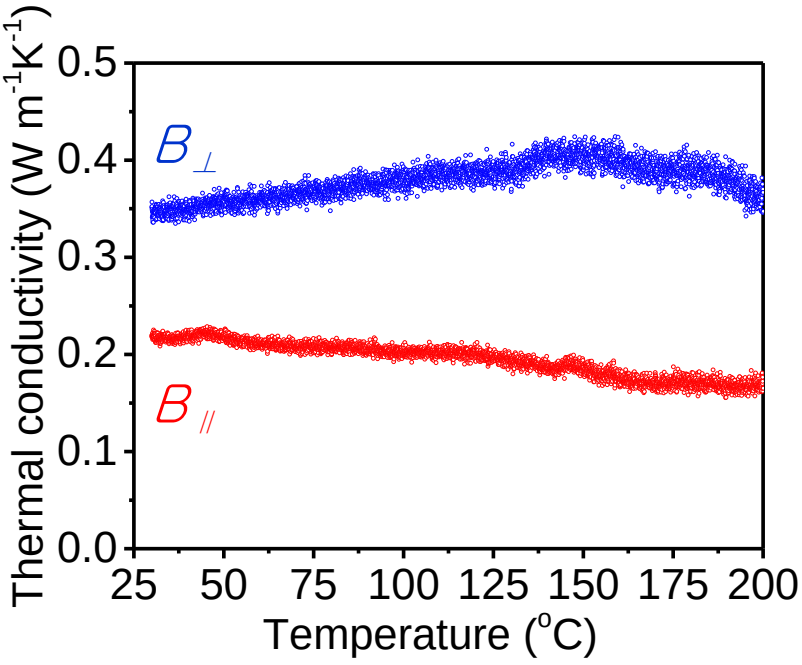

Figure 3.10. Thermal conductivity of LCNs polymerized in the presence of magnetic fields perpendicular ($B_{\perp}$) and parallel ($B_{\parallel}$) to the Al/PI/sapphire substrate.

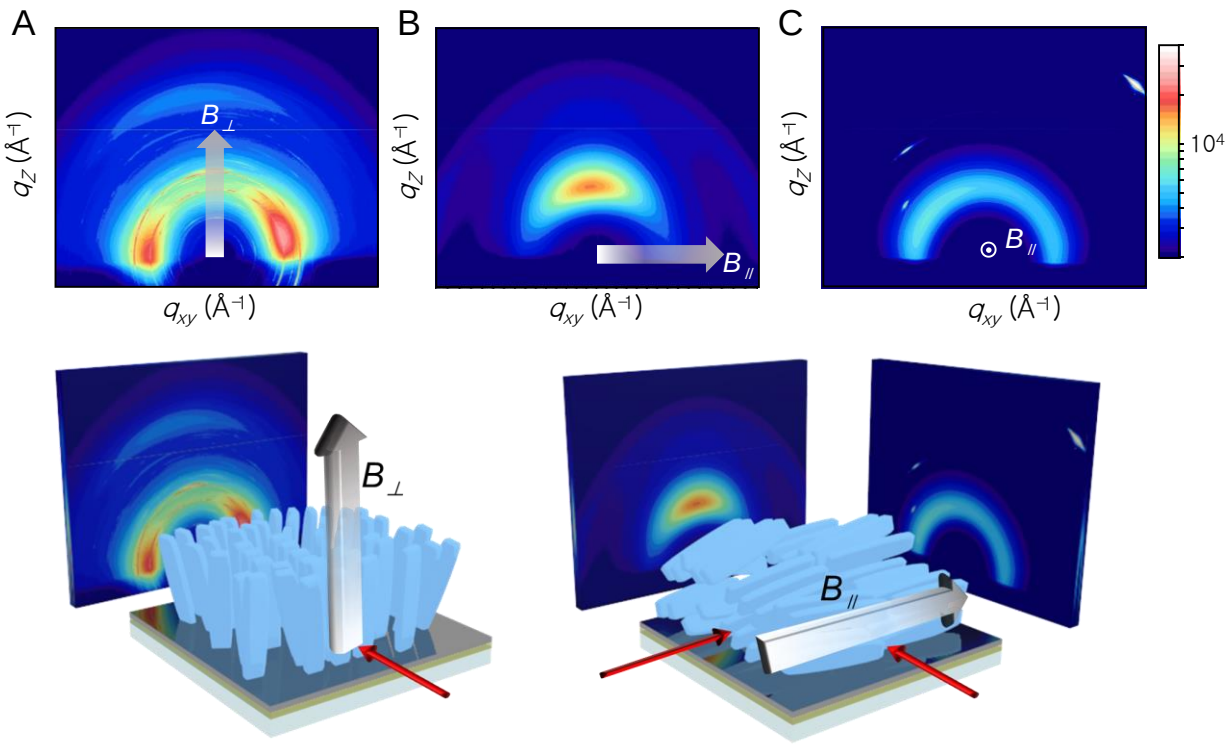

Figure 3.11. The effect of magnetic fields during polymerization on chain alignment**. A.** GIWAXS data for LCN polymerized with a magnetic field perpendicular to the substrate ($B_\perp$). **B. C.** GIWAXS data for LCN polymerized with a magnetic field parallel to the substrate ($B_{//}$). X-ray incident direction is represented as red arrows. In the figure, scattering vector q ($2\pi\ \lambda^{-1}$) ranged from -3 Å^{-1} to 3 Å^{-1} for the *xy* plane and 0 to 4 Å^{-1} for the *z* plane.

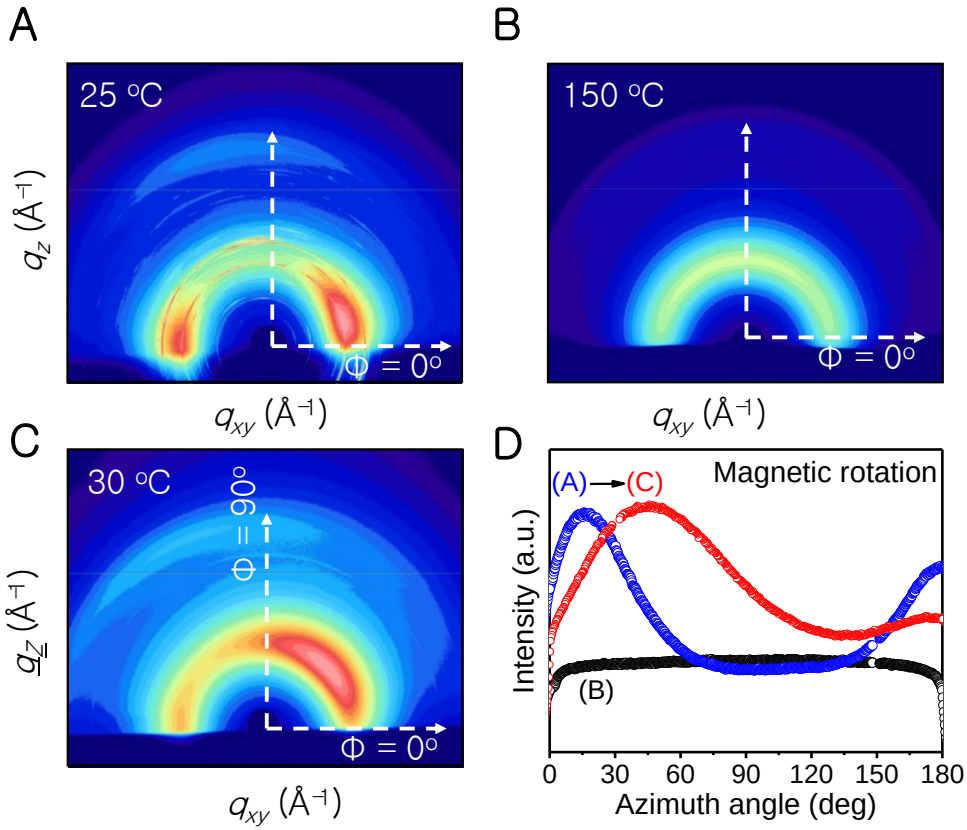

Figure 3.12. Temperature and magnetic field effect on molecular ordering. **A.** GIWAXS data for the LCN aligned perpendicular to the substrate ($B_{\perp}$) at 25 °C. **B.** GIWAXS data for the LCN aligned perpendicular to the substrate after heating up to 150 °C. I observe an order-disorder transition. **C.** GIWAXS data for the LCN after the magnetic reorientation ($B_{\parallel} \rightarrow B_{\perp}$). the LCN aligned perpendicular to the substrate ($B_{\parallel}$) was heating up to 150 °C then cooled down to the room temperature in the presence of a magnetic field parallel to the substrate ($B_{\perp}$). D. Azimuthal intensities of the LCN before and after the magnetic reorientation: (A), initial state at 25 °C, (B) after the complete loss of ordering at 150 °C and (C) 30 °C after the magnetic reorientation with $B_{\parallel}$. Φ represents the azimuth angle from the substrate.

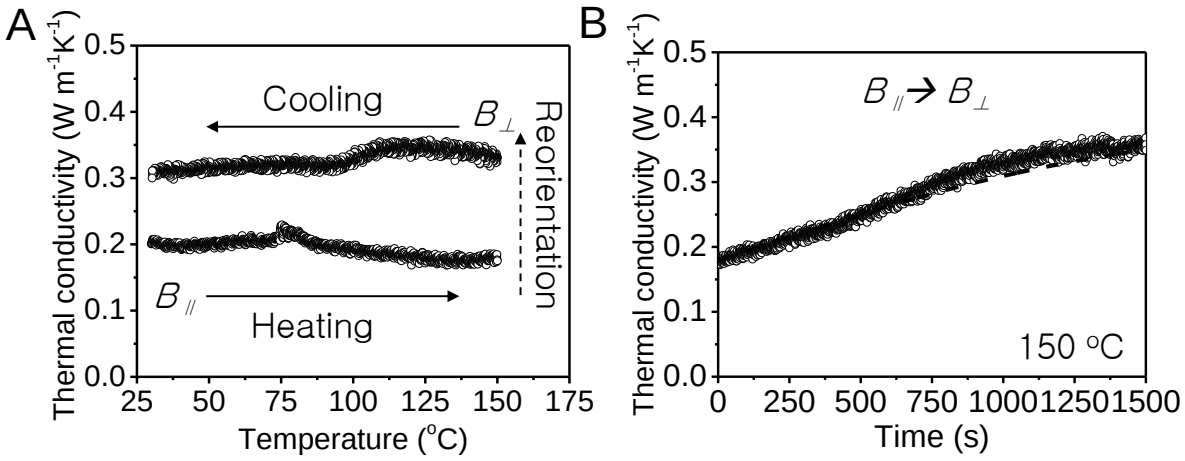

Figure 3.13. Effect of magnetic field on thermal conductivity of aligned LCN. **A.** Thermal conductivity of LCNs before and after magnetic reorientation. LCN polymerized under a parallel magnetic field ($B_{\parallel}$) was heated up to 150 °C with $B_{\parallel}$. After magnetic reorientation ($B_{\parallel} \rightarrow B_{\perp}$) it is slowly cooled down to room temperature. Heating and cooling rate is 4 °C min^{-1}. **B.** Thermal conductivity of a parallel aligned ($B_{\parallel}$) LCN in response to an orthogonal magnetic field ($B_{\perp}$) at 150 °C. The magnetic field was switched to the perpendicular direction ($B_{\perp}$) at 150 °C at t = 0 s.

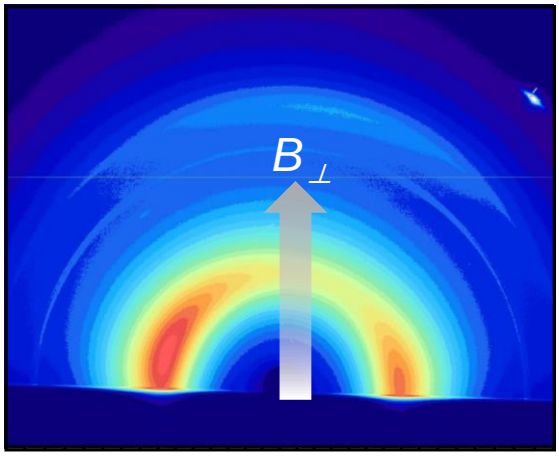

Figure 3.14. GIWAXS pattern after magnetic rotation. The magnetic field was changed from parallel ($B_{\parallel}$) to perpendicular ($B_{\perp}$) direction at elevated temperatures of 200 °C and slowly cooled to the room temperature. This image was taken at room temperature after the magnetic rotation. The scattering vector q (2π λ^{-1}) in this figure ranges from -3 Å^{-1} to 3 Å^{-1} in the xy plane and 0 Å^{-1} to 4 Å^{-1} in the z plane.

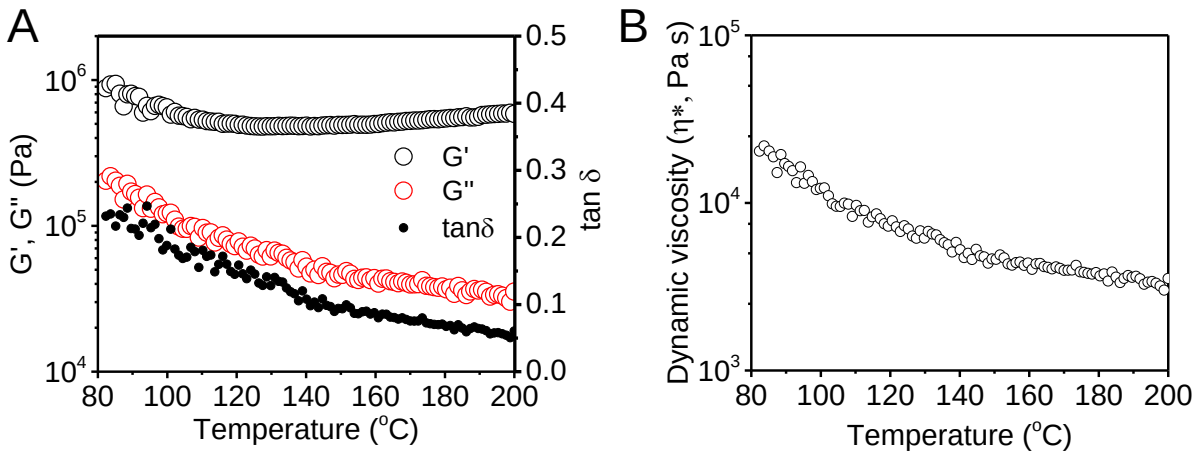

Figure 3.15. A. Storage modulus G', loss modulus G'' and tan δ of the LCN sample. **B.** Dynamic viscosity of the LCN measured by the oscillatory rotational rheometer.

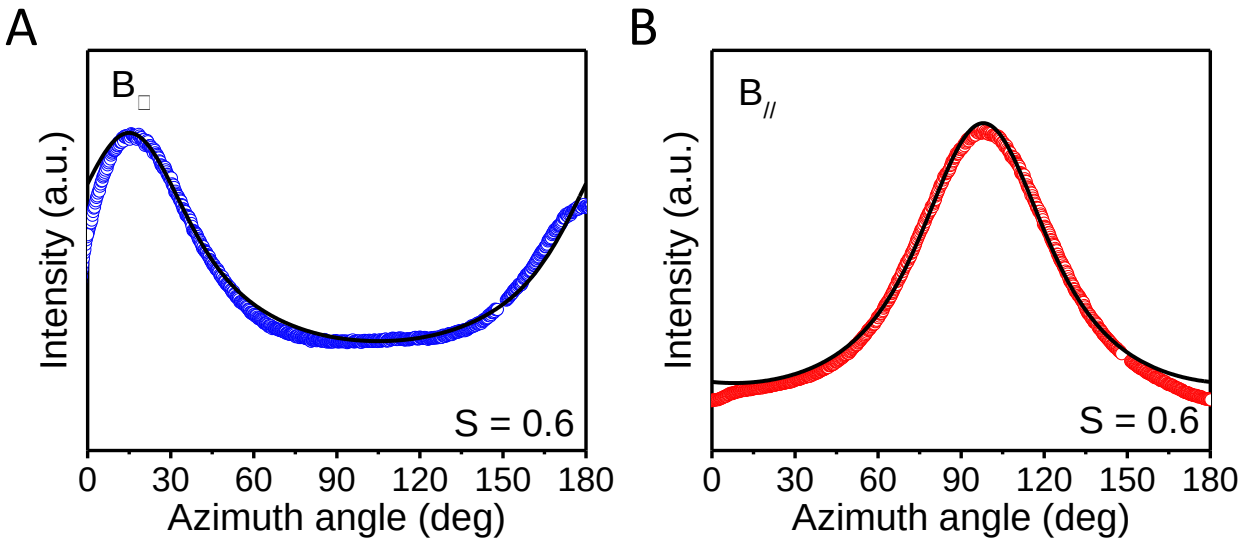

Figure 3.16. Azimuth integrated intensity and order parameter (*S*). **A.** Azimuth integrated intensity of LCNs polymerized in the presence of a magnetic fields perpendicular ($B_{\perp}$) to the substrate. **B.** Azimuth integrated intensity of LCNs polymerized in the presence of a magnetic field parallel ($B_{\parallel}$) to the substrate. Order parameters were obtained from curve fitting (solid lines).

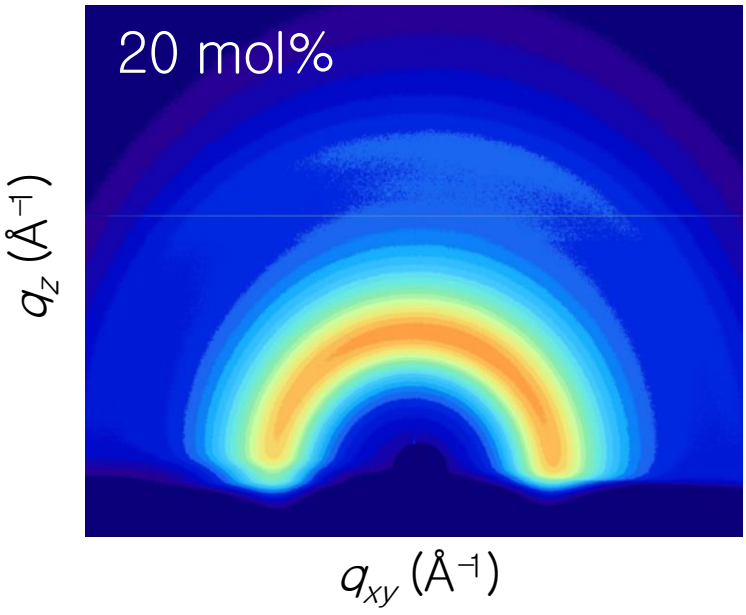

Figure 3.17. GIWAXS data for LCN with a cross-linker concentration of 20 mol%. The scattering vector q ($2\pi\,\lambda^{-1}$) in this figure ranges from -3 Å^{-1} to 3 Å^{-1} for the *xy* plane and 0 to 4 Å^{-1} for the *z* plane.

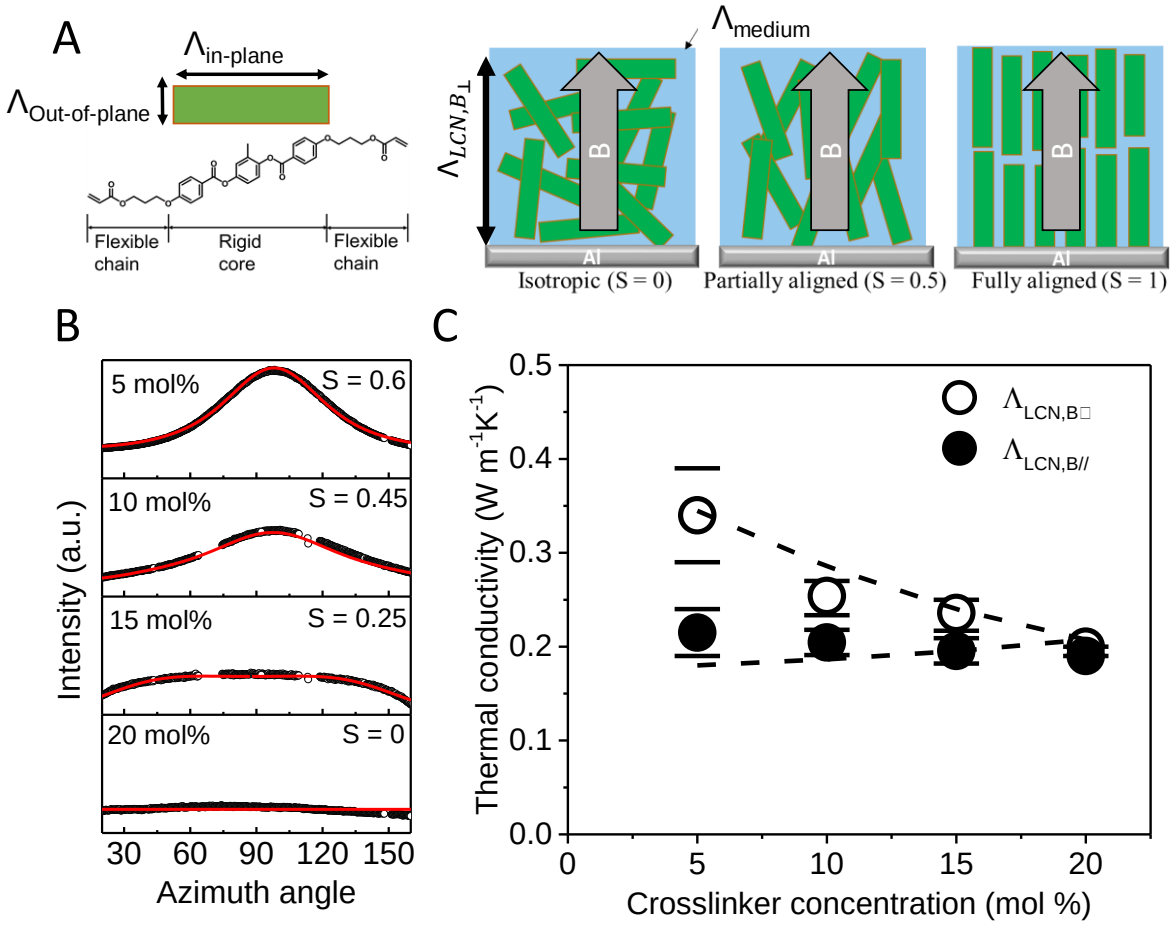

Figure 3.18. Thermal transport model for LCNs. **A.** Schematic illustration for the effective medium model for partially-ordered, anisotropic cylindrical mesogen units with the anisotropic thermal conductivity of $\Lambda_{\text{In-plane}}$ and $\Lambda_{\text{Out-of-plane}}$ embedded in an isotropic medium with a thermal conductivity of Λ_{medium}. **B.** The azimuth integrated intensities and calculated order parameters for LCNs polymerized with cross-linker concentrations of 5, 10, 15 and 20 mol%. **C.** Comparison between measured and calculated $\Lambda_{\text{LCN},B\parallel}$ and $\Lambda_{\text{LCN},B\perp}$ of LCNs polymerized under magnetic fields parallel ($B_{\parallel}$) and perpendicular ($B_{\perp}$) to the substrate as a function of cross-linker concentration. The dashed line is calculated from the effective medium model.

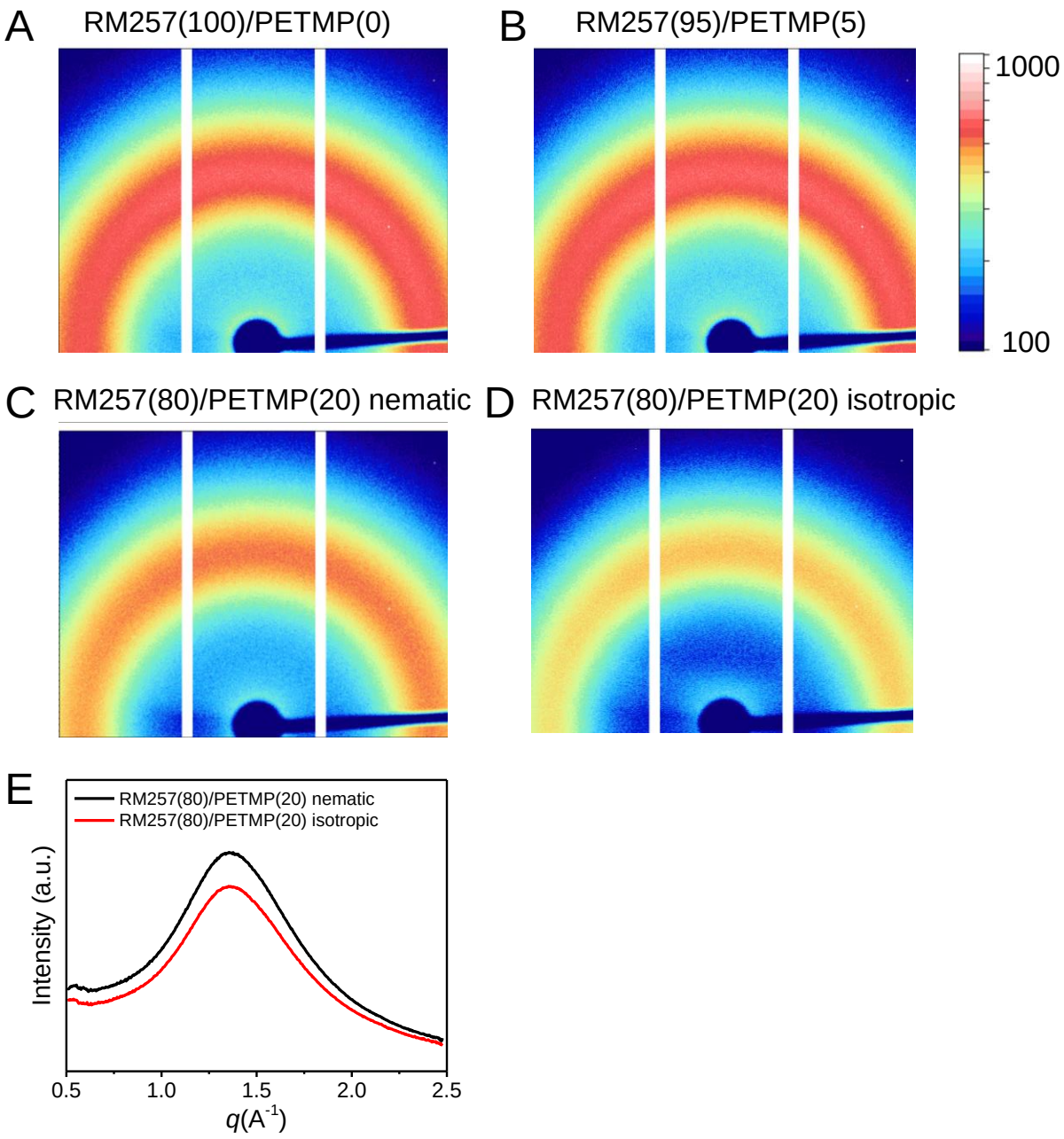

Figure 3.19. WAXS data for bulk LCNs prepared with a molecular ratio of RM257 to PETMP of **A.** 100/0, **B.** 95/5, and **C.** (80/20) at the nematic temperature (80 ^{o}C). D. WAXS data for bulk LCNs prepared with a molecular ratio of RM257 to PETMP (80/20) at the isotropic temperature (140 ^{o}C). E. Integrated WAXS intensity of bulk LCNs prepared with a molecular ratio of RM257 to PETMP of 80/20 at 80 ^{o}C and 140 ^{o}C.

3.9 REFERENCES

1. W. Urbach, H. Hervet, F. Rondelez, Thermal-Diffusivity Measurements in Nematic and Smectic Phases by Forced Rayleigh Light-Scattering. *Mol Cryst Liq Cryst* **46**, 209-221 (1978).
2. G. Ahlers, D. S. Cannell, L. I. Berge, S. Sakurai, Thermal-Conductivity of the Nematic Liquid-Crystal 4-N-Pentyl-4'-Cyanobiphenyl. *Phys Rev E* **49**, 545-553 (1994).
3. D. Demus, Goodby, J., Gray, G. W., Spiess, H.-W., Vill, V., Handbook of Liquid Crystals Set. *WILEY-VCH Verlag GmbH*, (1998).
4. T. J. White, D. J. Broer, Programmable and adaptive mechanics with liquid crystal polymer networks and elastomers. *Nat Mater* **14**, 1087-1098 (2015).
5. D. J. Broer, G. N. Mol, G. Challa, Insitu Photopolymerization of Oriented Liquid-Crystalline Acrylates .5. Influence of the Alkylene Spacer on the Properties of the Mesogenic Monomers and the Formation and Properties of Oriented Polymer Networks. *Makromol Chem* **192**, 59-74 (1991).
6. R. A. M. Hikmet, J. Lub, D. J. Broer, Anisotropic Networks Formed by Photopolymerization of Liquid-Crystalline Molecules. *Adv Mater* **3**, 392-394 (1991).
7. H. Thiem, P. Strohriegl, M. Shkunov, I. McCulloch, Photopolymerization of reactive mesogens. *Macromol Chem Physic* **206**, 2153-2159 (2005).
8. D. G. Cahill, Analysis of heat flow in layered structures for time-domain thermoreflectance. *Rev Sci Instrum* **75**, 5119 (2004).
9. K. Kang, Y. K. Koh, C. Chiritescu, X. Zheng, D. G. Cahill, Two-tint pump-probe measurements using a femtosecond laser oscillator and sharp-edged optical filters. *Rev Sci Instrum* **79**, 114901 (2008).
10. O. Yamamoto, Thermal Conductivity of Cross-Linked Polymers. *Polym J* **2**, 509-517 (1971).
11. G. G. Barclay, S. G. Mcnamee, C. K. Ober, K. I. Papathomas, D. W. Wang, The Mechanical and Magnetic Alignment of Liquid-Crystalline Epoxy Thermosets. *J Polym Sci Pol Chem* **30**, 1845-1853 (1992).
12. G. B. McGaughey, M. Gagne, A. K. Rappe, pi-stacking interactions - Alive and well in proteins. *J Biol Chem* **273**, 15458-15463 (1998).

13. C. Janiak, A critical account on pi-pi stacking in metal complexes with aromatic nitrogen-containing ligands. *J Chem Soc Dalton*, 3885-3896 (2000).
14. D. C. Thomas, M.; Sánchez-Ferrer, A.; Mbanga, B. L.; Atherton, T. J.; Cebe, P., *Liquid Crystals* **43**, 112-123 (2016).
15. W. H. Dejeu, Physical-Properties of Liquid-Crystalline Materials in Relation to Their Applications. *Mol Cryst Liq Cryst* **63**, 83-109 (1981).
16. J. S. Moore, S. I. Stupp, Orientation Dynamics of Main-Chain Liquid-Crystal Polymers .2. Structure and Kinetics in a Magnetic-Field. *Macromolecules* **20**, 282-293 (1987).
17. K. Schmidt *et al.*, Scaling behavior of the reorientation kinetics of block copolymers exposed to electric fields. *Soft Matter* **3**, 448-453 (2007).
18. M. Gopinadhan, P. W. Majewski, Y. Choo, C. O. Osuji, Order-Disorder Transition and Alignment Dynamics of a Block Copolymer Under High Magnetic Fields by In Situ X-Ray Scattering. *Phys Rev Lett* **110**, 078301 (2013).
19. W. Bras *et al.*, Field-induced alignment of a smectic-A phase: A time-resolved x-ray diffraction investigation. *J Chem Phys* **121**, 4397-4413 (2004).
20. B. McCulloch *et al.*, Dynamics of Magnetic Alignment in Rod-Coil Block Copolymers. *Macromolecules* **46**, 4462-4471 (2013).
21. Y. Rokhlenko *et al.*, Magnetic Alignment of Block Copolymer Microdomains by Intrinsic Chain Anisotropy. *Phys Rev Lett* **115**, 258302 (2015).
22. C. Ohm, M. Brehmer, R. Zentel, Liquid Crystalline Elastomers as Actuators and Sensors. *Adv Mater* **22**, 3366-3387 (2010).
23. K. Kurabayashi, Anisotropic thermal properties of solid polymers. *Int J Thermophys* **22**, 277-288 (2001).
24. J. Hennig, Anisotropy and Structure in Uniaxially Stretched Amorphous High Polymers. *J Polym Sci Pol Sym*, 2751-2761 (1967).
25. C. L. Choy, Thermal-Conductivity of Polymers. *Polymer* **18**, 984-1004 (1977).
26. D. B. Mergenthaler, M. Pietralla, S. Roy, H. G. Kilian, Thermal-Conductivity in Ultraoriented Polyethylene. *Macromolecules* **25**, 3500-3502 (1992).
27. C. L. Choy, Y. W. Wong, K. W. E. Lau, G. W. Yang, A. F. Yee, Thermal-Conductivity and Thermal Expansivity of Thermotropic Liquid-Crystalline Polymers. *J Polym Sci Pol Phys* **33**, 2055-2064 (1995).

28. P. Davidson, D. Petermann, A. M. Levelut, The Measurement of the Nematic Order-Parameter by X-Ray-Scattering Reconsidered. *J Phys Ii* **5**, 113-131 (1995).
29. S. J. Cox, V. Y. Reshetnyak, T. J. Sluckin, Effective medium theory of light scattering in polymer dispersed liquid crystal films. *J Phys D Appl Phys* **31**, 1611-1625 (1998).
30. K. Pietrak, T. S. Wisniewski, A review of models for effective thermal conductivity of composite materials. *J Power Technol* **95**, 14-24 (2015).
31. S. Dey *et al.*, Soft Elasticity in Main Chain Liquid Crystal Elastomers. *Crystals* **3**, 363-390 (2013).

CHAPTER 4: THERMAL CONDUCTIVITY SWITCHING IN AZOBENZENE POLYMERS VIA A LIGHT-TRIGGERED REVERSIBLE CRYSTAL-TO-LIQUID TRANSITION

Parts of Chapter 4 were published in "Light-triggered thermal conductivity switching in azobenzene polymers," Jungwoo Shin, Jaeuk Sung, Minjee Kang, Xu Xie, Byeongdu Lee, Kyung Min Lee, Timothy J. White, Cecilia Leal, Nancy R. Sottos, Paul V. Braun, David G. Cahill, Proceedings of the National Academy of Sciences of the United States of America, ***in press*** (2019).

In Chapter 3, I showed a thermal conductivity switching contrast, $r \approx 1.5$, for magnetically aligned LCNs on a time scale of 10 min at above 150 ^{o}C. Studies of the kinetics and thermal transport properties of macromolecules suggest that the thermal conductivity switching ratio and decrease response time could be further enhanced by introducing light-responsive pendent groups−azobenzene−to polymer chains.

In Chapter 4, in collaboration with Jaeuk Sung in Sottos group, we designed and synthesized a photo-responsive azobenzene-based polymer (azopolymer) exhibiting an unprecedented reversible crystal-to-liquid transition driven by ultraviolet (UV) (375 nm) and green (530 nm) light-triggered modulation of interchain π-π interactions. Employing *in situ* TDTR and *in situ* synchrotron X-ray scattering, we report a reversible, light-triggered thermal conductivity switching of azopolymer between high (0.35 W m^{-1} K^{-1}) and low thermal conductivity (0.10 W m^{-1} K^{-1}) states. This three-fold change in the thermal conductivity is achieved by modulation of chain alignment resulted from the conformational transition between planar (*trans*) and non-planar (*cis*) azobenzene groups under ultraviolet (UV) and green light

illumination. This conformational transition leads to changes in the π-π stacking geometry and drives the crystal-to-liquid transition which is fully reversible and occurs on a time-scale of tens of seconds at room temperature.

To the best of knowledge, this is the first observation of a photo-triggered crystal-to-liquid transition in any polymeric material. This result demonstrates powerful control of the thermophysical properties of polymers by modulating interchain π-π networks by light. The fast (seconds), reversible crystal-to-liquid transition may also provide a new class of polymers engineered to switch physical, optical and thermal properties on demand, which may enable controlled molecular release, mechanical bonding, and reconfigurable thermal routing.

4.1 SYNTHESIS OF POLY[6-(4-(PHENYLDIAZENYL)PHENOXY)HEXYL METHACRYLATE] (AZOPOLYMER)

All materials were purchased from Sigma-Aldrich. 4-phenylazophenol (98%), methacrylol chloride (97%), 6-bromo-1-hexanol (97%) and cyanoisopropyl dithiobenzoate (CPDB) were used as received. 2,2'-azobisisobutyronitrile (AIBN, 98%) was recrystallized in chloroform before use. The synthesis steps of azopolymer are as follows.

6-(4-(phenyldiazenyl)phenoxy)hexan-1-ol

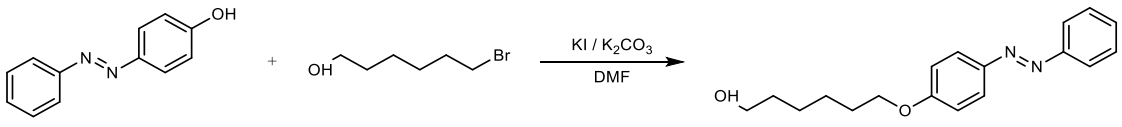

4-(phenyldiazenyl) phenol (3 g, 15 mmol) and 6-bromo-1-hexanol (5.48 g, 30 mmol) were dissolved in dimethylformamide (DMF) solution (25 mL) containing anhydrous potassium

carbonate (4.14 g, 30 mmol) and potassium iodide (15 mg, 0.9 mmol). The solution was refluxed at 90 ℃ under vigorous stirring for 24 h. The reacted mixture was then cooled to room temperature. After solvent evaporation, the concentrated solution was washed with water and extracted with chloroform. The extracted solution was dried over anhydrous $MgSO_4$. The remaining solvent was removed by evaporation. The 6-carbon spacer was chosen to optimize the trade-offs between the glass transition temperature and the mobility of the azobenzene functional group for conformational changes within the close-packed structure(*1*). The resulting crude product was recrystallized with ethanol, giving a dark brown solid. Yield: 75 %.

^{1}H NMR ($CDCl_3$, 400 MHz): δ (ppm) = 7.96-7.84 (dd, 4H, Ar-H), 7.54-7.38 (dt, 3H, Ar-H), 7.04-6.96 (m, 2H, Ar-H), 4.05 (t, 2H, O$\underline{CH_2}$), 3.72-3.59 (m, 2H, $\underline{CH_2}$OH), 1.90-1.78 (m, 2H, OCH$_2\underline{CH_2}$), 1.67-1.36 (m, 6H, OCH$_2$CH$_2\underline{CH_2}\underline{CH_2}\underline{CH_2}CH_2$OH).^{13}C{^{1}H} NMR (125 MHz, $CDCl_3$): δ (ppm) = 25.98, 26.10, 28.81, 29.35, 64.91, 68.38, 114.94, 115.00, 122.78, 122.78, 125.00, 125.53, 129.28, 129.28, 130.56, 147.32, 153.00, 161.86.

6-(4-(phenyldiazenyl)phenoxy)hexyl methacrylate

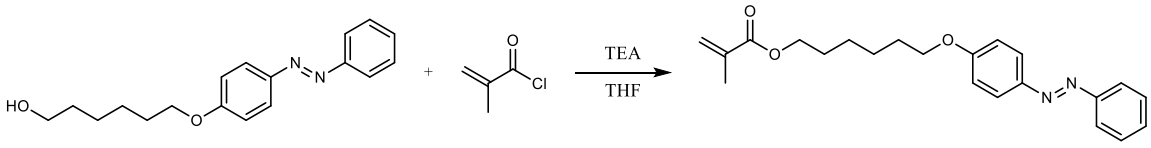

An anhydrous tetrahydrofuran (THF, 20 mL) solution containing 6-(4-(phenyldiazenyl)-phenoxy)hexan-1-ol (2 g, 6.7 mmol) and triethylamine (1.35 g, 13.4 mmol) was cooled to 0 ℃ in a water-ice bath. Then, methacryloyl chloride (1.4 g, 13.4 mmol) was added slowly dropwise. The solution was stirred in 0 ℃ for 30 minutes and at room temperature for 24 h. After constant stirring for another 24 h at room temperature, the solvent was evaporated, and chloroform was

added. The solution was then washed with aqueous NaCl and $NaHCO_3$ solutions, followed by drying with anhydrous $MgSO_4$. After solvent evaporation, the crude product was recrystallized from ethanol, giving an orange solid. Yield: 82 %.

^{1}H NMR ($CDCl_3$, 400 MHz): δ (ppm): 7.94-7.84 (dd, 4H, Ar-H), 7.53-7.40 (dt, 3H, Ar-H), 7.03-6.96 (d, 2H, Ar-H), 6.10 (s, 1H, C$\underline{CH_2}$), 5.55 (s, 1H, C$\underline{CH_2}$), 4.21-4.13 (t, 2H, OC$\underline{H_2}$), 4.08-4.02 (t, 2H, $\underline{CH_2}$O), 1.95 (s, 3H, CH_3), 1.89-1.79 (m, 2H, $OCH_2\underline{CH_2}$), 1.78-1.67 (m, 2H, $\underline{CH_2}CH_2O$), 1.60-1.39 (m, 4H, $OCH_2CH_2\underline{CH_2}\underline{CH_2}CH_2CH_2O$). ^{13}C {^{1}H} NMR (125 MHz, $CDCl_3$): δ (ppm) = 18.60, 26.00, 26.07, 28.82, 29.35, 64.89, 68.38, 114.93, 114.96, 122.78, 122.78, 124.23, 125.00, 129.27, 129.27, 130.56, 136.81, 147.18, 153.04, 161.84, 167.82.

Poly[6-(4-(phenyldiazenyl)phenoxy)hexyl methacrylate] (azopolymer)

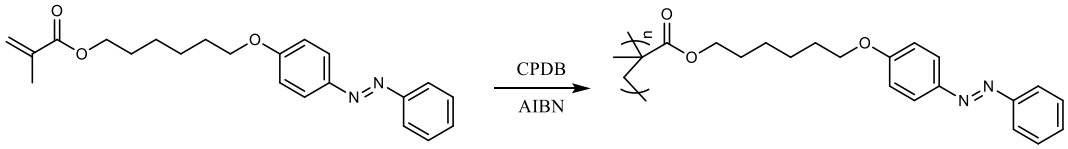

Azopolymer was prepared by reversible addition fragmentation chain-transfer (RAFT) polymerization. 6-(4-(phenyldiazenyl) phenoxy)hexyl methacrylate (2.17 g, 5.92 mmol), CPDB (6.7 mg, 0.064 mmol), and AIBN (1.3 mg, 0.012 mmol) were dissolved in anisole (6 mL). Then, the solution was treated with three freeze-pump-thaw cycles and sealed under N_2 gas. The polymerization system was placed in an oil bath at 70 ^oC℃ for 72 h. After polymerization, the polymer solution was added dropwise to cold methanol. The precipitate was dissolved in dichloromethane (DCM). The precipitate was recrystallized in cold methanol three times to remove unreacted monomers. The resulting azobenzene-functionalized polymer (poly[6-(4-(phenyldiazenyl)phenoxy)hexyl methacrylate])—hereafter referred to as "azopolymer"—was

collected and dried in a vacuum oven at 40 ° C for 24 h. Yield: 40%. M_w (GPC) = 2.40 × 10^4 g mol^{-1} and PDI = 1.37.

4.2 LIGHT-TRIGGERED PHASE TRANSITION OF AZOPOLYMER

We prepared ~280-nm thick, trans-azopolymer thin films by spin-coating 5 wt% azopolymer dissolved in a mixture of cyclopentanone and cyclohexane (9:1 weight ratio) on Al/polyimide/sapphire substrates. The substrates were first prepared by spin-coating a 250 nm polyimide film on a sapphire wafer followed by a 60 nm Al film deposition using magnetron sputtering. The purpose of the PI film is to reduce heat flow between the Al transducer and the sapphire substrate and thereby to increase the sensitivity of the TDTR measurements to the thermal conductivity of the azopolymer layer. The same specimens were used throughout the *in situ* optical microscopy, *in situ* TDTR, and *in situ* synchrotron X-ray scattering measurements.

Figure 4.1 shows the chemical structure of the synthesized azopolymer, as well as cross-polarized optical microscopy (POM) images of a spin-coated azopolymer film on Al/PI/sapphire and glass substrates, respectively, in the *trans* (Figure 4.1A, after green light exposure or time) and *cis* (Figure 4.1B, after UV exposure) states. The optical microscope images and videos were recorded using a VHX-5000 series Keyence Digital Microscope at 200× magnification. The phase transition of azopolymers was characterized under green (530 nm) and UV (375 nm) light illumination. We used collimated light emitting diodes (LEDs) with wavelengths of 530 nm and 375 nm for green and UV light sources, respectively (M530L3 and M375L3, Thorlabs) where we focused the light on a 0.16 cm^2 area throughout Chapter 4. The illuminated light intensity was controlled between 38 mW cm^{-2} and 630 mW cm^{-2} using a variable power controller LEDD1B (Thorlabs).

Starting from the crystalline ground state, UV light triggers a *trans*-to-*cis* photo-isomerization leading to melting of the polymer. Upon green light triggered reconversion of the *cis*-azobenzene groups to *trans*-azobenzene, the polymer returns to the crystalline state (at room temperature in the dark, the *cis* to *trans* isomerization will also take place over the course of several hours). The light-triggered melting and crystallization is a direct result of differences in the stacking of the planar *trans*- and non-planar *cis*-states of the azobenzene group. The planar trans-azobenzene readily undergoes π-π stacking, while the bent *cis*-azobenzene, in which the two phenyl rings align in different planes (*2*), does not (*3*).

As shown in the POM image (Figure 4.1C) the presence of spherulites indicates lamellar ordering of azopolymer film under ambient conditions. The spherulites in the crystalline *trans*-azopolymer film disappear upon exposure to UV light, resulting in an isotropic liquid, which turns dark in the POM image (Figure 4.1D). OM images in Figure 4.2 show a gradual melting of azopolymer during *trans*-to-*cis* photoisomerization and formation of spherulites during *cis*-to-*trans* photoisomerization. Under UV and green light illumination conditions, the melting and crystallization are complete within 10 s for azopolymer films. The reversible crystal-to-liquid transition can take place for azobenzene powder, too. Figure 4.3 shows reversible transition from solid powder to liquid on the glass substrate under UV and green light illumination. The transition time for azopolymer powders is slightly higher than the thin films due to the light penetration depth. Hereafter, we refer to the crystalline and liquid states of azopolymer as *trans*- and *cis*-azopolymer, respectively.

4.3 PHYSICAL PROPERTY CHANGES OF AZOPOLYMER DURING *TRANS-CIS* PHOTOISOMERIZATION

UV-Vis spectroscopy and differential scanning calorimetry (DSC) measurements were carried out to confirm the *trans-cis* photoisomerization. First, DSC was performed to study the phase transition temperature of the azopolymer with *trans* and *cis* conformational states of the attached azobenzene groups. The DSC measurements were performed using a TA Instrument Q20 Differential Scanning Calorimeter equipped with a Liquid Nitrogen Cooling System (LNCS). Tzero aluminum pan and lid were used as sample containers. Al_2O_3 was used as a reference material for calculating the specific heat of azopolymers. Dry nitrogen was used as a sample purge gas. The heating and cooling rates were 10 $^oC\ min^{-1}$. We determined the glass transition temperature (T_g), melting temperature (T_m) and crystallization temperature (T_c) of the *trans*- and *cis*-azopolymers from the inflection points in the DSC data.

We observed an appearance of a glass transition temperature ($T_{g,cis}$) at −48 ^oC after exposure to UV light which disappears upon exposure to green light. This transition temperature is markedly lower than the temperature of a small endothermic inflection in the DSC data at 31 ^oC, which we interpret as T_g of residual amorphous *trans*-azopolymer. (The *trans*-azopolymer melting point is 80 ^oC.) Previous studies of polymers with similar azobenzene side-chain structures in *trans* states (*4-6*). have reported glass transition temperatures in the range of $35 < T_g < 80\ ^oC$. Similar large shifts in T_g as a function of isomer-state have been previously observed in polybutadiene ($\Delta T_g \sim 90\ ^oC$) (*7*), and azobenzene functionalized polymers ($\Delta T_g \sim 60\ ^oC$) (*8*). Figure 4.4 shows 1st and 2nd heating and cooling DSC curves for *trans*-azopolymer between −80 and 110 °C. There is evidence of a small amount of amorphous phase after green light exposure

as a weak inflection point at 31 °C, see the inset of Figure 4.4A. This inflection point is thought to be the glass transition of the remaining amorphous phase. An endothermal peak at 80 °C appears which corresponds to melting of *trans*-azopolymer. The *cis*-azopolymer thermally relaxes via *cis*-to-*trans* transition near the melting temperature. Figure 4.5A shows an exothermal peak at 88 °C, followed by melting at 80 °C. The *cis*-to-*trans* transition overlaps with the melting of *trans*-azopolymer. After the *cis*-to-*trans* thermal relaxation, DSC curves for *cis*-azopolymer become identical to the *trans*-azopolymer as shown in Figure 4.4B. The glass transition of *cis*-azopolymer shown in the magnified heating DSC curve in Figure 4.5C disappears in the cooling curve. T_g of *cis*-azopolymer was further verified by subjecting *cis*-azopolymer to multiple cycles between −80 °C and −10 °C. Figure 4.5D shows 1st and 2nd heating and cooling DSC curves, indicating consistent glass transition at –48 °C. Because of its completely amorphous nature, the *cis*-azopolymer does not exhibit a sharp melting point, but rather softens over a temperature range around T_g to a viscoelastic liquid. DSC data was used to calculate the specific heat of *trans*- and *cis*-azopolymer (Figure 4.6). The thermal conductivity throughout this chapter is calculated using the relationship $\Lambda = e^2 / C$ where e is the thermal effusivity of azopolymer measured by TDTR and C is determined by the density and the specific heat of *trans*- and *cis*-azopolymers.

The crystal-to-liquid transition of azopolymer takes advantage of a large change in the difference in the phase transition temperature between *trans*- and *cis*-azopolymers ($T_{g,cis}$, $T_{m,trans}$). At room temperature, *cis*-azopolymer is stable in the fluid state, $T_{g,cis}$ < 300 K, and *trans*-azopolymer is stable in the crystalline state, $T_{m,trans}$ > 300 K. The data presented in Chapter 4 results from azopolymer with a molar mass M_w = 24,000 g mol^{-1}; for this molar mass, $T_{g,cis}$ = −48 °C and $T_{m,trans}$ = 80 °C. We expect that the temperature window for the crystal-liquid

transition, $T_{g,cis} < T < T_{m,trans}$, can be tuned by varying the molar mass. An increase in molar mass would lead to an increase in $T_{g,cis}$ as predicted in the Flory-Fox equation, eventually leading to a crystal-glass transition at room temperature. A crystal-glass transition would be preferred over a crystal-liquid transition in applications in which materials need to retain their shape and mechanical properties.

Gel permeation chromatography (GPC) was performed to measure molecular weights and molecular weight distributions relative to linear polystyrene standards using a Waters 1515 Isocratic HPLC module equipped with a Waters (2998) Photodiode Array Detector, a Waters (2414) Refractive Index Detector, a Waters (2707) 48 well autosampler and a series of 4 Waters HR Styragel columns (7.8 X 300 mm, HR1, HR3, HR4, and HR5) in HPLC grade THF at 30 °C at a flow rate of 1 mL min^{-1}. Standard polystyrenes from Shodex with M_n of 1.2 KDa, 3 KDa, 9 KDa, 28 KDa, 65 KDa, 152 KDa, 419 KDa, 979 KDa, 2,233 KDa, and 2,906 KDa with PDI of 1.09, 1.04, 1.03, 1.03, 1.03, 1.03, 1.04, 1.05, 1.04, and 1.04 were used as reference for molecular weight determination. The molecular weight of the azopolymer was calibrated using the following equation.

$$\log M_w = 1.445596e^{-2} - 3.66e^{1}t + 2.53t^2 - 8.77e^{-2}t^3 + 1.52e^{-3}t^4 - 1.05e^{-5}t^5 \qquad (4.1)$$

where t is the retention time and M_w is the relative molecular weight of the polymer. Fig. S6a shows a GPC trace of the azopolymer.

UV-Vis spectroscopy was performed to confirm the *trans-cis* photoisomerization of the azopolymer using a model UV-2450 UV-VIS Spectrophotometer, Shimadzu Corp. We used a 280-nm thick spin-coated azopolymer film on a sapphire substrate and illuminated the

azopolymer sample with UV light with varying intensity of 38, 80, 180, 320 and 630 mW cm^{-2} for 15 and 30 s. Figure 4.7B shows the absorption spectra of azopolymer film which is gradually shifted due to *trans*-to-*cis* photoisomerization under UV light. We attribute the spectral changes at wavelengths near 360 nm to the $\pi \rightarrow \pi^*$ electronic transitions and the changes at wavelengths near 450 nm to the $n \rightarrow \pi^*$ electronic transitions of the azobenzene functional groups (*9*).

Transverse (v_t) and longitudinal (v_l) speed of sounds of *trans*-azopolymer were measured by picosecond acoustic and surface acoustic wave measurements for crystalline azopolymer, and picosecond interferometry for liquid azopolymer using a TDTR setup (*10*, *11*). v_l was calculated from the acoustic echoes from Al/azopolymer film interphase using the relationship $v_l = 2\ h/\Delta t$, where h is the thickness of the azopolymer film and Δt is the time between echoes. v_t was calculated by generating and measuring surface acoustic waves using a periodic elastomeric PDMS mask on *trans*-azopolymer film. The longitudinal (C_{11}) and transverse (C_{44}) elastic moduli were calculated as $C_{11} = \rho v_l^2$ and $C_{44} = \rho v_t^2$. v_l of the liquid state azopolymer was calculated by measuring reflected probe beam intensity of a SiO_2/*cis*-azopolymer (1 mm)/Pt (60 nm)/SiO_2 liquid cell under continuous UV light illumination (630 mW cm^{-2}) where $v_l = v_p/(2\lambda n_l)$ and v_p is the in-phase TDTR probe beam oscillation frequency, λ is the wavelength of light and n_l is the refractive index of liquid measured by Woollam VAS Ellipsometer (n_l= 1.64 at λ = 780 nm). All measured physical parameters, including the molecular weight, the poly-dispersity indices (PDI), heat capacity per unit volume (C), T_g, T_m, and longitudinal and transverse speed of sounds (v_l and v_t) and elastic moduli (C_{11} and C_{44}) for *trans*- and *cis*-azopolymers, are summarized in Table 4.1.

4.4 THERMAL CONDUCTIVITY SWITCHING IN AZOPOLYMER

Across the crystal-to-liquid transition, the most significant property change observed, other than the crystal-liquid transition, is a three-fold change in the thermal conductivity in a matter of seconds at room temperature. I measured the dependence of out-of-plane thermal conductivity of the azopolymer film on Al (60 nm)/polyimide (250 nm)/sapphire substrates on exposure to UV and green light using *in situ* TDTR measurements (*12-14*). The $1/e^2$ intensity radius was 10 μm, and the intensities of the pump and probe beam were 5 mW and 3 mW, respectively. The steady state temperature rise, ΔT_{SS}, of the probed region was ≈10 K. The thermal penetration depths were 55–75 nm at 11 MHz and 180–240 nm at 1.12 MHz. At f = 11 MHz, the bidirectional heat flow model is sensitive to the thermal effusivity, $e = \sqrt{\Lambda C}$, where C is independently determined by combining measurements of a 280-nm thick azopolymer film using modulation frequencies of 10.1 and 1.12 MHz at room temperature and the density and the specific heat of *trans*- and *cis*-azopolymers under UV and green light illumination in Figure 4.6 (*15*). To measure changes in thermal conductivity during the crystal-to-liquid phase transition, I fixed the delay time at 100 ps and continuously measured V_{in} and V_{out} under UV and green light illumination.

Figures 4.8A-B shows a schematic illustration for the experimental configuration of *in situ* TDTR measurements for azopolymer/Al/PI/sapphire samples under green and UV light illumination. Figure 4.8C shows measured and fitted TDTR curves for *trans*- and *cis*-azopolymer films after green and UV light illumination. The thermal conductivity reversibly switches between 0.35 ± 0.05 W m^{-1} K^{-1} in *trans*-azopolymer to 0.10 ± 0.02 W m^{-1} K^{-1} in *cis*-azopolymer. These values are within the values expected for polymers: for example, the thermal

conductivity of polyethylene varies from 0.1 W m^{-1} K^{-1}, when randomly oriented to 90 W m^{-1} K^{-1} along the draw direction of a highly oriented crystalline fiber (*16, 17*).

Figure 4.9A shows temperature-dependent thermal conductivity of *trans*- and *cis*-azopolymers. The temperature-dependent thermal conductivities of *trans*- and *cis*-azopolymers were measured using a temperature controlled INSTEC HOT/COLD stage having an optical window with the heating and cooling rates of 10 ^{o}C min^{-1} under continuous green and UV light illuminations (630 mW cm^{-2}). Figure 4.9B shows the thermal conductivity of the azopolymer under alternating UV and green light illumination. 90% of the change in thermal conductivity occurs within a few tens of seconds when the light intensity is 320 mW cm^{-2}. The partial loss of thermal conductivity is attributed to incomplete crystallization due to insufficient time of illumination and the steady-state temperature rise during *in situ* TDTR measurements. The rate of thermal conductivity switching, τ_0^{-1}, which is the rate to achieve 90% of the total thermal conductivity change, increases from 0.016 to 0.126 s^{-1} as the UV light intensity increases from 38 to 630 mW cm^{-2} (Figure 4.10).

The thermal conductivity of *cis*-azopolymer is lower than the conductivity of the polyimide thermal blocking layer (0.2 W m^{-1} K^{-1}). Therefore, a majority of the heat deposited by the pump beam flows to the substrate side. Thus, the sensitivity of the measurement to the thermal conductivity of *cis*-azopolymer is smaller than the sensitivity to the thermal conductivity of *trans*-azopolymer. Therefore, I performed an independent experiment using frequency-domain probe beam deflection (FD-PBD) to verify the thermal conductivity of the liquid state (*18*). The detail of FD-PBD is described in Chapter 2.4. I used a 1-mm thick of azopolymer liquid sandwiched by a 60 nm Pt-coated fused silica substrate and a glass cover slide. Figure 4.11A

shows the measured and fitted FD-PBD curves for the liquid azopolymer on a Pt (60 nm)/SiO_2 sample under 630 mW cm^{-2} UV illumination at 60 °C. The pump beam heated the sample from the liquid side while measuring the probe beam deflection at r_0 = 10 μm. Figure 4.11B shows the in-phase and out-of-phase $\Delta\theta$ at a fixed f = 500 Hz with varying r_0 from −20 μm to 20 μm. The probe beam deflection becomes zero when the pump and the probe beams overlap. I fixed C = 1.85 J cm^{-3} K^{-1} and fitted the FD-PBD curve using Λ as a free parameter. The fitted value for the Λ of liquid state azopolymer is 0.12 W m^{-1} K^{-1}, which is consistent with the thermal conductivity of the liquid state azopolymer measured by TDTR.

4.5 THE EFFECT OF CHAIN ALIGNMENT ON THERMAL CONDUCTIVITY

Amorphous *trans*-azopolymer film was prepared by LN_2 quenching the *trans*-azopolymer film from the melting temperature. The measured and fitted TDTR data for amorphous azopolymer film is shown in Figure 4.12A. The thermal conductivity of the amorphous azopolymer is $\Lambda_{amorphous}$ = 0.19 ± 0.02 W $m^{-1}K^{-1}$ at room temperature, which is similar to other amorphous polymers with similar transverse (v_t) and longitudinal (v_l) sound velocities and atomic densities (*15*). Figure 4.12B shows thermal conductivity of amorphous film from −75 to 130 °C. The thermal conductivity of amorphous azopolymer slightly decreases with decreasing temperature. Above the melting temperature, the thermal conductivity of amorphous azopolymer becomes closer to that of the liquid state azopolymer.

While C can have a significant impact on the thermal conductivity, we observed that C is only ≈ 10 % greater in the amorphous state than the crystalline state yet the crystalline *trans*-azopolymer exhibits an 80% higher thermal conductivity than the amorphous *trans*-azopolymer, suggesting that crystallinity plays the dominant role in the change in thermal conductivity. The

higher thermal conductivity of crystalline *trans*-azopolymer can be attributed to the stronger dispersion and longer lifetimes of vibrational modes created by the out-of-plane alignment of side chains with planar azobenzene groups. Due to the limitations in the experiments associated with a very low sensitivity of the TDTR signals to in-plane thermal conductivity, the experimental data are limited to the out-of-plane thermal conductivity of azopolymer films. Nevertheless, we expect that the in-plane thermal conductivity of azopolymer film is lower than the out-of-plane thermal conductivity since the direction of thermal conduction is normal to the aligned side chains where most of heat would be carried by interchain interaction across the side-chain networks.

4.6 INTERCHAIN π-π BONDING TRANSITION BY LIGHT

Polymer films with azobenzene side-chain groups often form smectic or lamellar structures with an out-of-plane azobenzene group arrangement (*19, 20*), exhibiting characteristic side-chain interdigitation due to the π-π stacking of azobenzene groups (*1*). Upon UV light illumination, these interchain π-π interactions decrease dramatically with the torsional rotation of the azobenzene groups (*3*). Figure 4.13 illustrates a possible mechanism for crystal-to-liquid transition, associated with disruption of the π-π stacked azobenzene groups in azopolymer during the *trans*-to-*cis* isomerization. Upon UV excitation, the *trans*-azobenzene groups transform to non-planar *cis*-azobenzene isomers with various (C-N=N-C) dihedral angles between the two phenyl rings. This torsional rotation of the azobenzene groups causes a steric hindrance for azobenzene π-π stacking (*2*). As the population of the *cis*-isomer grows, the azobenzene stacking decreases, and long-range crystalline order is lost (*3*). Upon exposure to the green light (*cis*-to-*trans* transition), crystalline order is recovered by stacking of the *trans*-azobenzene groups.

In collaboration with Minjee Kang in Leal group at Illinois, we performed *in situ* synchrotron grazing-incidence wide-angle X-ray scattering (GIWAXS), wide-angle X-ray scattering (WAXS), grazing-incidence small-angle X-ray scattering (GISAXS) and small-angle X-ray scattering (SAXS) measurements to test this hypothesis and study the temporal evolution of short- and long-range macromolecular structure created by UV and green light illumination. We brought the azopolymer/Al/PI/sapphire samples to the 12-ID-B and 12-ID-C beamlines at the Advanced Photon Source at the Argonne National Laboratory for *in situ* synchrotron X-ray scattering measurements. Samples were probed using 13.3 keV (12-ID-B) and 18 keV (12-ID-C) X-rays. The samples were placed on a temperature-controlled stage at a temperature of 25–30 ^{o}C. The UV and green LEDs were mounted 15 cm above the sample stage. The LEDs were remotely controlled during X-ray scattering measurements. The data collection time of the detector was set at 0.5 s for the GISAXS, SAXS and GIWAXS experiments, and 1 s for the WAXS experiments. The time intervals between each data collection were 1 s and 3 s for the SAXS and WAXS measurements, respectively.

Figure 4.14 shows *in situ* 2-D GIWAXS patterns of the azopolymer/Al/PI/sapphire substrate during *trans*-to-*cis* and subsequent *cis*-to-*trans* transitions under UV and green light (630 mW cm^{-2}). Two sets of diffraction rings can be observed for the *trans*-azopolymer film (upper left panel). One corresponds to in-plane diffraction associated with the lateral side-chain interdigitation of azobenzene π-π stacking ($d_{\pi\text{-}\pi}$) at q = 1.68–1.78 Å^{-1}. The second arises from out-of-plane diffraction at integral multiples of q_z = 0.233 Å^{-1} consistent with a 2.7 nm (001) lamellar spacing of the azopolymers. The diffraction changes associated with $d_{\pi\text{-}\pi}$ and lamellar spacing represent macromolecular ordering of the azopolymer at different length scales. UV light illumination triggers order-disorder transition from the crystalline phase to isotropic phase where

We observed the loss of crystalline diffraction peaks, leaving a diffuse ring (as indicated by a violet arrow). Under green light illuminations We observed evolution of GIWAXS pattern almost identical to the initial pattern (as indicated by a green arrow), suggesting full recovery of lamellar structure on a time scale of ~10 s.

Transmission WAXS experiments were also performed to generate time-dependent diffraction peak intensity profiles Figures 4.15-16 show *in situ* transmission 2-D WAXS images of azopolymer during *trans*-to-*cis* and subsequent *cis*-to-*trans* transitions under UV and green light illuminations, respectively (630 mW cm^{-2}). We first collected sets of azimuth integrated intensity profiles during microstructural evolution. Then, the sets of azimuth integrated intensity profile were presented as a 2-D the time-dependent, azimuth-integrated WAXS signal intensity in a defined q scale in Figure 4.17A. Under UV light illumination, the $d_{\pi\text{-}\pi}$ peak gradually broadens and shifts to lower q while the unit cell lattice (010) reflection remains at q = 1.22 $Å^{-1}$. After ~20 s of UV illumination, the $d_{\pi\text{-}\pi}$ peak fades, followed by damping of the (010) peak, leaving only a broad diffuse scattering ring. Figure 4.17B shows $d_{\pi\text{-}\pi}$ spacing and the $d_{\pi\text{-}\pi}$ peak full-width-at-half-maximum (FWHM) during the *trans*-to-*cis* photoisomerization. Subsequent green light illumination triggers a *cis*-to-*trans* transition in which all diffraction patterns reappear, indicating recovery of the interdigitated structure. The time-scale of the phase transition corresponds to the time-scale of the thermal conductivity switching observed in TDTR measurements in Chapter 4.4.

4.7 LONG-RANGE ORDER-DISORDER TRANSITIONS

In addition to the short-range order-disorder transition of side-chain azobenzene groups revealed by the WAXS measurements, we performed GISAXS and transmission SAXS to study the long-

range order-disorder transition of the azopolymer backbone under UV and green light illumination. Figure 4.18 shows a 2-D GISAXS diffraction pattern of a *trans*-azopolymer film. We observed integral multiples of $q_z = 0.233$ Å^{-1} and $q_z = 0.224$ Å^{-1} consistent with a double periodic array at short $(001)_s$ and long $(001)_l$ spacings for *trans*-azopolymer lamellae.

Figures 4.19-20 show *in situ* transmission 2-D SAXS images of azopolymer during *trans*-to-*cis* and subsequent *cis*-to-*trans* transitions under UV and green light illuminations (630 mW cm^{-2}), respectively. Each SAXS data was converted to azimuth integrated intensity as presented in 2-D the time-dependent, azimuth-integrated SAXS intensity plot in Figure 4.21 during *trans*-to-*cis* and *cis*-to-*trans* transitions. The interdigitated (001) and (002) peaks decay under UV illumination in approximately 10 s. Crystallization into the lamellar structure occurs under subsequent green light illumination on a comparable time-scale. Prior to formation of the final lamellar structure, we observed a transient diffraction peak at $q = 0.189$ Å^{-1}, which can be attributed to an intermediate phase (IP) consisting of a weakly ordered structure ($d = 3.3$ nm) that does not give rise to higher order peaks. The diffraction peak of this intermediate phase decays rapidly as the fully interdigitated $(001)_s$ and partially interdigitated $(001)_l$ peaks grow in the time-dependent intensity profile in Figure 4.22.

The transient nature of the IP prior to the formation of the lamellar structure supports a crystallization pathway which passes through a weakly ordered phase. We speculate that in this intermediate state side-chains form a non-interdigitated structure during the *cis*-to-*trans* isomerization before forming the interdigitated structure. After the azopolymer chains are interdigitated at the nucleation site, they exhibit outward growth of the spherulite structure (see

Chapter 4.2). Figure 4.23 shows a schematic illustration of the assembly and crystallization process outlined in Chapter 4.7.

4.8 SIDE-CHAIN INTERDIGITATION OF *TRANS*-AZOPOLYMER

The intensity of the $(001)_s$ peak is an order of magnitude higher than the $(001)_l$ peak, suggesting that $(001)_s$ is the most dominant structure. This split peak can be attributed to the two distinct populations of lamellar spacings originating from slightly different azobenzene interdigitation configurations (*1, 21*). In Chapter 4.7, We observed that *trans*-azopolymer exhibits two independent packing structures with fully and partially interdigitated azobenzene side-chains. We suspect that the partially interdigitated lamellar $(001)_l$ exhibit weak π-π interaction compared with the fully interdigitated lamellar $(001)_s$ structure, thereby losing ordering much faster than the fully interdigitated lamellar under UV light illumination. We used a low-intensity UV light illumination to trigger a selective *trans*-to-*cis* transition of partially interdigitated *trans*-azopolymer lamellar and measured *in situ* SAXS pattern changes (Figure 4.24). We plot a 2-D time-dependent azimuth integrated SAXS intensity plot and time-dependent SAXS intensity profile in Figure 4.25. The $(001)_l$ peak intensity decays under low-intensity UV illumination while (001)s peak intensity remains almost the same.

4.9 SUMMARY

In summary, we observed reversible crystal-liquid transitions in an azopolymer which occur on the order of 10 s with a UV and green light under illumination intensities on the order of 100 mW cm^{-2}. This transition is associated with a three-fold change in thermal conductivity. UV light illumination induces a transition in the azobenzene side chains from the planar *trans*-state to the

non-planar *cis*-state; green light illumination reverses this transition. The torsional rotation of the phenyl rings in *cis*-azobenzene disrupts π-π interactions between the azobenzene groups, resulting in formation of an isotropic liquid with a thermal conductivity of 0.10 W m^{-1} K^{-1}. Subsequent green light illumination induces crystallization of *trans*-azopolymer, which is found to have a thermal conductivity of 0.35 W m^{-1} K^{-1} and consists of crystals containing interdigitated aligned planar-azobenzene side chains. Excitingly, we find that the conformational state of specific functional groups on polymer chains not only regulates short- and long-range ordering, but also the thermal transport properties of the polymer.

4.10 FIGURES AND TABLE

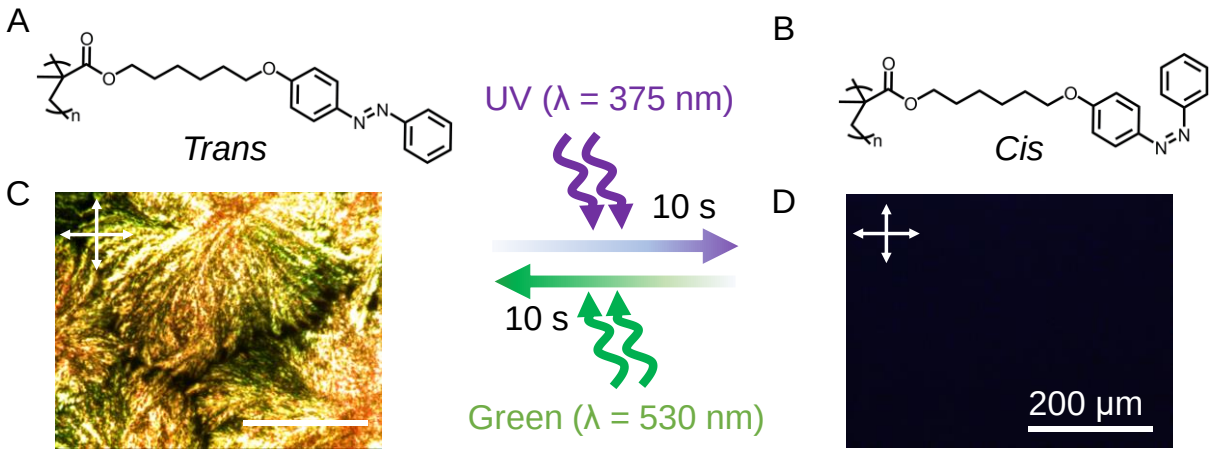

Figure 4.1. Light-triggered phase transition of azopolymer. **A.** *Trans*- and **B.** *cis*-azopolymer structures. Corresponding cross-polarized optical microscopy images of **C.** *trans*- and **D.** *cis*-azopolymer films on the glass substrate under continuous UV and green light illuminations. All scale bars are 200 μm.

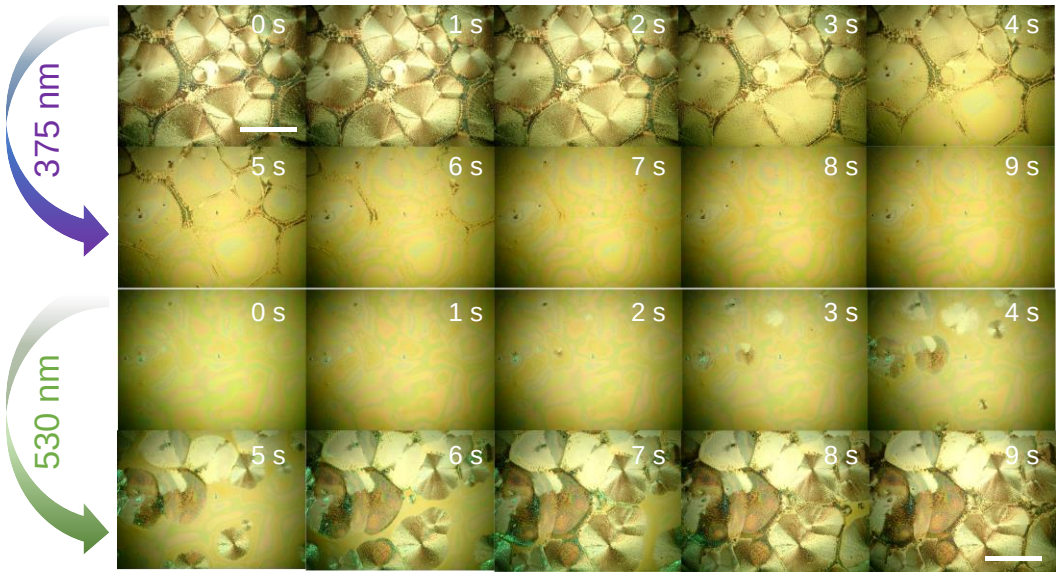

Figure 4.2. Optical microscopy images of a spin-coated azopolymer film on the Al/polyimide/sapphire substrate during reversible crystal-to-liquid transitions under UV and green light illumination. The light intensity is 630 mW cm^{-2}. The time interval between each image is 1 s. The scale bar is 200 μm.

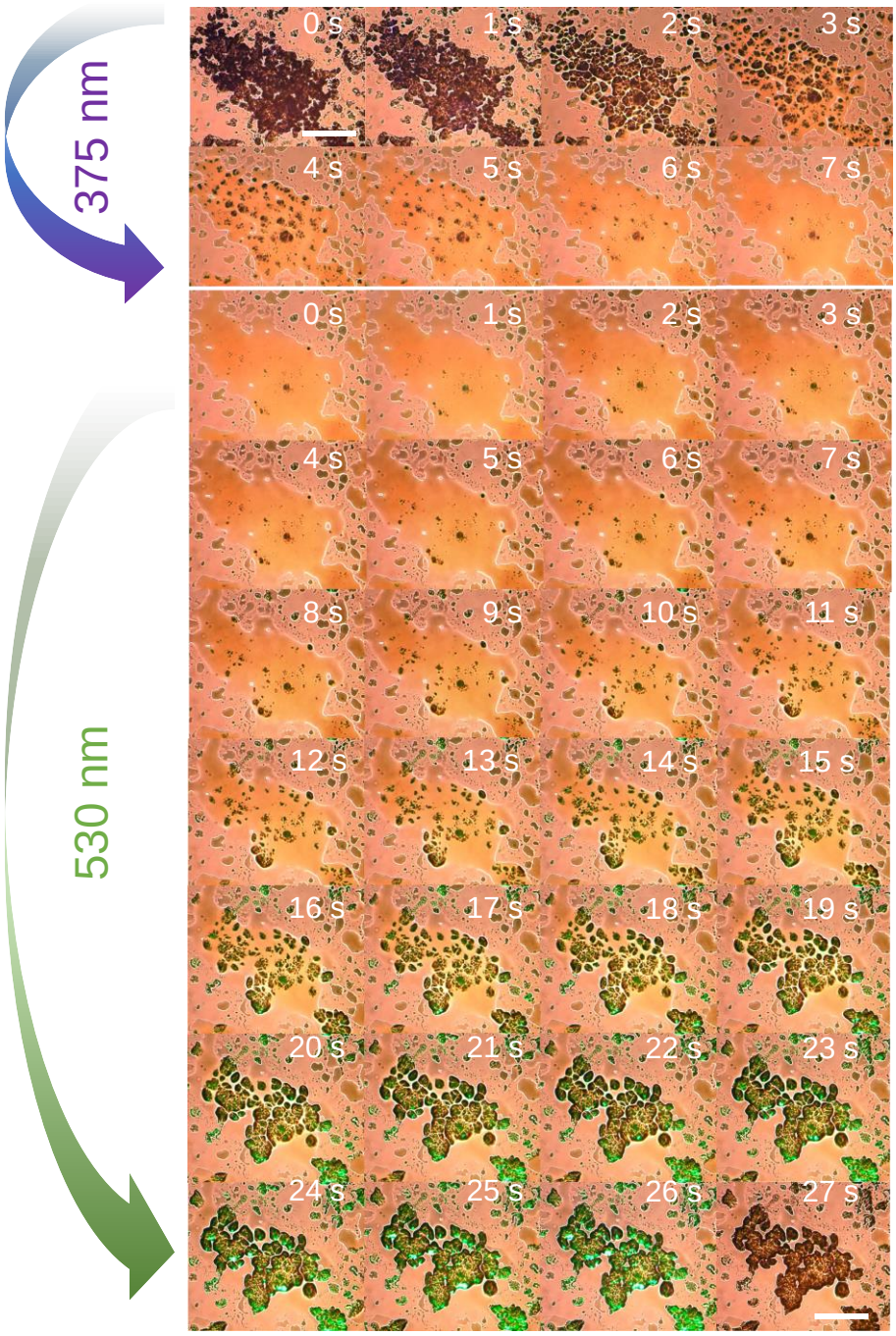

Figure 4.3. Transmission optical microscopy images of azopolymer powders on the glass slide during reversible crystal-to-liquid transitions under UV and green light illumination (630 mW cm^{-2}). The scale bar is 200 μm. The time interval between each image is 1 s.

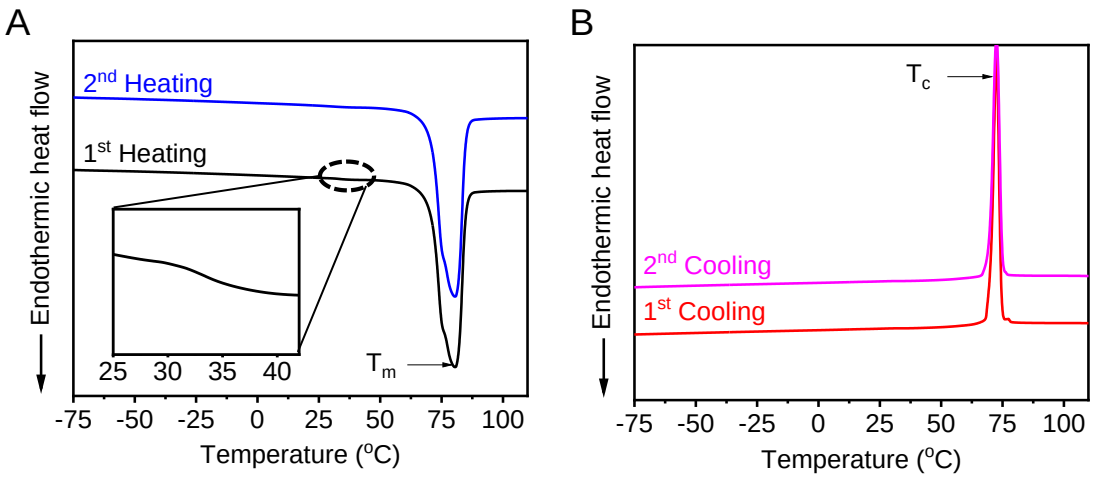

Figure 4.4. Phase transition temperatures of *trans*-azopolymer. **A.** 1st and 2nd heating DSC curves for *trans*-azopolymer. The inset shows a magnified heating curve with an inflection point. **B.** 1st and 2nd cooling DSC curves for *trans*-azopolymer.

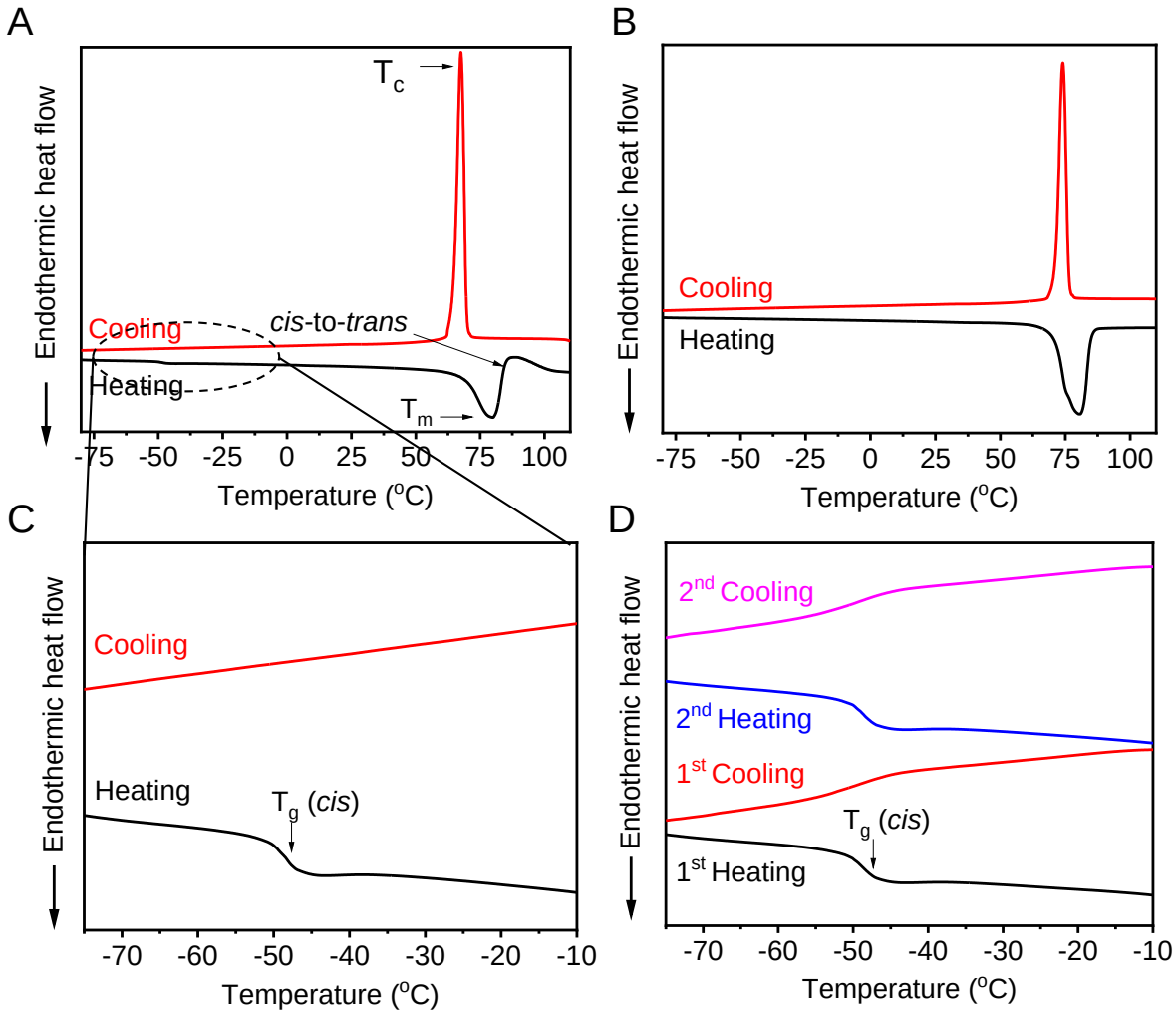

Figure 4.5. Phase transition temperatures of *cis*-azopolymers. **A.** 1st heating and cooling DSC curves for *cis*-azopolymer from −80 °C to 110 °C. **B.** 2nd heating and cooling DSC curves for *cis*-azopolymer immediately following the 1st DSC cycle shown in panel A. **C.** Expanded 1st heating and cooling DSC curves for *cis*-azopolymer. **D.** 1st and 2nd heating and cooling DSC curves for *cis*-azopolymer with a reduced temperature window from −80 °C to −10 °C.

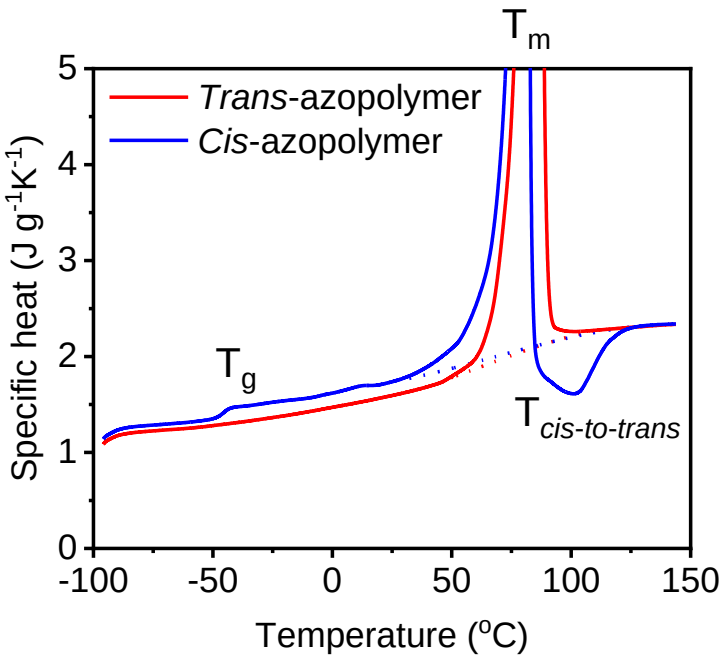

Figure 4.6. Specific heat of *trans*- and *cis*-azopolymers from –100 °C to 150 °C. The dotted lines under the endothermic melting peak represent the estimated specific heat values used to determine the thermal conductivity of *trans*- and *cis*-azopolymers at around the melting temperature.

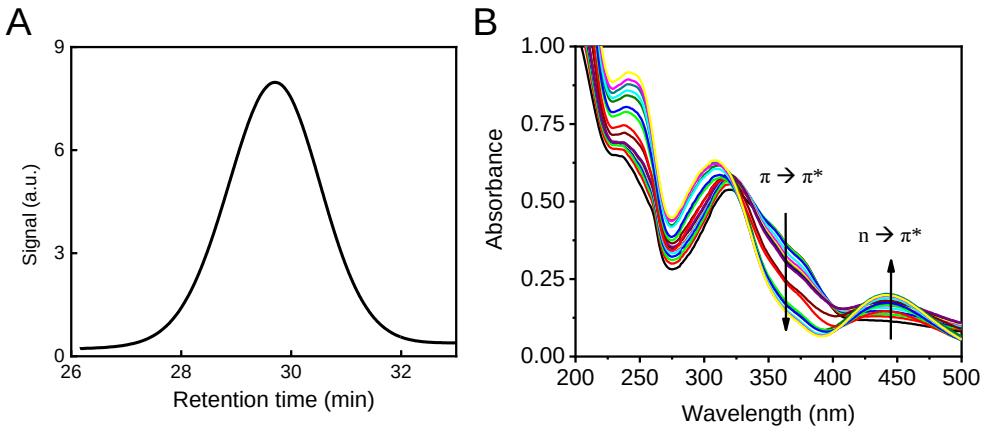

Figure. 4.7. Molecular weight distribution and optical properties of azopolymer. **A.** GPC trace of the synthesized azopolymer. **B.** UV-Vis absorption spectrum shift for an azopolymer film under UV illumination.

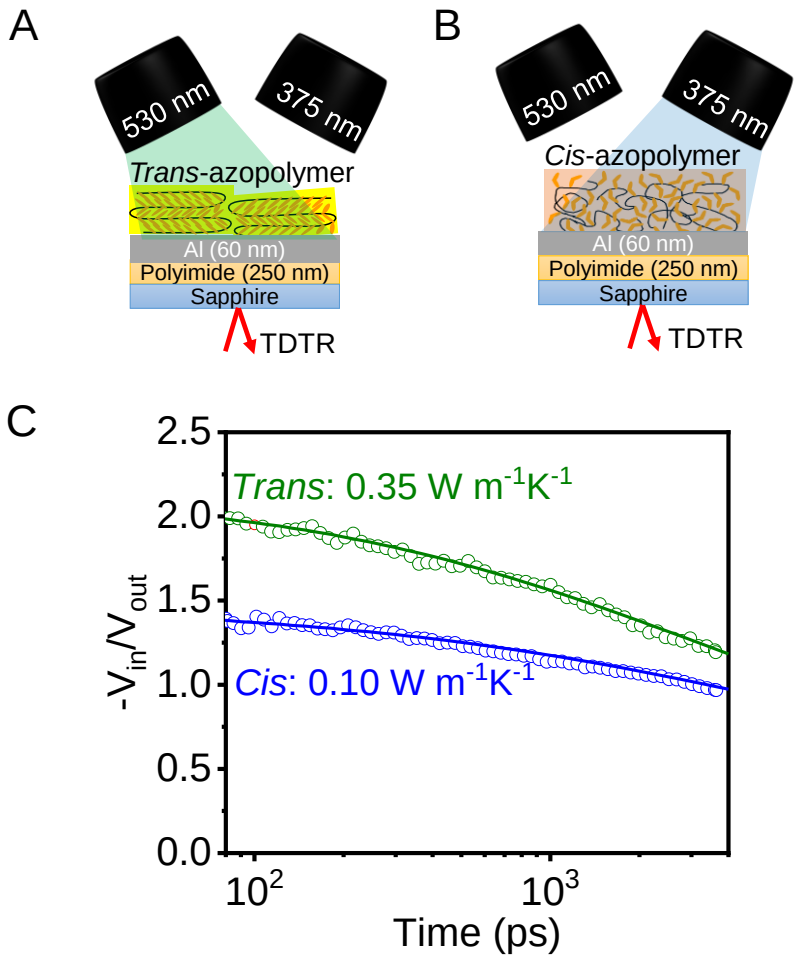

Figure 4.8. Thermal conductivity switching of azopolymer. **A.** Schematic illustration for *in situ* TDTR measurements for an azopolymer film under green and UV light illumination. **B.** Measured and fitted TDTR data for *trans*- and *cis*-azopolymer films after green and UV light illumination, respectively.

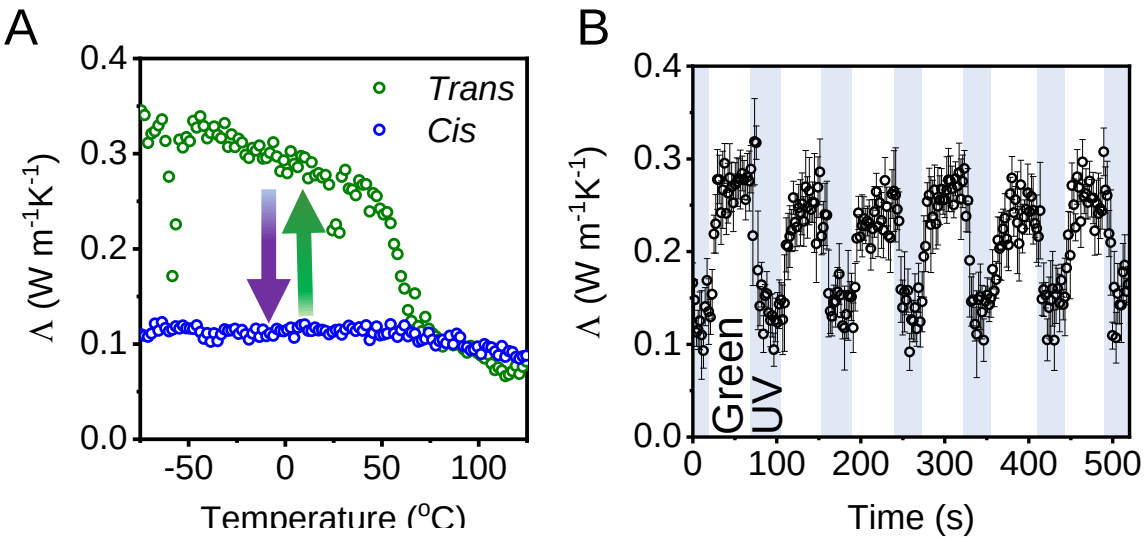

Figure 4.9 Thermal conductivity switching of azopolymer. **A.** Temperature-dependent thermal conductivity of *trans*- and *cis*-azopolymer films. **B.** Thermal conductivity of the azopolymer film under alternating green and UV light illumination. The reversible *trans*-to-*cis* transitions between the crystalline and liquid states occur within 10 s under UV and green light illumination (320 mW cm^{-2}) at room temperature. Error bars represents temporal signal fluctuations and experimental uncertainty.

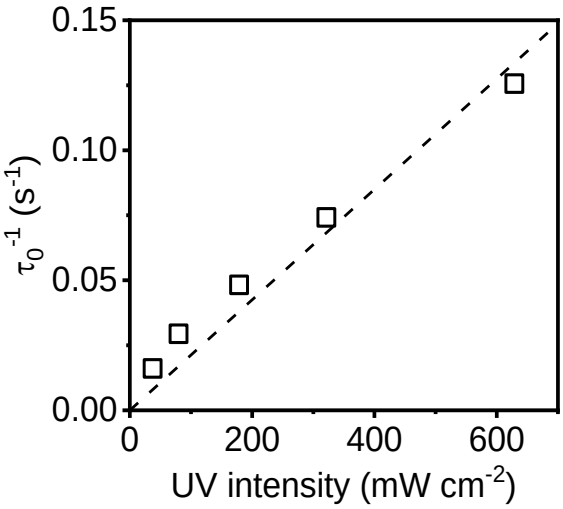

Figure 4.10. Thermal conductivity switching rate τ_0^{-1} of azopolymer film with increasing UV intensity.

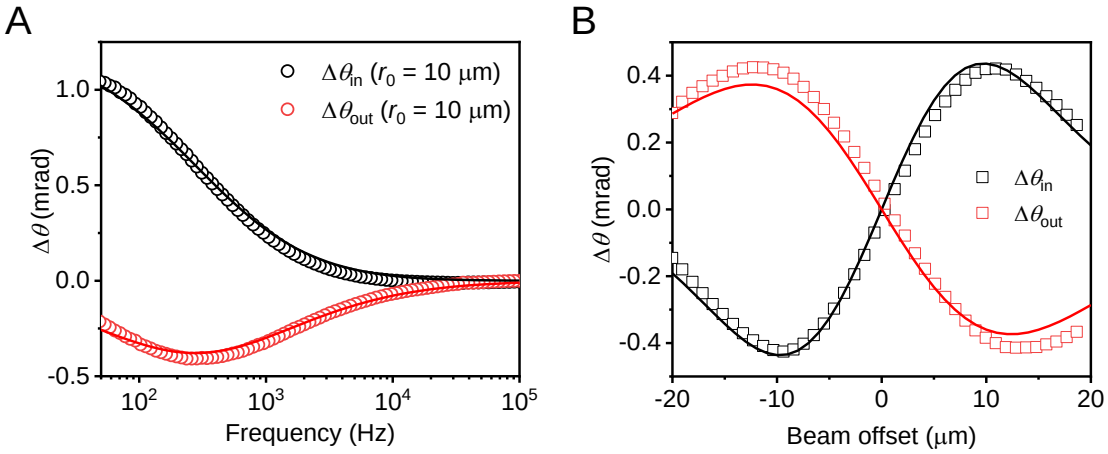

Figure 4.11. Thermal conductivity of cis-azopolymer measured by FD-PBD. **A.** Measured and fitted FD-PBD curves for the liquid state azopolymer at r_0 = 10 μm. **B.** Measured and fitted FD-PBD data with varying r_0 from −20 μm to 20 μm at f = 500 Hz.

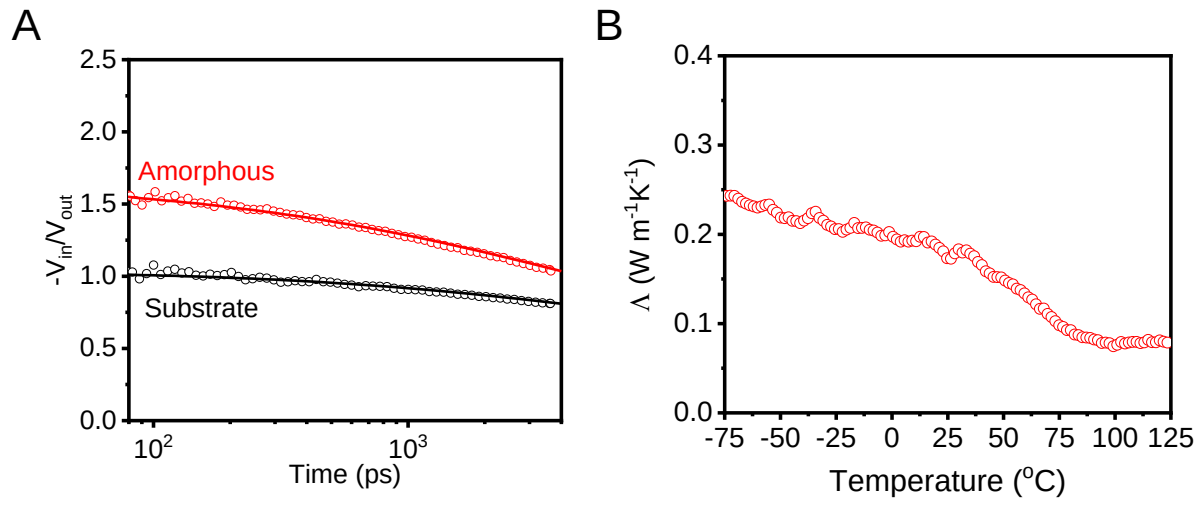

Figure 4.12. Thermal conductivity of amorphous *trans*-azopolymer. **A.** Measured and fitted TDTR curves for the amorphous *trans*-azopolymer film and the Al/polyimide/sapphire substrate. **B.** Temperature-dependent thermal conductivity of amorphous *trans*-azopolymer film from −75 ºC to 130 ºC.

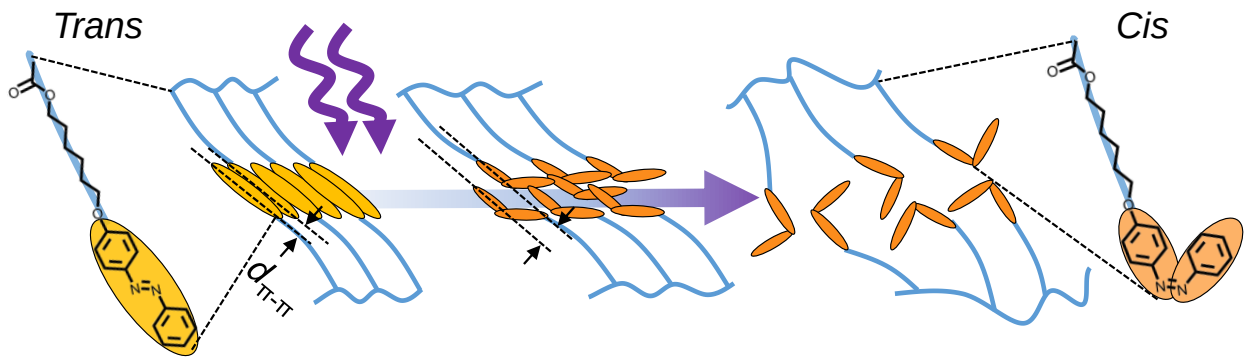

Figure 4.13. Schematic illustration of the conformation changes of the azopolymer driven by photoisomerization.

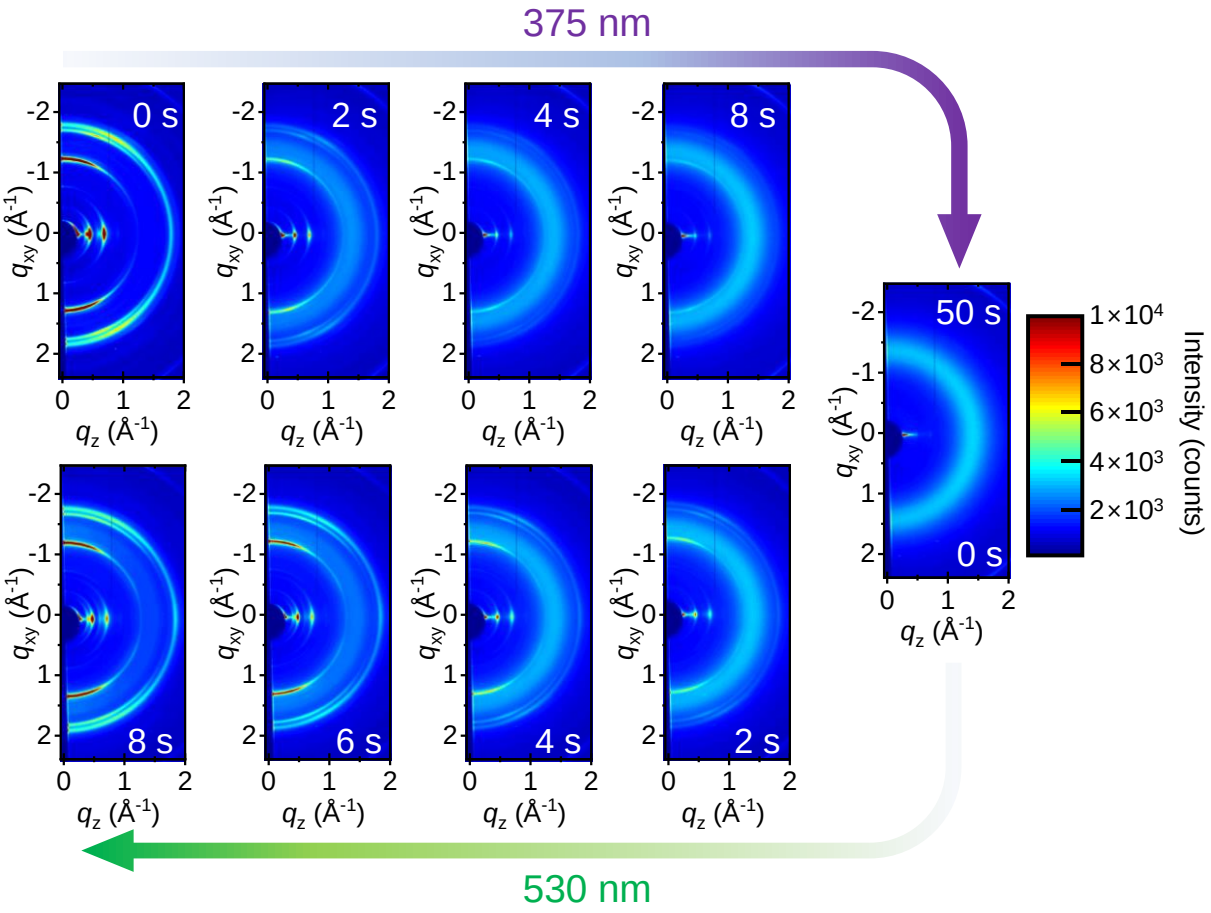

Figure 4.14. *In situ* 2-D GIWAXS diffraction pattern changes of a 280 nm *trans*-azopolymer film on the Al/polyimide/sapphire substrate during reversible crystal-to-liquid transition under UV (violet arrow) and green light illumination (green arrow) (630 mW cm^{-2}) at 30 °C.

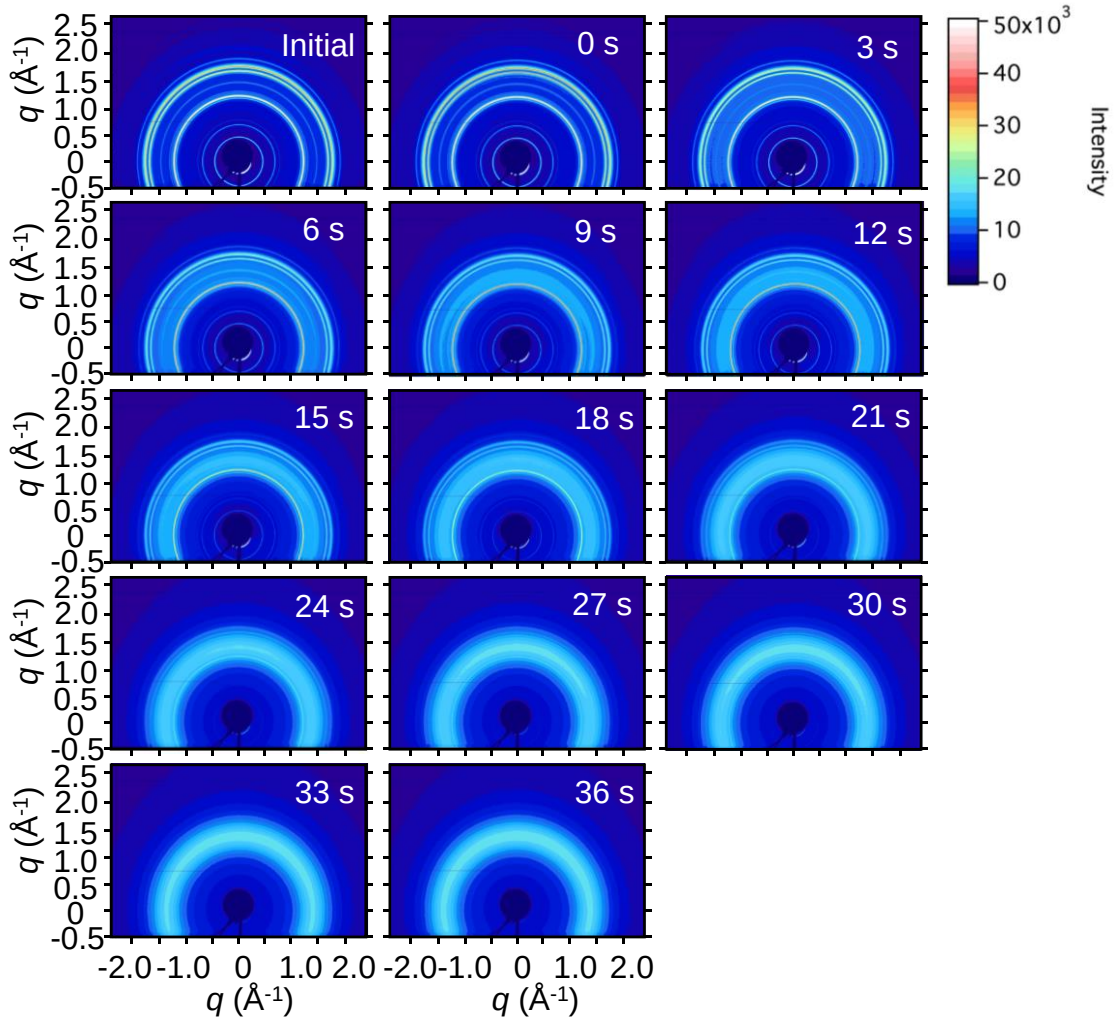

Figure 4.15. *In situ* transmission 2-D WAXS data of azopolymer powders during crystal-to-liquid transition under UV light illumination (630 mW cm^{-2}) at 25 ℃.

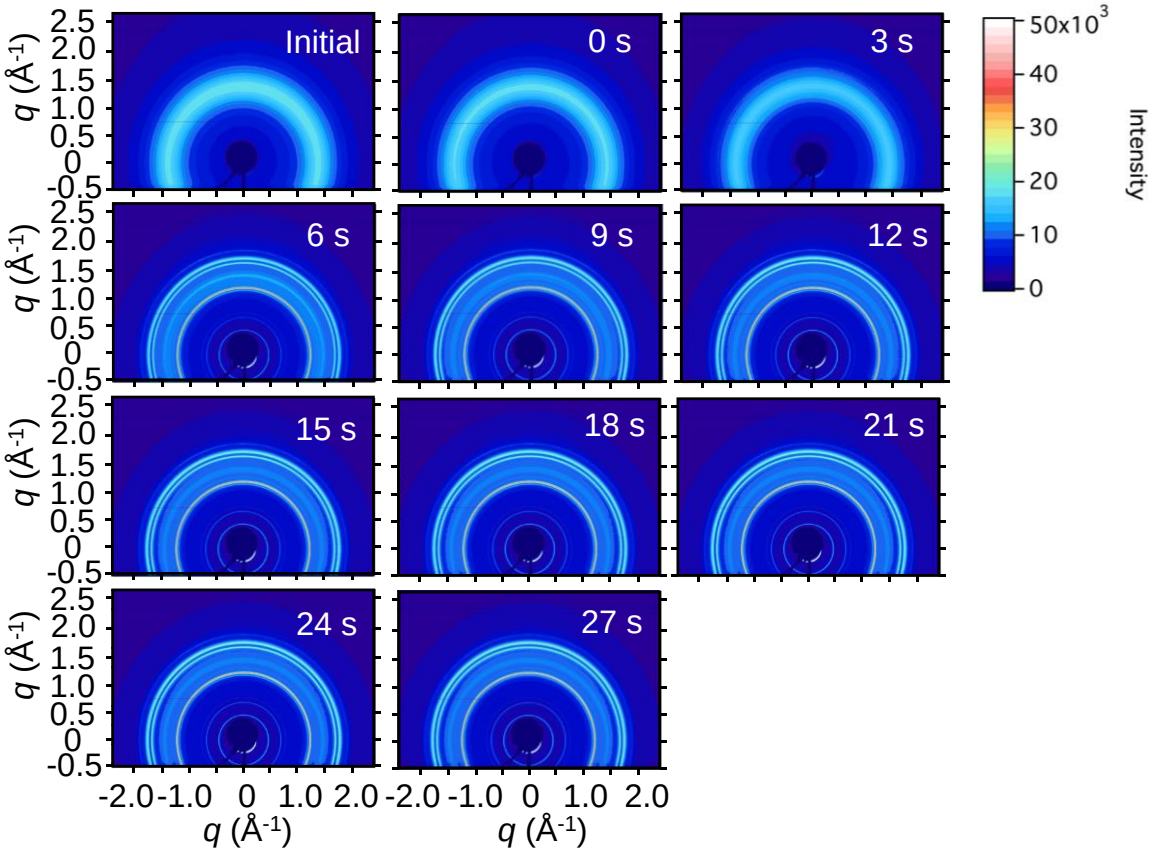

Figure 4.16. *In situ* transmission 2-D WAXS data of azopolymer powders during liquid-to-crystal transition under green light illumination (630 mW cm^{-2}) at 25 ℃, immediately following UV light illumination shown in Figure 4.15.

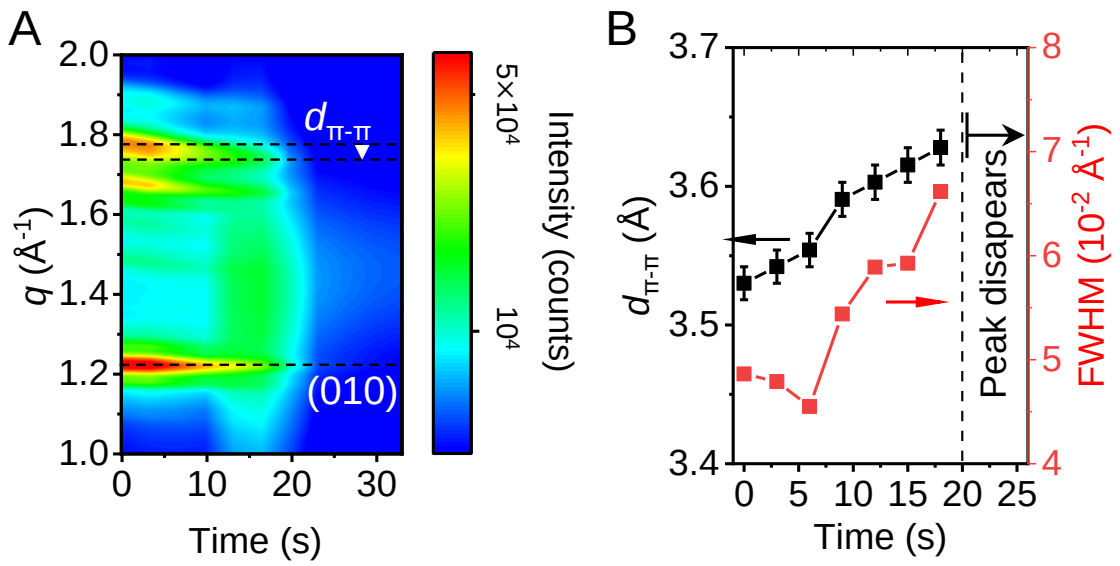

Figure 4.17. π-π stacking evolution of azobenzene groups during *trans*-to-*cis* photoisomerization. **A.** Azimuth integrated *in situ* transmission WAXS intensity of the azopolymer during the *trans*-to-*cis* transition driven by UV illumination (630 mW cm^{-2}). **B.** $d_{\pi-\pi}$ and full width at half maximum (FWHM) of the π-π stacking peak as a function of *trans*-to-*cis* photoisomerization time. Error bar represents the uncertainty of *q*. This time-dependent plot represents the $d_{\pi-\pi}$ diffraction shift in panel A.

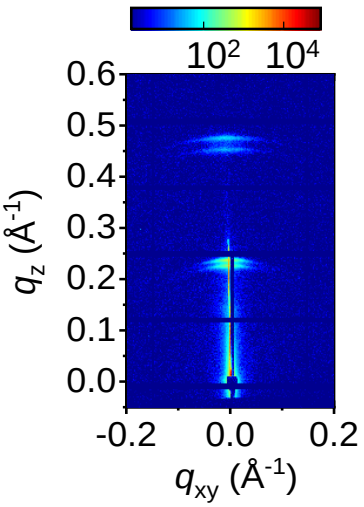

Figure 4.18. 2-D GISAXS diffraction pattern of the *trans*-azopolymer film.

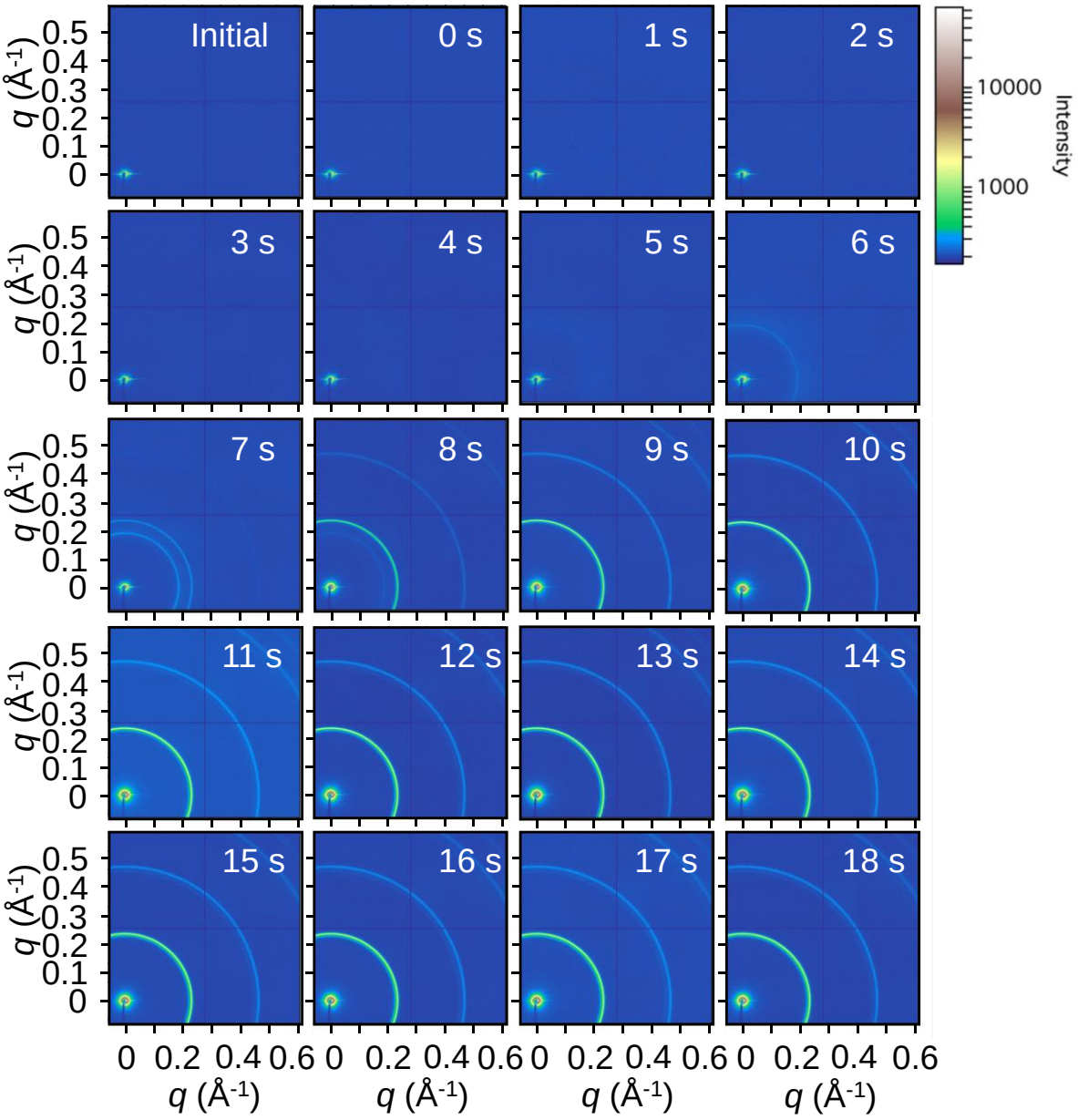

Figure 4.19. *In situ* transmission 2-D SAXS data of azopolymer powders during crystal-to-liquid transition under UV light illumination (630 mW cm^{-2}) at 25 °C.

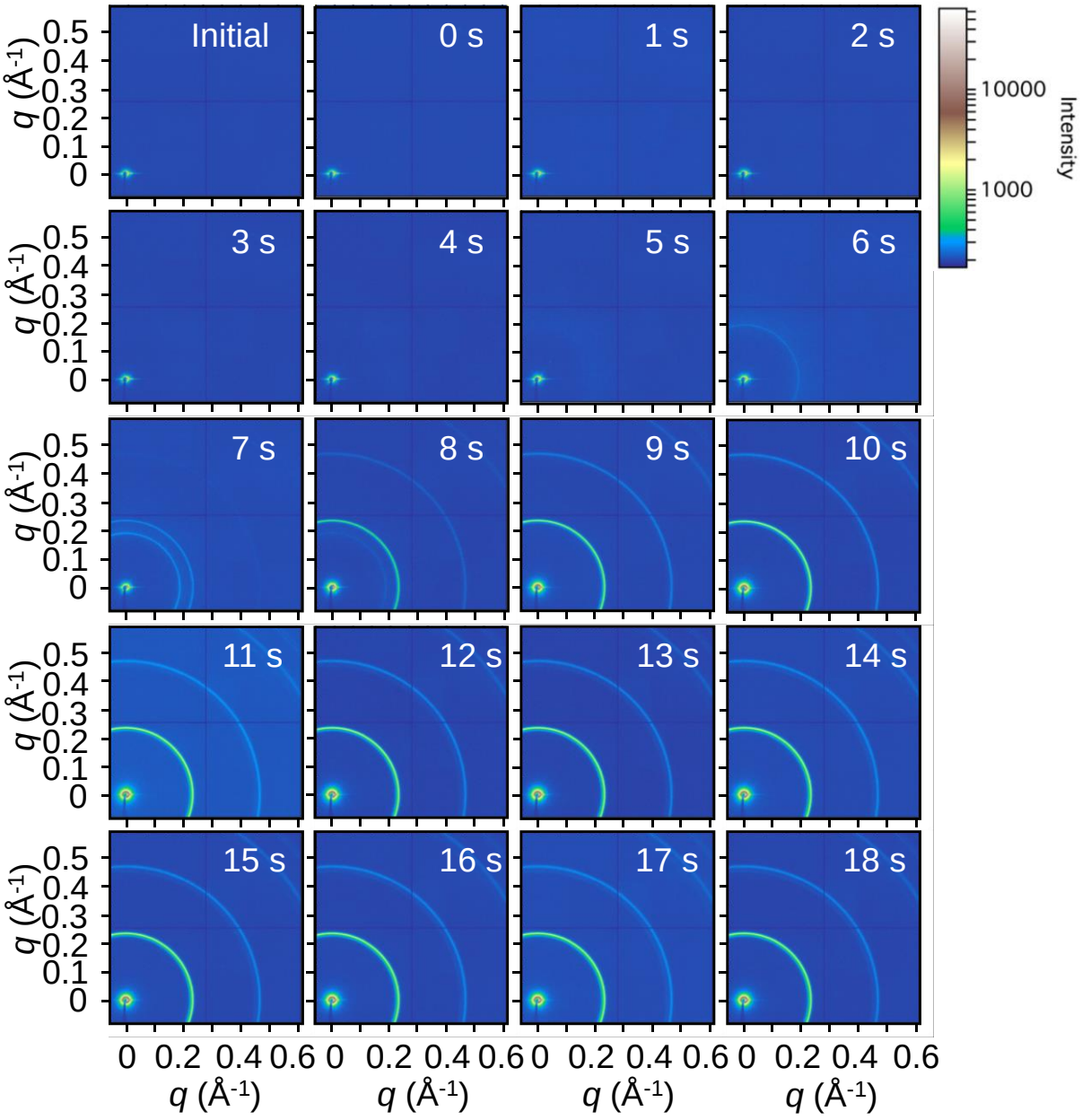

Figure 4.20. *In situ* transmission 2-D SAXS data of azopolymer powders during liquid-to-crystal transition under green light illumination (630 mW cm^{-2}) at 25 °C, immediately following UV light illumination shown in Figure 4.19.

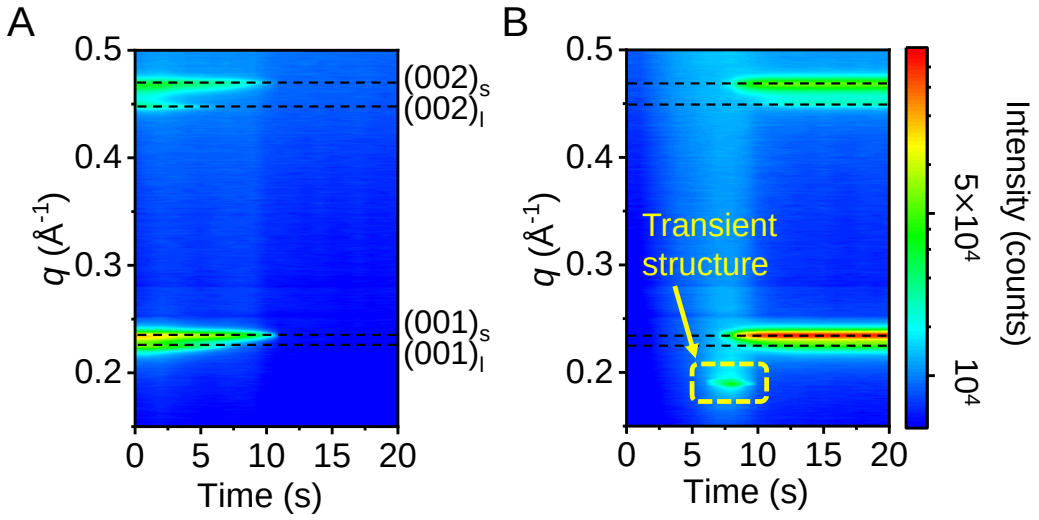

Figure 4.21. Photo-triggered reversible lamellar crystallization pathway. **A.** Azimuth integrated *in situ* transmission SAXS intensity of azopolymers during *trans*-to-*cis* photoisomerization (UV light). **B.** Azimuth integrated transmission SAXS intensity of azopolymers during the *cis*-to-*trans* photoisomerization (green light).

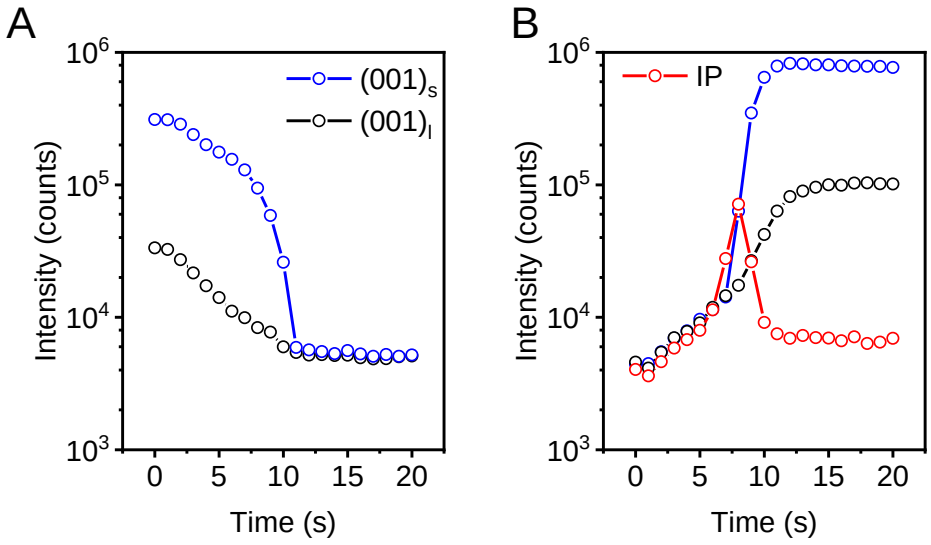

Figure 4.22. Long-range ordering changes under UV and green light illuminations. **A.** SAXS intensity profile of $(001)_l$ and $(001)_s$ peaks of azopolymer during *trans*-to-*cis* photoisomerization under UV light illumination (630 mW cm^{-2}). **B.** SAXS intensity profile of $(001)_l$, $(001)_s$ and intermediate phase (IP) peaks during *cis*-to-*trans* photoisomerization under green light illumination (630 mW cm^{-2}).

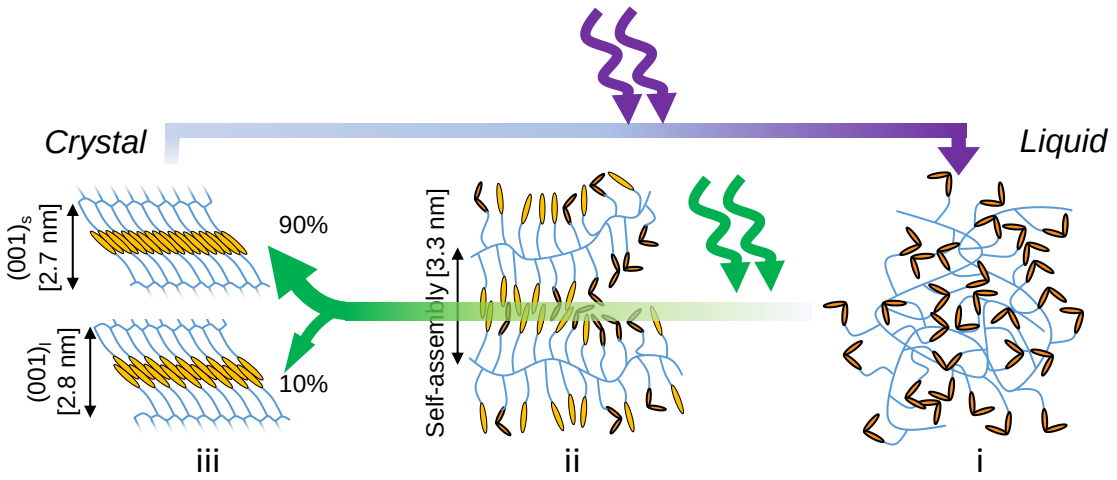

Figure 4.23. Schematic showing the suggested crystallization pathway under green light illumination (right to left). (i) Randomly distributed *cis*-azopolymer chains initially form (ii) an intermediate phase consisting of non-interdigitated polymer clusters followed by the formation of (iii) the interdigitated structure with long $(001)_l$ and short $(001)_s$ spacings.

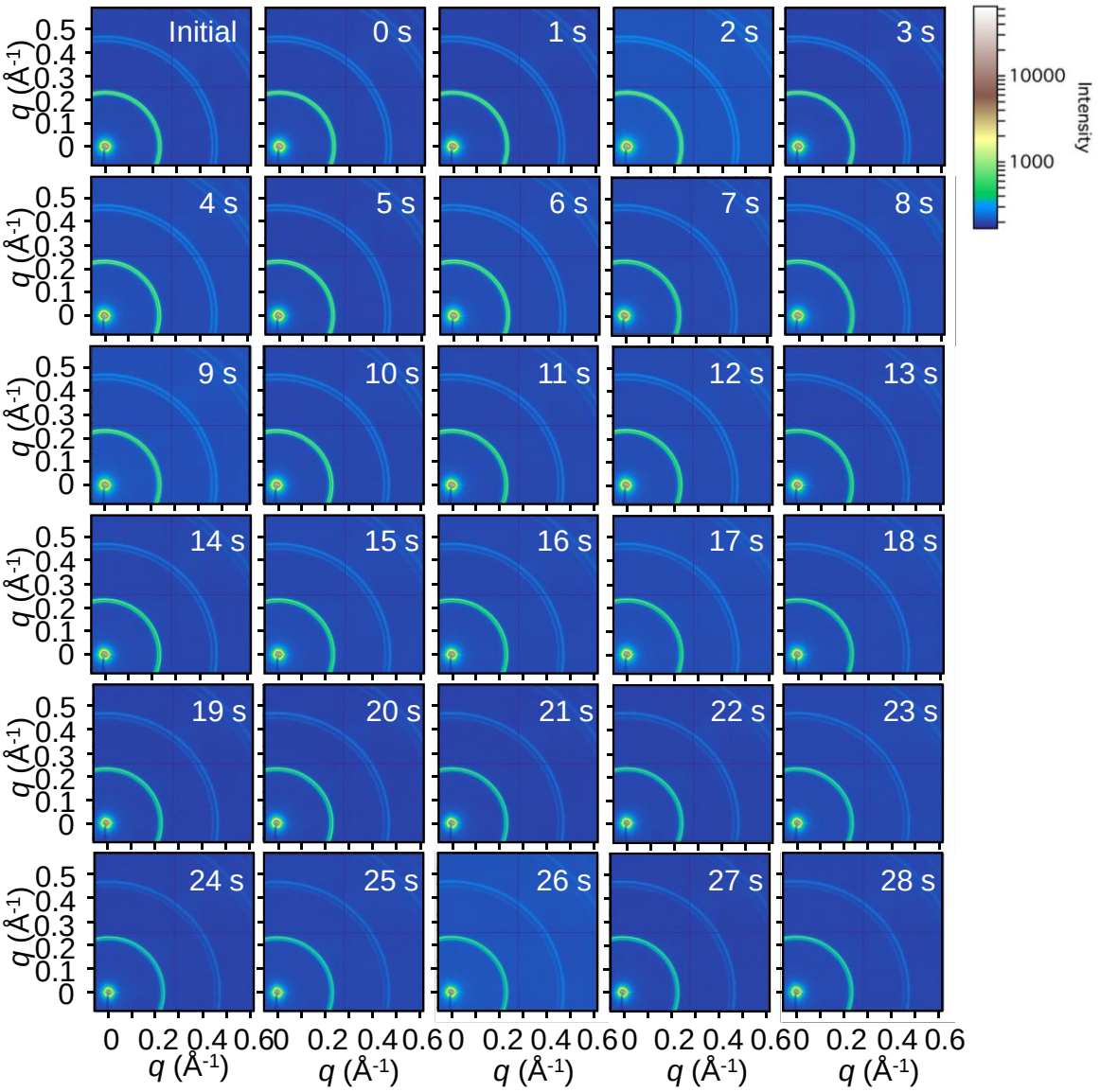

Figure 4.24. *In situ* transmission 2-D SAXS data of trans-azopolymer during selective *trans*-to-*cis* transition of $(001)_l$ by low intensity UV light illumination (130 mW cm^{-2}).

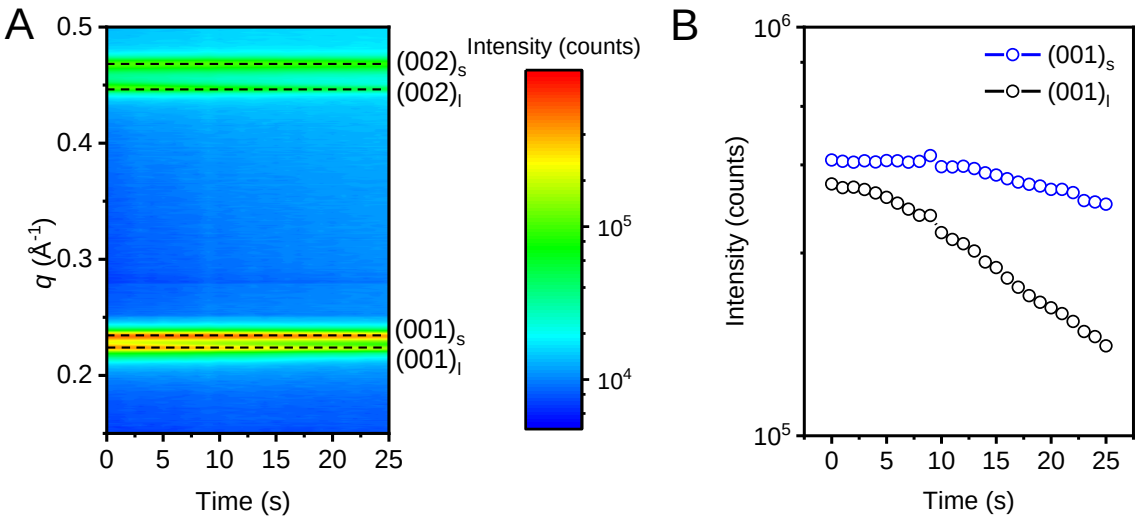

Figure 4.25. Selective *trans*-to-*cis* isomerization of partially-interdigitated lamellar. **A.** Azimuth integrated *in situ* transmission SAXS intensity data of azobenzene polymer during selective *trans*-to-*cis* transition by low-intensity UV light illumination (130 mW cm^{-2}). **B.** Azimuth integrated SAXS intensity plots of $(001)_l$ and $(001)_s$ peaks shown in panel A.

Table 4.1. Physical properties of *trans*- and *cis*-azopolymer. PDI and weight average molar mass (M_w) are calculated from the gel permeation chromatography (GPC) data. C is measured by frequency modulated TDTR and confirmed by DSC; T_g and T_m are measured by DSC; v_l, v_t, C_{11} and C_{44} of *trans*-azopolymer are calculated from picosecond acoustics and surface acoustic wave measurements; v_l of *cis*-azopolymer is calculated from picosecond interferometry measurement.

Isomer	PDI	M_W, g mol^{-1}	C, J cm^{-3} K^{-1}	T_g, °C	T_m, °C	v_l, nm ps^{-1}	v_t, nm ps^{-1}	C_{11}, GPa	C_{44}, GPa
Trans-azopolymer	1.37	2.4×10^4	1.6	31†	80	3.4	1.83	11.6	3.35
Cis-azopolymer			1.88	−48	—	1.78	—	—	—

†residual amorphous phase.
Dashed lines indicate that the quantity is not applicable or has not been measured.

4.11 REFERENCES

1. S. Hassan, R. Anandakathir, M. J. Sobkowicz, B. M. Budhlall, Tuning oxygen permeability in azobenzene-containing side-chain liquid crystalline polymers. *Polym Chem-Uk* **7**, 1452-1460 (2016).
2. H. Koshima, N. Ojima, H. Uchimoto, Mechanical Motion of Azobenzene Crystals upon Photoirradiation. *J Am Chem Soc* **131**, 6890-6891 (2009).
3. M. Hoshino *et al.*, Crystal Melting by Light: X-ray Crystal Structure Analysis of an Azo Crystal Showing Photoinduced Crystal-Melt Transition. *J Am Chem Soc* **136**, 9158-9164 (2014).
4. T. F. Miao *et al.*, Chirality Construction from Preferred pi-pi Stacks of Achiral Azobenzene Units in Polymer: Chiral Induction, Transfer and Memory. *Polymers-Basel* **10**, 612 (2018).
5. D. H. Han, X. Tong, Y. Zhao, T. Galstian, Y. Zhao, Cyclic Azobenzene-Containing Side-Chain Liquid Crystalline Polymers: Synthesis and Topological Effect on Mesophase Transition, Order, and Photoinduced Birefringence. *Macromolecules* **43**, 3664-3671 (2010).
6. S. Wu *et al.*, Supramolecular bisazopolymers exhibiting enhanced photoinduced birefringence and enhanced stability of birefringence for four-dimensional optical recording. *J Mater Chem* **20**, 5202-5209 (2010).
7. N. Makhiyanov, E. V. Temnikova, Glass-transition temperature and microstructure of polybutadienes. *Polymer Science Series A* **52**, 1292-1300 (2010).
8. H. W. Zhou *et al.*, Photoswitching of glass transition temperatures of azobenzene-containing polymers induces reversible solid-to-liquid transitions. *Nat Chem* **9**, 145-151 (2017).
9. T. T. Yuan, J. Dong, G. X. Han, G. J. Wang, Polymer nanoparticles self-assembled from photo-, pH- and thermo-responsive azobenzene-functionalized PDMAEMA. *Rsc Adv* **6**, 10904-10911 (2016).
10. D. Y. Li, P. Zhao, J. C. Zhao, D. G. Cahill, Generation and detection of gigahertz surface acoustic waves using an elastomeric phase-shift mask. *J Appl Phys* **114**, 143102 (2013).

11. K. E. O'Hara, X. Y. Hu, D. G. Cahill, Characterization of nanostructured metal films by picosecond acoustics and interferometry. *J Appl Phys* **90**, 4852-4858 (2001).
12. D. G. Cahill, Analysis of heat flow in layered structures for time-domain thermoreflectance. *Rev Sci Instrum* **75**, 5119 (2004).
13. K. Kang, Y. K. Koh, C. Chiritescu, X. Zheng, D. G. Cahill, Two-tint pump-probe measurements using a femtosecond laser oscillator and sharp-edged optical filters. *Rev Sci Instrum* **79**, 114901 (2008).
14. J. Shin *et al.*, Thermally Functional Liquid Crystal Networks by Magnetic Field Driven Molecular Orientation. *Acs Macro Lett* **5**, 955-960 (2016).
15. X. Xie *et al.*, High and low thermal conductivity of amorphous macromolecules. *Physical Review B* **95**, 035406 (2017).
16. X. J. Wang, V. Ho, R. A. Segalman, D. G. Cahill, Thermal Conductivity of High-Modulus Polymer Fibers. *Macromolecules* **46**, 4937-4943 (2013).
17. R. Shrestha *et al.*, Crystalline polymer nanofibers with ultra-high strength and thermal conductivity. *Nat Commun* **9**, 1664 (2018).
18. X. Xie, J. D. Dennison, J. Shin, Z. Diao, D. G. Cahill, Measurement of water vapor diffusion in nanoscale polymer films by frequency domain probe beam deflection. *Rev Sci Instrum* **89**, 104904 (2018).
19. S. F. Guo, A. Sugawara-Narutaki, T. Okubo, A. Shimojima, Synthesis of ordered photoresponsive azobenzene-siloxane hybrids by self-assembly. *J Mater Chem C* **1**, 6989-6995 (2013).
20. T. Seki, New strategies and implications for the photoalignment of liquid crystalline polymers. *Polym J* **46**, 751-768 (2014).
21. A. Bobrovsky *et al.*, Photo-Orientation Phenomena in Photochromic Liquid Crystalline Azobenzene-Containing Polymethacrylates with Different Spacer Length. *Macromol Chem Physic* **218**, 1700127 (2017).

CHAPTER 5: THERMAL CONDUCTIVITY CHANGES OF CONVERSION, INTERCALATION AND ALLOYING ELECTRODE MATERIALS DURING ELECTROCHEMICAL REACTION WITH LITHIUM IONS

Parts of Chapter 5 are being prepared for a publication in "Thermal conductivity changes of conversion, intercalation and alloying electrodes during electrochemical reaction with Li^+ ions," Jungwoo Shin, Sanghyeon Kim, Hoonkee Park, Ho Won Jang, David G. Cahill, Paul V. Braun, *manuscript in preparation*.

In Chapter 5, in collaboration with Sanghyeon Kim in Braun group at Illinois, we studied thermal and mechanical properties of five Li-ion electrode materials during charge/discharge cycles with Li^+ ions. *In situ* time-domain thermoreflectance (TDTR) and picosecond acoustics were used to characterize the thermal and elastic properties of the five electrodes with varying Li^+ ion contents in the electrode materials. The conversion electrodes, Fe_2O_3 and NiO showed irreversible thermal conductivity and elastic modulus loss of up to 80% and 40% after the first cycle, and eventually became static thermal insulator regardless of Li^+ ion contents. The intercalating V_2O_5 and TiO_2 electrodes exhibited a stable and reversible thermal conductivity switching as a function of Li^+ ion contents without the irreversible thermal conductivity and elastic modulus loss. The alloying Sb electrode showed the highest thermal conductivity switching ratio $r \sim 20–30$ during the first few cycles, which gradually decreased with cycling. We attribute these large differences in the thermal and mechanical switching properties among the three different mechanisms to the existence of Li-ion pathways in the crystal structure of electrode materials. While the irreversible thermal conductivity and mechanical modulus loss of conversion and alloying electrode materials are caused by the lattice disordering and structural

degradation by Li^+ ions, the intercalation electrodes maintain stable Li^+ ion pathway and crystal structure during cycling.

5.1 SELECTION AND PREPARATION OF ELECTRODE MATERIALS

Phase transitions in materials result in discontinuities of physical properties (e.g., volume, heat capacity, mechanical strength, thermal conductivity). Here, I am particularly interested in the change in thermal conductivity during a phase transition of electrode materials induced by Li^+ ion insertion, which can be dramatic due to the large-scale rearrangements of atoms and their associated network of bond that carries heat. In Chapter 5, I chose five electrode materials for candidates showing large changes in thermal conductivity under electrochemical reaction with Li^+ ions. I took advantage of the superior temporal resolution of *in situ* TDTR, which is essential to study thermal conductivity changes of electrode materials during characteristic redox reactions.

As discussed in Chapter 2.5, in collaboration with Sanghyeon Kim in Braun group at Illinois, we used Al film as a current collector of the electrode materials as well as a transducer for *in situ* TDTR measurements. Al has a stable electrochemical potential range above 0.5 V vs. Li/Li^+, compatible with a few anode materials including 3d-metal oxides and Sb anodes and all cathode materials(*1*). Here, we present a systematic experimental platform for the investigation of various electrode materials with switchable conductivity caused by electrochemically driven solid-solid phase transitions with negligible (<10%) to extreme volume change (300%).

The electrochemical lithiation/delithiation of electrodes undergo three electrochemical phase-transition mechanisms: conversion, intercalation and alloying. We selected Fe_2O_3 and NiO

as conversion systems; TiO_2 and V_2O_5 as intercalation systems; and Sb as an alloying system. The electrochemical reactions for the three electrochemical systems are described in the following:

$$M + xLi^+ + xe^- \Leftrightarrow Li_xM \text{, alloying} \quad (5.1)$$

$$ZO_x + 2xLi^+ + 2xe^- \Leftrightarrow xLi_2O + Z \text{, conversion} \quad (5.2)$$

$$QO_y + xLi^+ + xe^- \Leftrightarrow Li_xQO_y \text{ , intercalation} \quad (5.3)$$

where x is the Li^+ ion contents in the electrode, M = Sb, Z = Fe, Ni, and Q = V, Ti. These are well-known Li-ion battery electrodes exhibiting distinct electrochemical reaction mechanisms which may impact the resulting thermal conductivity transitions(*2-4*).

Fe_2O_3, NiO, V_2O_5, and TiO_2 films were deposited on the Al/SiO_2/sapphire substrates by an electron beam evaporator (Rocky Mountain Vacuum Tech, Englewood, CO). The base pressure, e-beam voltage and current for the e-beam deposition were set to 10^{-6} Torr, 3.4 kV, and 20 mA, respectively. The as-deposited metal oxide samples were annealed in the following conditions: Fe_2O_3 in Air at 400 °C for 1 h; NiO in Ar at 300 °C for 2 h; V_2O_5 in air at 500 °C for 1 h; TiO_2 in Air at 400 °C for 2 h. This heat treatment dramatically increased the initial thermal conductivity of electrodes. For example, Figure 5.1 shows measured and fitted TDTR data of the V_2O_5/Al/SiO_2/sapphire sample before and after the heat treatment. The inset is a cross-sectional scanning electron microscopy (Hitachi S-4800 High-Resolution SEM) image of the V_2O_5/Al/SiO_2/sapphire sample. Thermal conductivity of V_2O_5 increased from 0.9 W m^{-1} K^{-1} to 8.4 W m^{-1} K^{-1} due to the improvement of crystallinity and the reduction of

defects(*5*). The electrochemical properties of Fe_2O_3, NiO, V_2O_5, and TiO_2 were tested in a home-made liquid jar cell with a 1 M lithium perchlorate ($LiClO_4$) dissolved in ethylene carbonate (EC) and dimethyl carbonate (DMC) (1:1 by volume) solution as a liquid electrolyte and a Li metal foil as the counter electrode.

For the alloying system, Sb was deposited by thermal evaporation of Sb pellets (1-3 mm, Kurt J. Lesker, 99.999 %) on Au/Al/SiO_2/sapphire substrate. Note that 15-nm Au film with a 2-nm Cr adhesion layer was deposited on top of Al transducer to provide better adhesion between Sb and the substrate. Compared with Al with a native oxide layer which does not have a high adherence with Sb, Au can form a thin intermetallic $AuSb_2$ layer with much improved adherence(*6*).

The all-solid-state cell made of Ti metal rods and polyaryletheretherketone spacer was employed to test the electrochemical properties of Sb with the Li_2S:P_2S_5 solid electrolyte and In-Li alloy counter electrode. Details regarding the experimental setup and geometry of the liquid and solid electrolyte cells are described in Chapter 2.5.

5.2 VOLUME EXPANSION OF ELECTRODE MATERIALS

While intercalating TiO_2 and V_2O_5 exhibit negligible volume changes during cycling, conversion and alloying electrode show markedly large volume expansion during lithiation process. The theoretical expansion ratio of conversion electrodes during electrochemical reactions with Li^+ ions (M_yO_x + 2_xLi ↔ xLi_2O +yM) was calculated as $V_{lithiatd}/V_0$ = $\rho_{M_yO_x} / M_{M_yO_x} \cdot (xM_{Li_2O} / \rho_{Li_2O} + yM_M / \rho_M)$ where M_yO_x can be Fe_2O_3 and NiO; ρ is the

density and M is the molecular weight. The theoretical volume expansion ratio of the alloying electrode Sb (Sb + 3Li ↔ Li_3Sb) was calculated as $V_{lithiatd}/V_0 = \rho_{Sb} / M_{Sb} \cdot (M_{Li_3Sb} / \rho_{Li_3Sb})$.

While NiO and Fe_2O_3 exhibited $V_{lithiatd}/V_0$ ~ 1.9; and Sb exhibited $V_{lithiatd}/V_0$ ~ 2.3 actual volume changes of the electrode materials were measured by cross-sectional SEM. Figure 5.2 shows cross-sectional SEM images of five electrodes deposited on Al/SiO_2/sapphire substrates at the initial (after the heat treatment), lithiated and delithated states. We compared the thicknesses before and after the first lithiation reaction. For Fe_2O_3, the initial thickness $d_{Fe_2O_3} = 350\,\text{nm}$; the thickness after the first lithiation $d_{Fe_2O_3\text{-discharge}} = 836\,\text{nm}$; and the experimental volume expansion ratio $d_{Fe_2O_3\text{-lithiated}} / d_{Fe_2O_3} = 2.4$, which is ~25% larger than the theoretical volume expansion ratio described above. This discrepancy can be attributed to the irreversible solid-electrolyte interphase (SEI) layer formation, which also accounts for the irreversible discharge capacity loss at the first cycle. The thickness of the lithiated state was also larger than the initial state by $d_{Fe_2O_3\text{-delithiated}} / d_{Fe_2O_3} = 1.16$ (irreversible volume expansion). NiO showed a slightly lower volume expansion as $d_{NiO\text{-lithiated}} / d_{NiO} = 2.0$, comparable with the prediction, and $d_{NiO\text{-delithiated}} / d_{NiO} = 1.2$.

Contrary to the conversion electrodes, intercalating V_2O_5 and TiO_2 showed negligible volume change. The experimental volume expansion ratio of TiO_2 (anatase) $d_{TiO_2\text{-lithiated}} / d_{TiO_2} = 1.16$, which is slightly larger than the theoretical volume expansion of 4%(*7*). After the first discharge, TiO_2 showed a small irreversible volume expansion of $d_{TiO_2\text{-delithiated}} / d_{NiO} = 1.03$. Likewise, V_2O_5 showed a volume expansion of < 1 % during charge/discharge cycles.

The most dramatic experimental volume expansion was observed for Sb, with severe structural degradation. Figure 5.3 shows cross-sectional SEM and surface SEM images of Sb/Au/Al/SiO_2/sapphire samples at the initial and lithiated states. Note that we were not able to measure the thickness of the delithiated Sb film due to the delamination of the film with the irregular mixing with the solid electrolyte. The cross-sectional and surface SEM images at the lithiated state (Li_3Sb) show a severe pulverization of Sb film and the formation of irregular SEI layer (*8*), typical phenomena observed for bulk alloying electrode materials with poor electrochemical properties (*9*).

5.3 PHASE TRANSITIONS OF ELECTRODE MATERIALS

To determine the phase transition of the electrode materials, we performed Rutherford Backscattering Spectrometry (RBS) using high-energy He^+ ion beam (0.5-2.0 MeV) from the high-energy ion-beam accelerator (3SDH Pelletron, NEC), and X-ray diffraction (XRD) using Panalytical Phillips X'pert with a Cu-Kα radiation (λ = 0.154 nm) at Materials Research Laboratory at UIUC. Figure 5.4 shows measured and fitted RBS data for the conversion and intercalation electrode materials deposited on Al/SiO_2/sapphire substrates. The calculated atomic ratio of Fe_2O_3 electrode is Fe:O = 41.4:58.5, suggesting the presence of Fe-rich phases such as Fe_3O_4. RBS signal fluctuation of Ni peak of NiO sample (Figure 5.4B) suggested an inhomogeneous phase mixing with varying atomic ratios of Ni:O = 55.2:44.8 (bottom) 65:35 (middle) and 50:50 (top). The oxygen gradient from the top layer indicates incomplete oxidation of NiO after the heat treatment. Figures 5.4C-D show RBS data of TiO_2 and V_2O_5 on Al/SiO_2/sapphire substrates. The calculated atomic ratios are Ti:O = 31.4:68.6 and V:O =

28.7:71.3, close to the theoretical values of TiO_2 and V_2O_5: Ti:O = 33.3:66.7 and V:O = 28.6:71.4.

Figure 5.5 shows XRD data of five electrode materials at the initial, lithiated state and delithated state. Co-existent of Fe_2O_3 and Fe_3O_4 phases and NiO and Ni phases were observed, consistent with the off-stoichiometries observed in RBS measurements. After the first lithiation reaction, the 3-d metal oxide conversion electrode materials lost crystal structures, resulting in amorphization and the dramatic structural change associated with the insertion of Li^+ ion (*10*). Metal nanoclusters (Ni and Fe) embedded in electrically insulating amorphous Li_2O matrix do not give rise of XRD peak at the delithiated state. Subsequent delithiation does not recover the crystalline structure but amorphous metal oxide phase.

In contrary, intercalation electrode materials exhibited a stable crystal structure after cycling. Among TiO_2 polymorphs, we examined anatase TiO_2 (α phase). α-TiO_2 is a tetragonal phase consisting of distorted 1-D TiO_6 octahedra chains with vacancy channels, which work as a diffusion path for Li^+ ions(*11*). Insertion of Li^+ ions into these vacancies resulted in coulombic repulsion, leading to the phase transition to orthorhombic Li-titanite phase (Li_xTiO_2, $x < 0.6$, β phase), with a lattice expansion in b axis and contraction in c-axis (*12*). Further insertion of Li^+ ions resulted in tetragonal γ phase ($LiTiO_2$).

Figure 5.5C shows XRD data of TiO_2 before and after the lithiation and delithiation. After the lithiation, the (020) diffraction peak of anatase TiO_2 phase shifted from $2\theta = 48.33$ (b = 3.78 Å) to 44.68º (4.054 Å), which are close to α-TiO_2 (b = 3.792 Å) and β-Li_xTiO_2 (b = 4.084 Å) phases(*13*). On the other hand, V_2O_5 shows a mixture of multiple phases with varying *x* of $Li_xV_2O_5$ where co-existent α ($x< 0.1$), ε ($0.35<x< 0.7$), δ ($x<1$) and γ ($1<x\leq2$) phases were

observed (*14*, *15*). Figure 5.5D shows XRD data of V_2O_5 where (001) textured crystalline α-$Li_xV_2O_5$ film at the initial state was transformed to a binary mixture of δ-$Li_xV_2O_5$ and γ-$Li_xV_2O_5$ phases after the lithiation and returned to the initial α-$Li_xV_2O_5$ phase after the delithiation(*15*).

Figure 5.5E shows XRD data of Sb at the initial state and after the first discharge. The Sb at the initial state turned into Li_3Sb phase with after the lithiation. The additional diffraction peaks of Li_2S came from a trace of Li_2S:P_2S_5 solid-electrolyte powders on the surface of the recovered electrode. Note that we were not able to perform *ex situ* XRD measurements for the delithated Sb film which was strongly adhered to the Li_2S:P_2S_5 pellet.

5.4 THERMAL CONDUCTIVITY AND ELASTIC MODULUS CHANGES OF IRON(III) OXIDE AND NICKEL(II) OXIDE

Before *in situ* TDTR measurements, we carried out *ex situ* TDTR measurements of 500 ^oC heat treated iron(III) oxide (Fe_2O_3) deposited on Au (60 nm)/SiO_2 substrates. Figure 5.6A shows as-prepared (after annealing), discharged and charged Fe_2O_3 (335 nm)/Au (60 nm)/SiO_2 samples. Fe_2O_3 has been known to exhibit reversible and stable electrochemical conversion reactions, can be simply observed by the color of the sample. After the lithiation process, yellowish Fe_2O_3 film reduced to black Fe + Li_2O phases, which returned to dark yellow film, indicating a partial recovery of Fe_2O_3 phase which might contain a trace of Fe and/or Fe_3O_4 phase. Figure 5.6B shows a differential capacity curve (d*Q*/d*V*) of the Fe_2O_3 (335 nm)/Au (60 nm)/SiO_2 with the Li metal counter electrode in 1 M $LiClO_4$ dissolved EC/DMC electrolyte. The cathodic and anodic peaks observed at 1.55 and 0.8 V vs. Li/Li^+ correspond to the conversion reaction of Fe_2O_3 ($2Fe_2O_3 + Li \leftrightarrow 6Li_2O + 4Fe$).

After lithiation/delithiation reactions, we deposited Al transducer films on as-prepared, lithiated and delithiated Fe_2O_3/Au/SiO_2 samples for *ex situ* TDTR measurements. Samples were sealed in an Ar-filled container and brought to the Al deposition chamber to minimize the exposure to air. Figure 5.6C shows measured in-phase TDTR voltage of the as-prepared Al/Fe_2O_3/Au/SiO_2 sample. The time interval between peaks correspond to the acoustic echoes reflecting between air/Al and Al/Fe_2O_3 interfaces, (Δt_{p1} = 33.5–34.5 ps) and Al/Fe_2O_3 and Fe_2O_3/Au interfaces (Δt_{p2} = 90–90.5 ps) where $\Delta t_{p1} = 2h_{Al}/v_{Al}$, h_{Al} and v_{Al} are the thickness and the longitudinal speed of sound of Al (6.42 nm ps^{-1}). $v_{Fe_2O_3}$ was calculated using $v_{Fe_2O_3} = 2h_{Fe_2O_3}/\Delta t_{p2}$ where $h_{Fe_2O_3}$ was measured by SEM. Then, $v_{Fe_2O_3}$ was converted to $C_{11} = \rho_{Fe_2O_3} v_{Fe_2O_3}^2$ where $\rho_{Fe_2O_3}$ is the density of Fe_2O_3. Figure 5.6D shows measured and fitted *ex situ* TDTR data of as-prepared and lithiated Fe_2O_3. We observed a dramatic thermal conductivity decrease from 7.6 W m^{-1} K^{-1} to 0.44 W m^{-1} K^{-1} after the first lithiation. TDTR signal of the charged Fe_2O_3 sample is identical to the lithiated Fe_2O_3 sample without thermal conductivity recovery. For the conversion nickel(II) oxide (NiO) electrode, we observed a moderate thermal conductivity loss from 7.7 W m^{-1} K^{-1} to 3.1 W m^{-1} K^{-1} after the first delithiation, which was recovered to 4 W m^{-1} K^{-1} after the delithiation.

To study the thermal conductivity changes of Fe_2O_3 and NiO as a function of Li^+ contents x in $Fe_2O_3 + 6xLi \leftrightarrow 3xLi_2O + 2xFe + (1-x)Fe_2O_3$ and $NiO + 2xLi \leftrightarrow xLi_2O + xNi + (1-x)NiO$, we used the liquid electrolyte cell with the Fe_2O_3 or NiO/Al/SiO_2/sapphire substrate for *in situ* TDTR measurements. See Chapter 2.5 for the detail of the liquid-electrolyte cell construction. Alloying and conversion materials in which the phase transformation initiates from supersaturation of Li^+ ions in the electrode surface, forming metastable or unstable phase. As the discharge/charge process proceeds, the supersaturated Li^+ ions diffuse to the bulk,

moving the boundary between the Li-ion rich and poor phases. Here, we estimated *x* of the Fe_2O_3 and NiO electrode materials based on their volumes and theoretical capacities.

First of all, we measured picosecond echoes of NiO and Fe_2O_3 with varying *x*. Figure 5.7 shows the measured in-phase TDTR signal of NiO/Al/SiO_2/sapphire substrate in the liquid electrolyte cell. Note that the echoes were generated from the reflection longitudinal lattice waves between i) NiO/Al and Al/SiO_2 interphases and ii) electrolyte/NiO and NiO/Al interphases. The first acoustic signals are static and marked with a dashed black line, and the second acoustic signals are variable and marked with black arrows with respect to the Li^+ ion contents. Note that we were not able to measure the acoustic signal from the lithiated Fe_2O_3 sample due probably to the pulverization and structural degradation associated with the large volume change of Fe_2O_3.

Figure 5.8A shows thermal conductivity and calculated C_{11} of as-prepared Fe_2O_3. Similar to what we observed in *ex situ* TDTR, thermal conductivity of Fe_2O_3 dropped from 4.6 W m^{-1} K^{-1} to 0.6 W m^{-1} K^{-1} after the first lithiation, which does not return to the initial state after the delithiation. The reason for the low thermal conductivity of Fe_2O_3 measured by *in situ* TDTR compared with *ex situ* TDTR (4.6 vs. 7.6 W m^{-1} K^{-1}) is the difference of annealing temperature (400 vs. 500 ^oC). Figure 5.8B shows voltage curves of Fe_2O_3 during the galvanostatic charge/discharge cycling (5 cycles). Figure 5.8C shows thermal conductivity and calculated C_{11} value of NiO from *in situ* TDTR measurements of the liquid electrolyte cell with NiO/Al/SiO_2/sapphire sample.

Similar to Fe_2O_3, NiO showed irreversible decreases in thermal conductivity and C_{11} from 7.7 to 3.1 W m^{-1} K^{-1} and from 329 to 190 GPa during the first lithiation process,

suggesting the amorphization and lattice softening of NiO during the conversion reaction. The elastic modulus shift was calculated from the acoustic echo shift from 95 ps (x = 0) to 138 ps (x = 0.71). The acoustic echo shifts with respect to x, $\Delta t_{p2}(x)$, ware used to calculate the change of longitudinal speed of sound, $v_{NiO}(x)$. We estimated the thickness and the density of NiO changes linearly with respect to x in $x$$Li_2O$ + xNi + (1-x)NiO where $C_{11}(x) = \rho_{Fe_2O_3}(x)\, v_{Fe_2O_3}(x)^2$. After the first discharge, thermal conductivity and C_{11} of NiO were recovered to 4.3 W m^{-1} K^{-1} and 218 GPa.

Despite of large decreases in thermal conductivity and elastic modulus of Fe_2O_3 and NiO with respect to x during lithiation, they remained almost the same during the delithiation process. This irreversible loss of thermal conductivity and elastic modulus after the lithiation are associated with the irreversible electrochemical capacity at the first discharge as shown in Figure 5.8D.

Figure 5.9 shows the voltage and thermal conductivity changes of Fe_2O_3 and NiO measured by *in situ* TDTR during five galvanostatic charge/discharge cycles at the current density of 330 and 182 mA g^{-1}, respectively. While Fe_2O_3 became a thermal insulator (<1 W m^{-1} K^{-1}) after the first discharge NiO showed a small fluctuation of thermal conductivity attributable to the changes in density and elastic modulus. Since Fe_2O_3, NiO, and Li_2O are semiconducting oxides with band gaps of 2.1 eV, 3.5 eV, and 4.8 eV(*16*) the major heat carriers for these materials are phonon at room temperature. As observed from XRD, conversion electrodes undergo Li-ion induced amorphization at the first discharge(*10*), which is responsible for the large loss of the lattice thermal conductivity after the first lithiation.

Further cycling would result in changes of density and elastic modulus as a function of *x*, which leads to a small change in the minimum lattice thermal conductivity as (*17*)

$$\Lambda_{\min} = \left(\frac{\pi}{6}\right)^{1/3} k_B n^{3/2} \sum_{i=1}^{3} v_i \left(\frac{T}{\Theta_i}\right)^2 \int_0^{\Theta_i/T} \frac{x^3 e^x}{(e^x - 1)} dx \qquad (5.4)$$

where k_B is the Boltzmann constant, n is the atomic number density, v_i is the longitudinal (i = 1) and transverse (i = 2,3) speeds of sound, and Θ_i is the Debye temperature. n is calculated from the density ρ and molecular weight M of the electrode material, $n = \rho N_A / M$ where N_A is the Avogadro number. v_i can be reduced from longitudinal modulus C_{11} and transverse elastic modulus C_{44} with density ρ where $v_1 = \sqrt{C_{11}/\rho}$ and $v_{2,3} = \sqrt{C_{44}/\rho}$.

After the first lithiation (amorphization), we expect that the density and speed of sound changes could set the minimum boundary of the conversion electrode materials. However, we calculated $\Lambda_{\min}(Li_2O)$ = 1.75 W m^{-1} K^{-1}, $\Lambda_{\min}$(Fe) = 1.16 W m^{-1} K^{-1} and $\Lambda_{\min}(Fe_2O_3)$ = 1.41 W m^{-1} K^{-1}, which are larger than the measured thermal conductivity of discharged Fe_2O_3. We attribute this low thermal conductivity of Fe_2O_3 to the formations of SEI and voids, which account for the additional volume expansion (~40%) measured by SEM after the first lithiation.

Figure 5.10 shows the specific charge and discharge capacities of Fe_2O_3 and NiO during five galvanostatic cycling. NiO shows the first discharge capacity of 508 mAh g^{-1}, which is 71% of the theoretical capacity (718 mAh g^{-1}). After the first discharge, two-thirds of the initial capacity of NiO was not recovered during the following cycles. Fe_2O_3 showed the first discharge capacity of 1080 mAh g^{-1}, which is close to the theoretical capacity of 1000 mAh g^{-1}. However, this value gradually decreased to 390 mAh g^{-1} during the following cycles.

This irreversible capacity loss could be related to the formation and growth of insulating SEI with the pulverization of active materials. The irreversible structural degradation, SEI, phase separation and electric conductivity decreases of metal oxide conversion electrode (*18*) can be associated with the ultralow thermal conductivity of discharged Fe_2O_3.

5.5 THERMAL CONDUCTIVITY AND ELASTIC MODULUS CHANGES OF TITANIUM(IV) OXIDE AND VANADIUM(V) OXIDE

Studies on intercalation electrode materials have shown reversible thermal conductivity switching along with stable crystal structures during lithiation/delithiation. Examples are Li_xCoO_2, Li_xMoS_2 and Li_xP with r of 1.5(*19*) 2.0(*20*) and 1.65(*21*). Here, we chose semiconducting titanium(IV) oxide (TiO_2, anatase) and vanadium(V) oxide (V_2O_5) with band gaps of 3.3 eV and 2.3 eV(*16*). At room temperature, we expect that most heat is carried by lattice for TiO_2 and V_2O_5. With the reversible insertion and desertion of Li^+ ion between the van der Waals V_2O_5 layers and vacancy channels of TiO_2, we hypothesized that the phonon dispersion of these intercalation electrodes changes with varying Li^+ ion contents.

Figure 5.11 shows picosecond acoustic data of TiO_2 and V_2O_5 on Al/SiO_2/sapphire substrates with varying Li^+ ion contents during electrochemical charge/discharge reaction in the liquid electrolyte cell. As TiO_2 and V_2O_5 exhibited (001) textured crystal structures the measured v_l is considered as the speed of sound in (001) direction. The v_l of as-prepared V_2O_5 (2.7 nm ps^{-1}) is closed to literature value of the speed of sound in the (001) direction (across the van der Waals interfaces, 2.5 nm ps^{-1}) of V_2O_5 (*22*). Contrary to alloying Fe_2O_3 and NiO, intercalation TiO_2 and V_2O_5 showed increases in v_l from 6.5 nm ps^{-1} to 7.8 nm ps^{-1} and from 2.7 nm ps^{-1} to 2.8 nm ps^{-1}, respectively.

The monotonic increase in speed of sound of TiO_2 and V_2O_5 are related to the elastic moduli increases with respect to x in the intercalation materials. v_l of TiO_2 and V_2O_5 were converted and presented as C_{33} in Figure 5.12 with thermal conductivity measured by TDTR. Here, we estimated x of V_2O_5 based on the potential plateau and x of the Li_xTiO_2 which clearly exhibited two potential plateaus corresponding to Li^+ ion insertion to ε ($0.35<x< 0.7$), δ ($x<1$) and γ ($1<x\leq2$) phases (*23*). x of $LiTiO_2$ was estimated based on the volume and theoretical capacity. We note that Li^+ ion insertion to anatase TiO_2 film is kinetically restricted to Li_xTiO_2 below x = 0.6 since the dimension is larger than ~100 nm(*13*). However, the thickness if TiO2 film (255 nm) was chosen as close as the thermal penetration depths $d_T = \sqrt{\Lambda / (f \pi C)}$ to secure the sensitivity of TDTR at f = 11 MHz.

TiO_2 showed C_{33} increased from 164 to 249 GPa, similar to calculated values of 185 and 276 GPa of α-TiO_2 and γ-$LiTiO_2$(*24*). Likewise, V_2O_5 showed C_{33} increased from 23 to 28 GPa. Although elastic moduli were increased with respect to x, we observed thermal conductivity changes of Li_xTiO_2 from 7.7 W m^{-1} K^{-1} (x = 0) to 4.4 W m^{-1} K^{-1} (x = 0.34) after the first lithiation, followed by a recovery to 8.0 W m^{-1} K^{-1} (x = 0.1) after the subsequent delithiation and $Li_xV_2O_5$ from 7.22 W m^{-1} K^{-1} (x = 0) to 4.78 W m^{-1} K^{-1} (x = 2) and 5.64 W m^{-1} K^{-1} (x = 0.11) after the first lithiation/delithiation. As TiO_2 and V_2O_5 showed thermal conductivity recovery after the delithiation, we assume that the intercalation materials are structurally-stable during the electrochemical lithiation/delithiation processes. The potential plateau of TiO_2 and V_2O_5 electrode (Figure 5.12B and D) are stable, which is consistent with the small volume changes and stable crystal structures after cycling.

Figure 5.13 shows thermal conductivity and electrochemical potential changes of TiO_2 and V_2O_5 during galvanostatic charge/discharge cycles. Li_xTiO_2 showed a monotonic decrease in thermal conductivity with respect to x up to x = 0.34. The reason for the thermal conductivity decrease is not clear. The phase transition from α-TiO_2 to β-Li_xTiO_2 are assisted by a charge transfer reaction between the host and guest. The insertion of Li^+ ions to TiO_2 results in changes of phonon dispersion(*25*) as well as an electronic band structure transition between Li(2s) and of Ti($3d_{yz}$) orbitals (*26*). As Li(2s) electrons fill the $3d_{yz}$ orbitals of TiO_2 the electron density of state grows in number at E_F(*27*). The resulting increase in the electric conductivity would increase the electrical contribution to thermal conductivity (Λ_e). The increase in speed of sound, which is related to the lattice thermal conductivity (Λ_L), is contradicting with the observed thermal conductivity decrease of Li_xTiO_2.

On the other hand, $Li_xV_2O_5$ showed thermal conductivity decrease from x = 0 to x = 0.5 and increase from x = 0.5 to x = 1, which remained almost the same up to x =2 at around 4.8 W m^{-1} K^{-1}. This "thermal conductivity valley" can be contributed to the series of phase transitions where ε phase ($0.35<x< 0.7$) might have lower thermal conductivity than other phases including α ($x< 0.1$), δ ($x<1$) and γ ($1<x\leq2$)(*14, 15*). We further confirmed the existence of the thermal conductivity valley of V_2O_5 by subjecting it to cycling between x = 0 and x = 1 (2^{nd} cycle, Figure 5.13B). During five charge/discharge cycles, intercalating Li_xTiO_2 and $Li_xV_2O_5$ showed a reversible thermal conductivity switching $r \approx 1.6–1.8$ up to x 0.5, respectively. Further increase in x ($x > 1$) did not induce the thermal conductivity change of V_2O_5. We suspect that this thermal conductivity valley ($0<x<1$) might also present in Li_xTiO_2. However, we were not able to test this hypothesis since further insertion of Li^+ ions to Li_xTiO_2 ($x > 0.6$) can be achieved by nanostructuring (<~10 nm) (*27, 28*).

Figure 5.14 shows specific cycling performance of TiO_2 and V_2O_5 with the charge/discharge capacities of 40–50 mAh g^{-1}, which is much lower than the theoretical capacities of TiO_2 (165 mAh g^{-1}) and V_2O_5 (260 mAh g^{-1}). We attribute the reduction of capacity to the poor kinetics of Li^+ ions diffusion in bulk film at high C-rates (1–2C), which were chosen for *in situ* TDTR measurements. Note that we pre-cycled 255-nm TiO_2 at the current density of 75 mA g^{-1} with the initial discharge capacity of 110 mAh g^{-1}. Then, TiO_2 showed capacity fading from 73 to 52 mAh g^{-1} (up to 6 cycles) at the current density of 50 mAh g^{-1} for five cycles. These values are close to 300-nm TiO_2 microspheres with the initial discharge capacity of 110 mAh g^{-1} and 50 mAh g^{-1} (up to 20 cycles) (*29*).

5.6 THERMAL CONDUCTIVITY AND ELASTIC MODULUS CHANGES OF ANTIMONY

To measure the thermal conductivity switching of Sb, we used specially designed all-solid cells that are compatible with TDTR measurements of electrode materials with large volume expansion. For this setup, we Li_2S:P_2S_5 solid electrolyte was used to replace the conventional liquid electrolyte. The Li metal counter electrode was replaced with the In-Li alloy counter electrode to suppresses the dendrite formation on the surface (*30*). This cell was made to keep pressurizing the electrode by Ti metal rods. Detail of the solid electrochemical cell is described in Chapter 2.5.

Figure 5.15 shows TDTR data of as-prepared (Sb) and lithiated (Li_3Sb) Sb/Au/Al/SiO_2/sapphire sample in the solid electrolyte cell. We measured Λ = 18 W m^{-1} K^{-1} for as-prepared Sb, mostly from the electric contribution to thermal conductivity Λ_e = 12 W m^{-1} K^{-1} calculated by Wiedemann Franz law:

$$\Lambda_e = \sigma L T \tag{5.5}$$

where σ is the electric conductivity of the Sb film measured by four probes, L is the Lorentz number (2.44×10^{-8} W Ω K^{-2}). This large electrical contribution is originated from the overlap of valence and conduction bands at E_F. The estimated lattice thermal conductivity of Sb $\Lambda_L = \Lambda - \Lambda_e$ = 6 W m^{-1} K^{-1}. At the fully lithiated state, Li_3Sb, we measured thermal conductivity of 0.6 W m^{-1} K^{-1}, which is close to Λ_{min} = 0.43 W m^{-1} K^{-1}. This dramatic thermal conductivity contrast $r \approx 30$ can be attributed to the loss of crystallinity and electric conductivity during the phase transition between semimetal (Sb) and semiconductor (Li_3Sb, E_g = 0.7 eV) (*31, 32*). The lattice thermal conductivity is also dramatically suppressed to 2.2 W m^{-1} K^{-1} at the crystalline Li_3Sb (first principles) (*33*) compared with the lattice thermal conductivity of crystalline Sb (first principles)(*34*). A similar degree of thermal conductivity has been reported for semiconducting Sb compounds: 0.35 and 0.23 W m^{-1} K^{-1} for crystalline and amorphous Sb_2Te_3(*35*) and 0.65 W m^{-1} K^{-1} for Zn_4Sb_3(*36*) due to i) the loose coupling of Zn and Sb oscillating different frequencies and ii) the interstitials (*37*).

We observed that this dramatic thermal conductivity decrease is associated with the irreversible loss of C_{11}. Figure 5.16 shows picosecond acoustic data and thermal conductivity of Li_xSb with respect to the Li^+ ion contents x. x was calculated by the theoretical capacity and volume of the Sb film. Note that we used the classical heat capacity $C = 3Nk_B$ = 2.36 J $cm^{-3}K^{-1}$ to calculate thermal conductivity of Li_3Sb (Θ_{Li_3Sb} = 171 K) where both Sb and Li match well with the classical $3Nk_B$ = 1.38 J cm^{-3} K^{-1} and 1.9 J cm^{-3} K^{-1}, respectively. This large heat capacity transition ΔC = 70% compared with ΔC < 10% of Fe_2O_3, NiO, TiO_2 and V_2O_5 might add uncertainty to the measured thermal conductivity as TDTR measures thermal effusivity,

$e = \sqrt{\Lambda C}$, of electrode materials. Pulverization of Sb with the formation of void and SEI could lead to the underestimation of thermal conductivity. During the lithiation process, the position of picosecond acoustic peak changed from 247 ps (x = 0) to 344 ps (x = 1), which returned to 239 ps after the delithiation. The first two peaks were converted to C_{11} = 88 and 59 GPa, considering the theoretical volume expansion from Sb to LiSb. However, we were not able to calculate C_{11} at fully discharged and charged states as the thicknesses of fully discharged Li_3Sb and charged Sb films could not be determined by SEM due to the severe structural degradation and mixing with SEI.

Figure 5.17A shows voltage and thermal conductivity of Sb during galvanostatic charge/discharge cycles. Compared with the irreversible thermal conductivity loss of conversion electrode materials at the first discharge, we observed a gradual thermal conductivity loss of Sb (delithiated) from 18 to 3.3 W m^{-1} K^{-1} for five cycles. This thermal conductivity reduction could be attributed to the pulverization of Sb film (200 nm) during repetitive charge/discharge cycling. We expect decreases in Λ_L as the majority of phonons carrying heat in Sb and Li_3Sb has a mean free path (MFP) between 10 nm to 100 nm (*33, 34*). Furthermore, pulverization of Sb leads to a decrease in electric conductivity due to the formation, breakage and growth of SEI on newly exposed, pulverized Sb particles during cycling(*8, 38*). Because the pulverization of Sb introduces new active Sb surface, we observed an increase in the discharge capacity of Sb and a continuous shift of potential hysteresis as cycle goes (Figure 5.17B-C).

We attributed this capacity loss with structural degradation to the gradual loss of thermal conductivity. To prevent the SEI growth and pulverization Sb film, we limited the discharge capacity up to x = 1.38 (250 mAh g^{-1})—the irreversible discharge capacity of the fully lithiated

Li_3Sb film at the first discharge. Figure 5.18A shows voltage and thermal conductivity of Li_xSb during galvanostatic charge/discharge cycles with a limited discharge capacity up to $x = 1.38$. As shown in Figure 5.18B-C, we observed irreversible discharge capacities of 190 and 109 mAh g^{-1} during the first and the second discharges. Interestingly, thermal conductivity of Sb remained above 10 W m^{-1} K^{-1} during discharge reactions attributable to these irreversible capacities at the first and second cycles. We attribute these irreversible discharge capacities to the stable SEI film formation on the surface of Sb. The sum of irreversible capacity at the first and second discharges (299 mAh g^{-1}) is also comparable with the irreversible discharge capacity of fully lithiated Li_3Sb at the first discharge.

With limiting discharge capacity, the volume expansion of Sb is also limited, thereby suppressing the severe pulverization of Sb with the continuous growth of SEI. Thus, we observed a stable thermal switching of Sb between 8.5–10.5 W m^{-1} K^{-1} (Sb) and 4.5–6 W m^{-1} K^{-1} (Li_xSb) for five cycles with much improved coulombic efficiencies (>90%).

5.7 SUMMARY

In summary, we explored the thermal, structural, mechanical and electrochemical properties of five electrode materials (Fe_2O_3, NiO, TiO_2, V_2O_5, Sb) with respect to Li^+ ion content. We performed a series of *in situ* TDTR and picosecond acoustic measurements to relate the thermal conductivity changes with speed of sound changes of the electrode materials. We observe contrasting behaviors between conversion (NiO, Fe_2O_3), intercalation (V_2O_5 and TiO_2) and alloying (Sb) electrode materials. Conversion electrodes become thermally static materials preceded by an irreversible thermal conductivity loss of a factor of two to five during the first discharge. Intercalation materials showed reversible thermal conductivity

switching (up to a factor of 2) and elastic modulus switching with varying Li^+ contents. The alloying Sb electrode showed the largest thermal conductivity switching by a factor of 20–30 at the first few cycles, which gradually became thermal insulator regardless of Li^+ ion contents. With a limiting discharge capacity, we were able to keep the thermal conductivity switching of Sb up to 5 cycles. This study emphasizes the role of structural and electrochemical stability of electrode materials in their thermal transport properties.

5.8 FIGURES

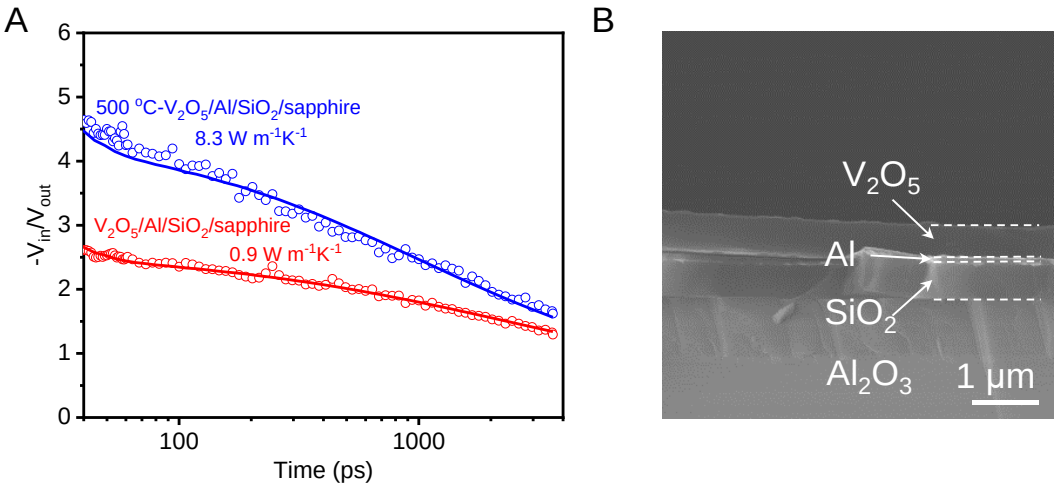

Figure 5.1. Effect of heat treatment on thermal conductivity of V_2O_5. **A.** The measured (open circles) and fitted (solid lines) TDTR curves of V_2O_5/Al/SiO_2/sapphire sample before and after the heat treatment at 500 °C at air. **B.** the cross-sectional SEM image of V_2O_5/Al/SiO_2/sapphire sample (after the heat treatment).

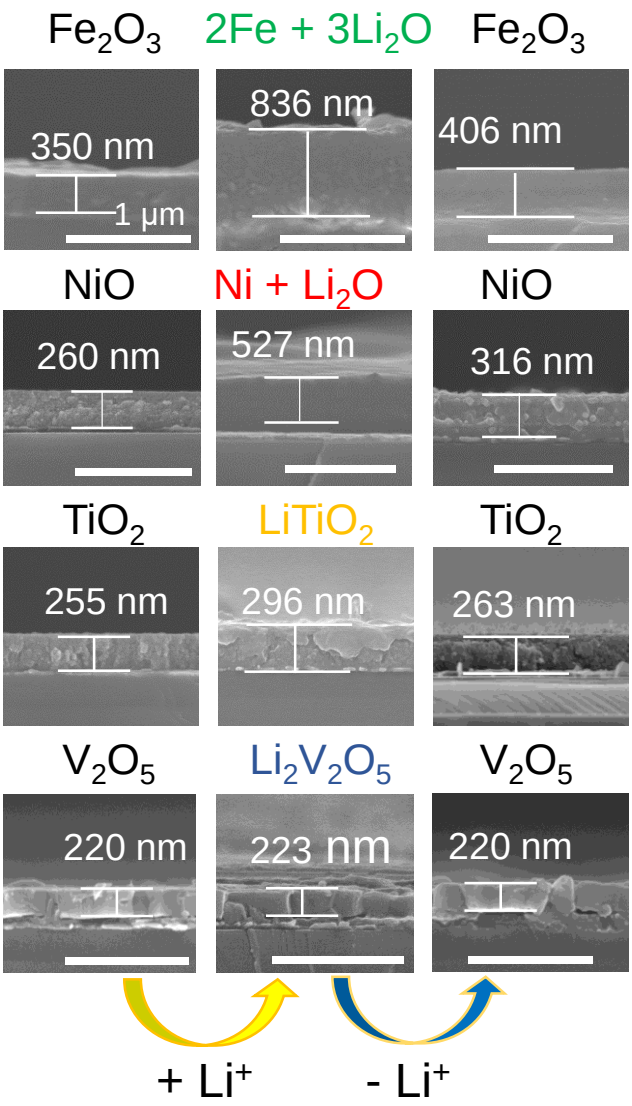

Figure 5.2. Cross-sectional SEM images of four electrode materials before and after lithiation/delithiation. The scale bar is 1 µm.

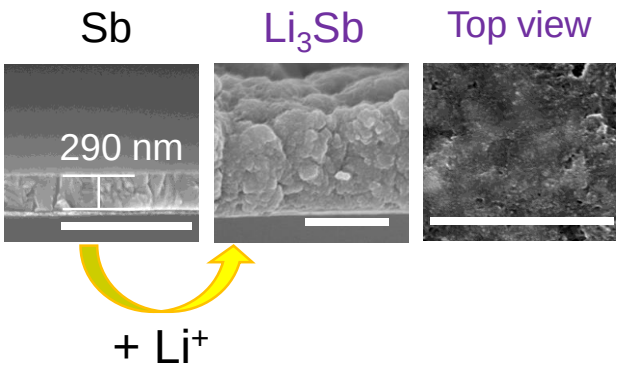

Figure 5.3. SEM images of the cross sections and the top surface of Sb/Al/SiO_2/sapphire samples before and after the first lithiation. The scale bar is 1 μm.

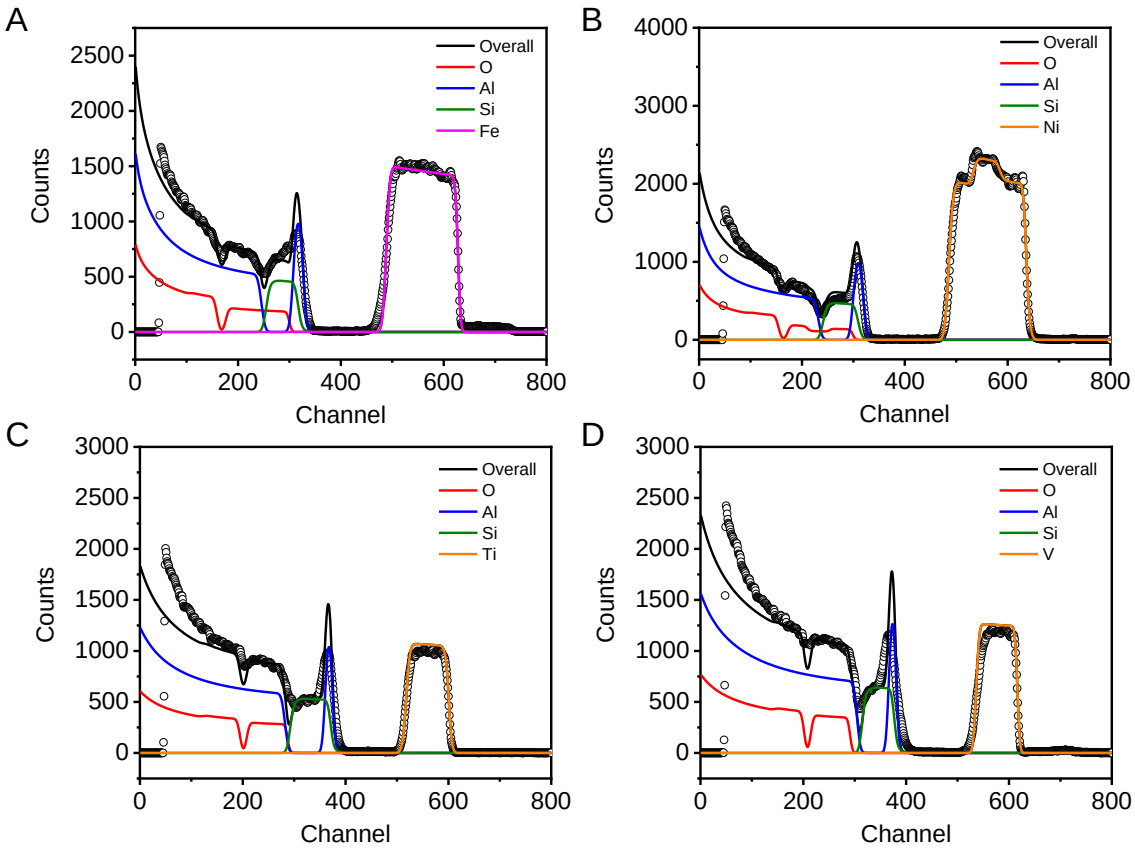

Figure 5.4. RBS data of conversion and intercalation electrode materials on Al/SiO_2/sapphire substrates after the heat treatment. **A.** Conversion Fe_2O_3; **B.** Conversion NiO; **C.** Intercalating TiO_2; and **D.** Intercalating V_2O_5.

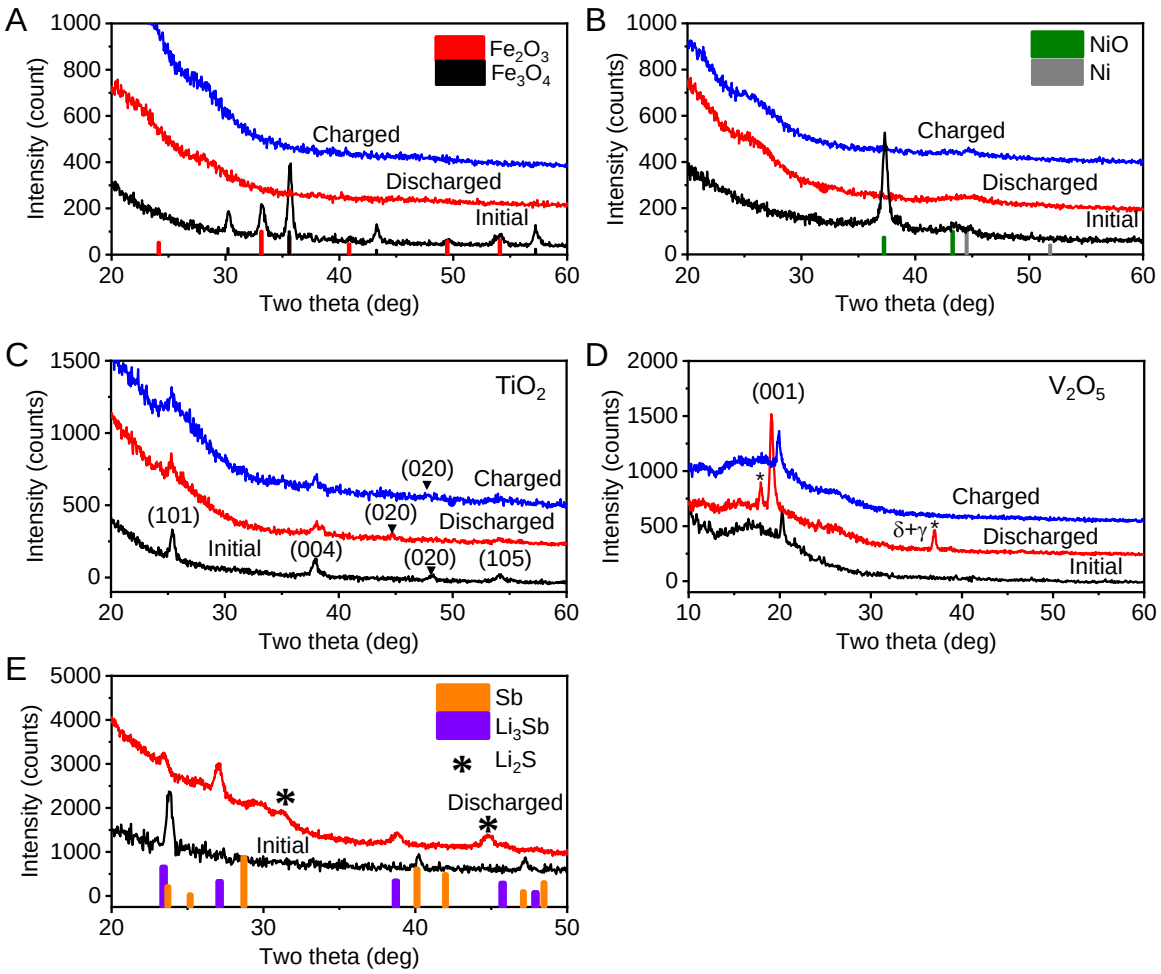

Figure 5.5. XRD data of five electrode materials before and after lithiation/delithiation: **A.** Conversion Fe_2O_3; **B.** Conversion NiO: **C.** Intercalating TiO_2; **D.** Intercalating V_2O_5; and **E.** Alloying Sb.

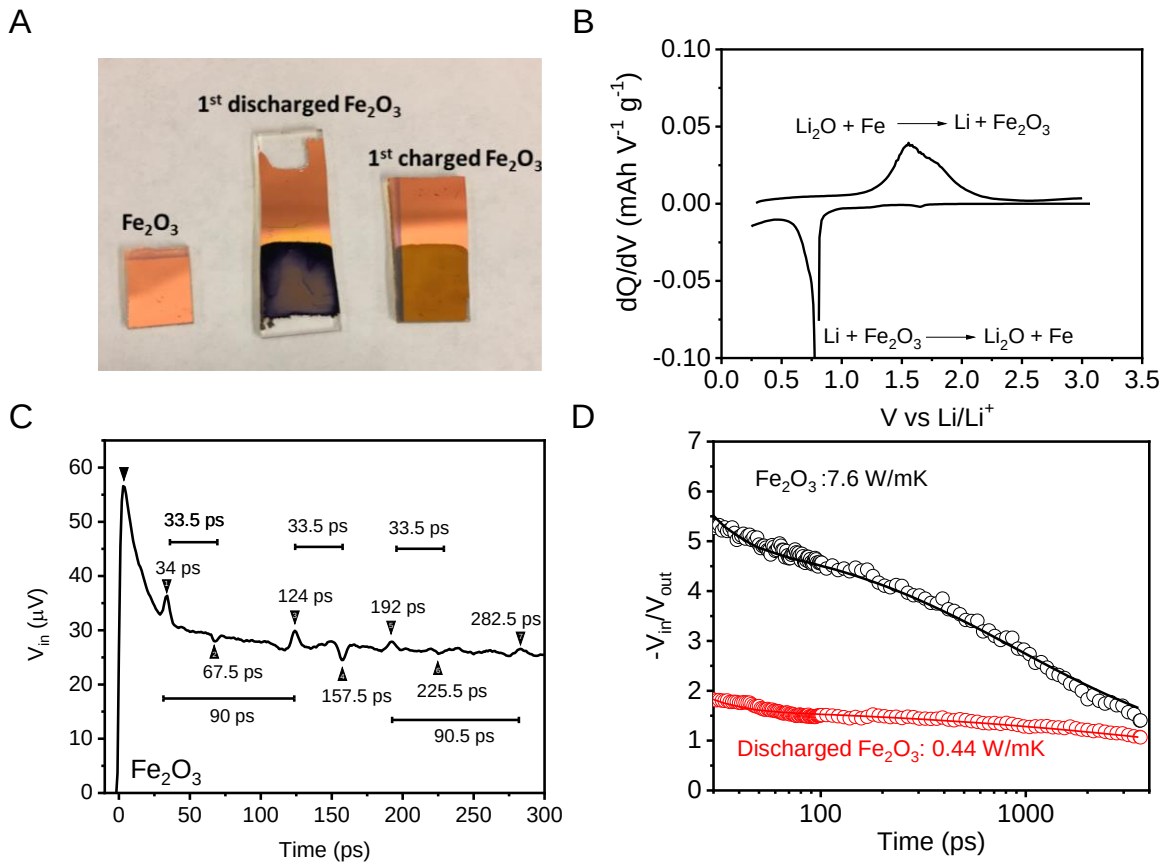

Figure 5.6. *Ex situ* TDTR analysis of conversion Fe_2O_3 electrode material **A.** Photographs of as-prepared, discharged and charged Fe_2O_3 films on Au/SiO_2 substrates. **B.** Differential capacity analysis for Fe_2O_3. **C.** Picosecond acoustic data of the Al (107 nm)/Fe_2O_3 (335 nm)/Au (60 nm)/SiO_2 sample. **D.** Measured and fitted *ex situ* TDTR data of Al (107 nm)/Fe_2O_3 (335 nm)/Au (60 nm)/SiO_2 before and after the first discharge.

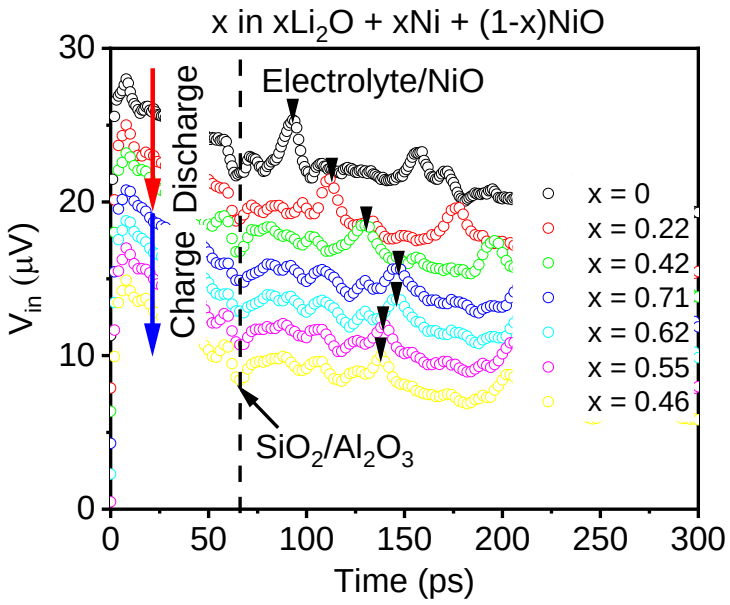

Figure 5.7. *In situ* picosecond acoustic analysis of the conversion NiO electrode. Measured in-phase TDTR signal of NiO/Al/SiO_2/sapphire substrate in the liquid electrolyte cell under electrochemical reaction with Li^+ ions. The Li^+ ion content, *x*, was calculated from the volume and the theoretical capacity of NiO (718 mAh g^{-1}).

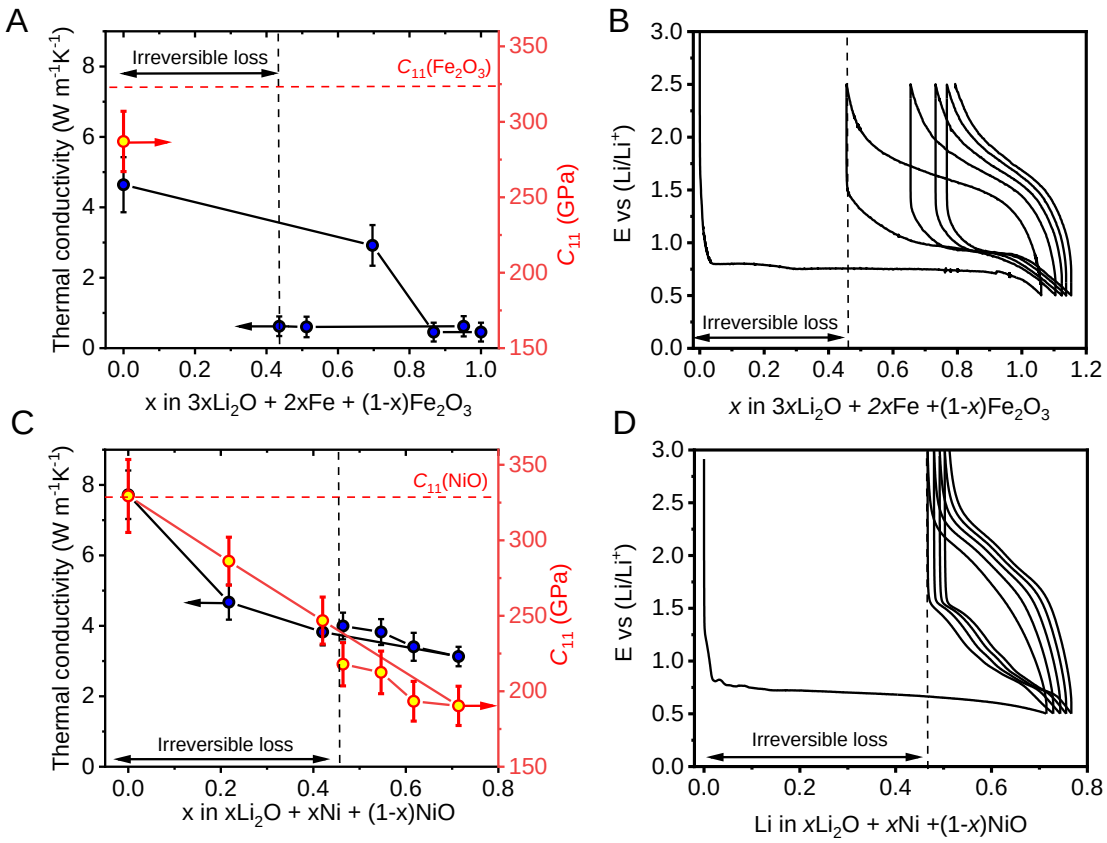

Figure 5.8. Thermal conductivity and elastic modulus of conversion Fe_2O_3 and NiO electrode materials with respect to *x*. **A.** Thermal conductivity and calculated C_{11} of Fe_2O_3 with varying *x* during lithiation/delithiation. **B.** Potential hysteresis of Fe_2O_3 during five galvanostatic charge/discharge cycles at the current of 300 mA g^{-1} with the voltage window from 2.5 to 0.5 V vs. Li/Li$^+$. **C.** Thermal conductivity and calculated C_{11} of NiO with respect to *x* during lithiation/delithiation. **D.** Potential hysteresis of NiO during galvanostatic charge/discharge cycling (5 cycles) at the current of 182 mA g^{-1} from 3.0 to 0.5 V vs. Li/Li$^+$. Black dashed line indicates the irreversible capacity loss at the first discharge. Red dashed line indicates the theoretical C_{11}.

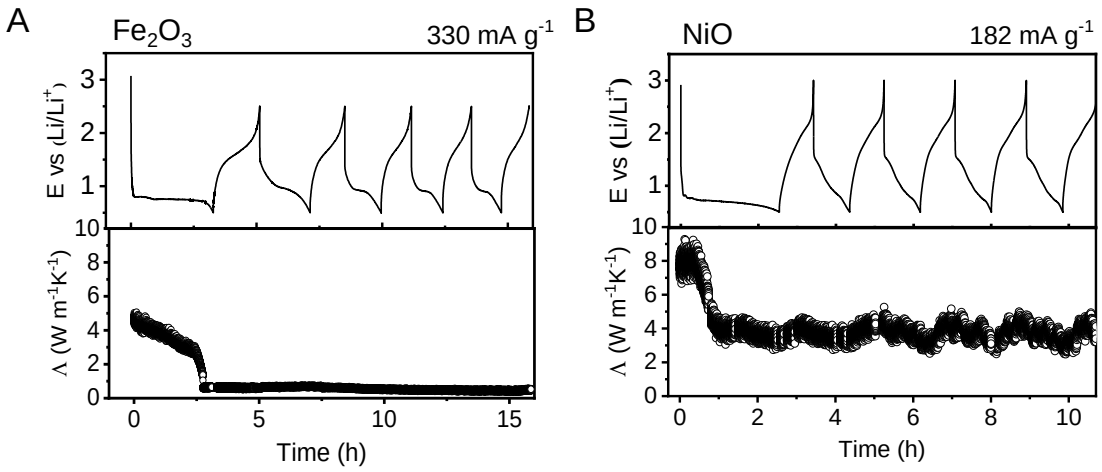

Figure 5.9. *In situ* TDTR analysis of Fe_2O_3 and NiO electrode materials. **A.** Voltage (up) and thermal conductivity (down) of Fe_2O_3 during five galvanostatic charge/discharge cycling at the current density of 300 mA g^{-1} with the voltage window from 2.5 to 0.5 V vs. Li/Li^+. **B.** Voltage (up) and thermal conductivity (down) of Fe_2O_3 during galvanostatic charge/discharge cycling (5 cycles) at the current density of 182 mA g^{-1} with the voltage window 3.0 to 0.5 V vs. Li/Li^+. The current densities were calculated based on the weight and volume of each electrode material.

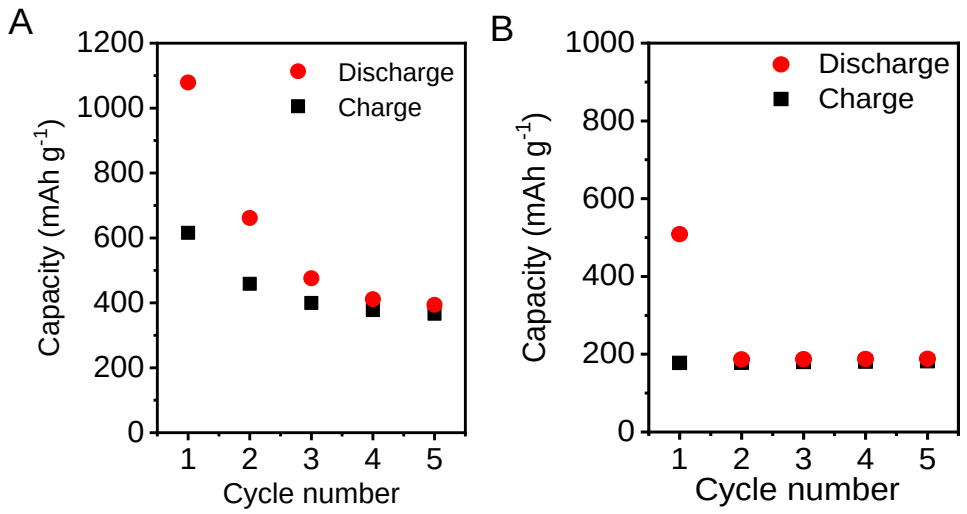

Figure 5.10. Cycling performance of Fe_2O_3 and NiO. Electrochemical charge/discharge capacity of **A.** Fe_2O_3 and **B.** NiO films on Al/SiO_2/sapphire substrates during *in situ* TDTR measurements (Figure 5.9). Specific capacity was calculated based on weight and volume of each electrode material.

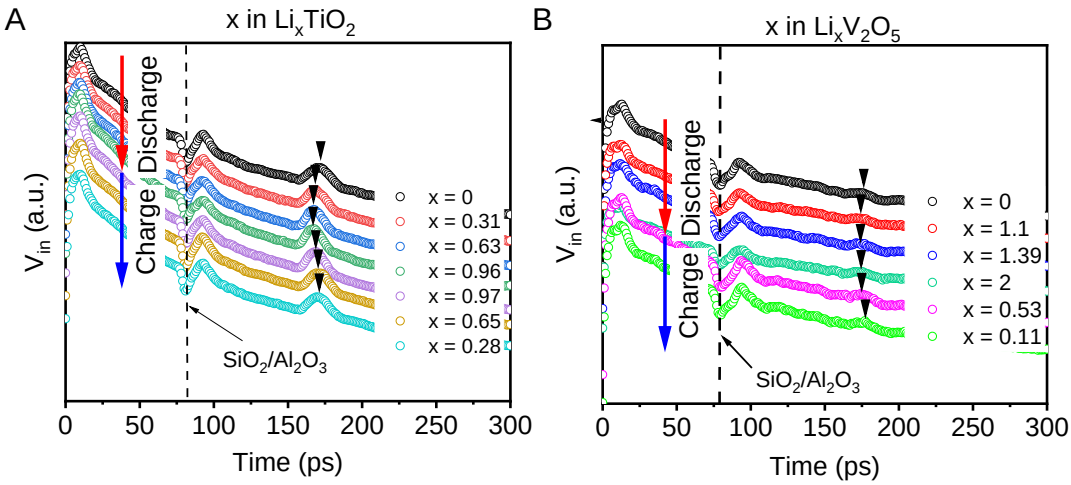

Figure 5.11. *In situ* picosecond acoustic analysis of the intercalating TiO_2 and V_2O_5. with varying *x*. **A.** Measured in-phase TDTR signal of TiO_2/Al/SiO_2/sapphire substrate in the liquid electrolyte cell under electrochemical reaction with Li^+ ions. *x* was calculated from the volume and the theoretical capacity of anatase α-TiO_2 (165 mAh g^{-1}). **B.** Measured in-phase TDTR signal of V_2O_5/Al/SiO_2/sapphire substrate in the liquid electrolyte cell under electrochemical reaction with Li^+ ions. *x* was calculated from the potential plateaus of V_2O_5.

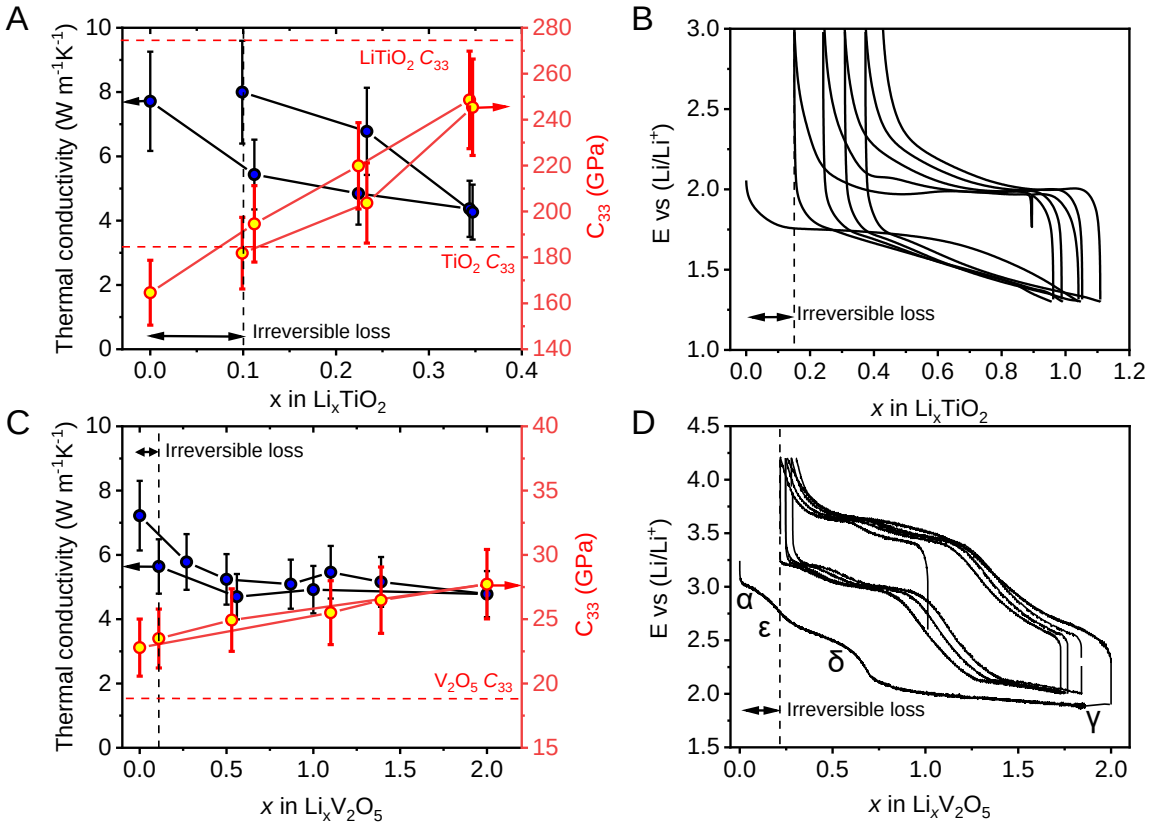

Figure 5.12. Thermal conductivity and elastic modulus of intercalating TiO_2 and V_2O_5 electrode materials with respect to *x*. **A.** Thermal conductivity and calculated C_{33} of TiO_2 with respect to *x* during lithiation/delithiation. **B.** Potential hysteresis of TiO_2 during five galvanostatic charge/discharge cycles at the current of 50 mA g^{-1} with the voltage window from 3.0 to 1.3 V vs. Li/Li^+. **C.** Thermal conductivity and calculated C_{33} of V_2O_5 with respect to *x* during lithiation/delithiation. **D.** Potential hysteresis of V_2O_5 during five galvanostatic charge/discharge cycles at the current of 100 mA g^{-1} with the voltage window from 4.2 to 1.9–2.6 V vs. Li/Li^+. V_2O_5 was activated up to $x = 2$ at the first discharge. For the following cycles, V_2O_5 was discharged to 2.6 (2nd cycle, $x = 1$) and 2.0 V (up to 5th cycle, $x \leq 2$) vs. Li/Li^+. Black dashed line indicates the irreversible capacity loss at the first discharge. Red dashed line indicates the theoretical C_{33}.

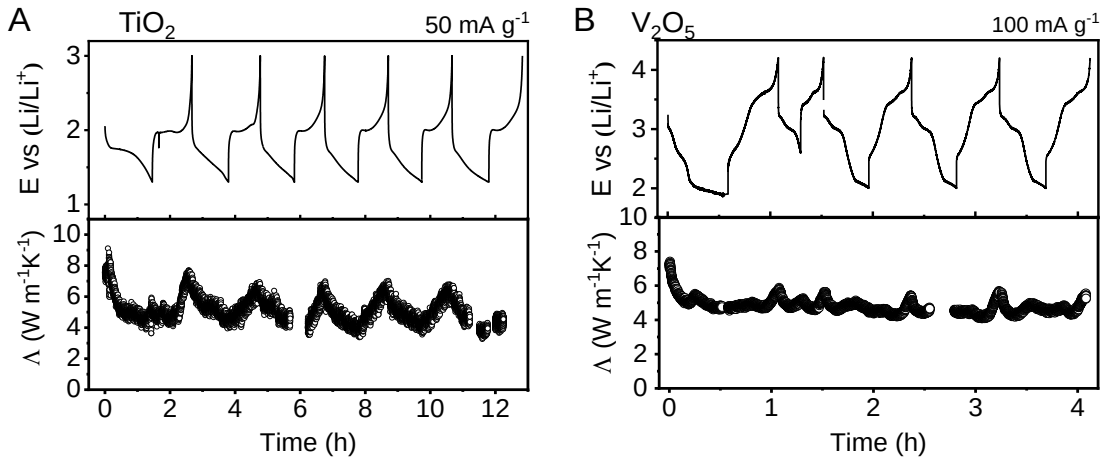

Figure 5.13. *In situ* TDTR analysis of intercalating TiO_2 and V_2O_5 electrode materials. **A.** Voltage (up) and thermal conductivity (down) of TiO_2 during five galvanostatic charge/discharge cycles at the current density of 50 mA g^{-1} with the voltage window from 3.0 to 1.3 V vs. Li/Li^+. **B.** Voltage (up) and thermal conductivity (down) of V_2O_5 during five galvanostatic charge/discharge cycles at the current density of 100 mA g^{-1} with the voltage window from 4.0 to 1.9 (1^{st}, $x = 2$), 2.6 (2^{nd}, $x \leq 1$) and 2.0 (3^{rd} to 5^{th}, ≤ 2) V vs. Li/Li^+. Current densities were calculated based on the weight and volume of each electrode material.

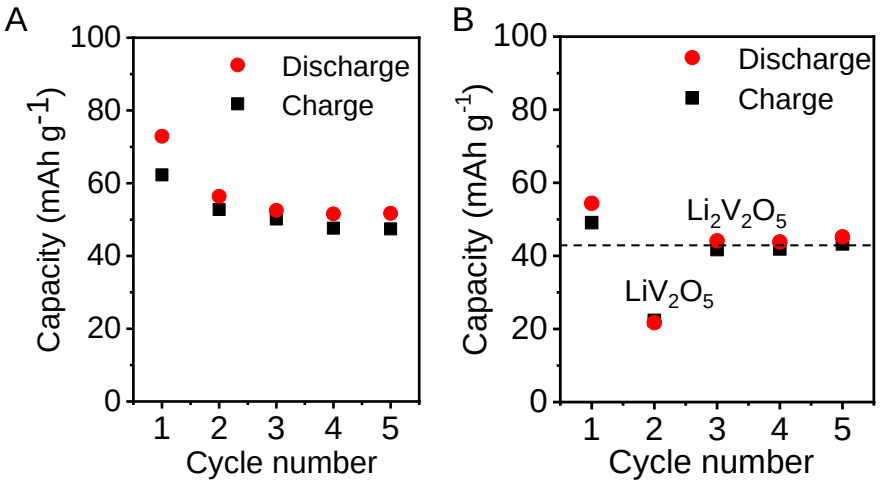

Figure 5.14. Cycling performance of TiO_2 and V_2O_5. Electrochemical charge/discharge capacity of **A.** Li_xTiO_2 and **B.** $Li_xV_2O_5$ films on Al/SiO_2/sapphire substrates up to x = 1 and x = 2 during *in situ* TDTR measurements (Figure 5.13). Note that the second cycle of $Li_xV_2O_5$ was performed at $x \leq 1$ and the rest of cycles were performed at ≤ 2 for $Li_xV_2O_5$. Specific capacities were calculated based on the weight and volume of each electrode material.

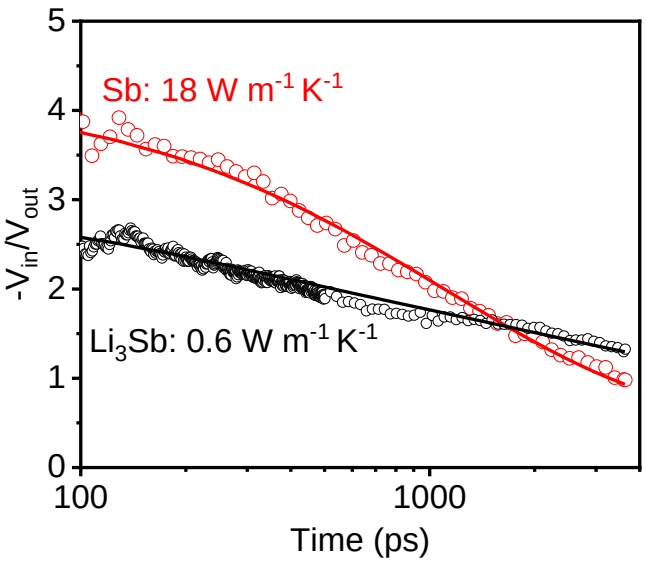

Figure 5.15. Measured and fitted TDTR data of as-prepared and discharged Sb/Au/Al/SiO_2/sapphire.

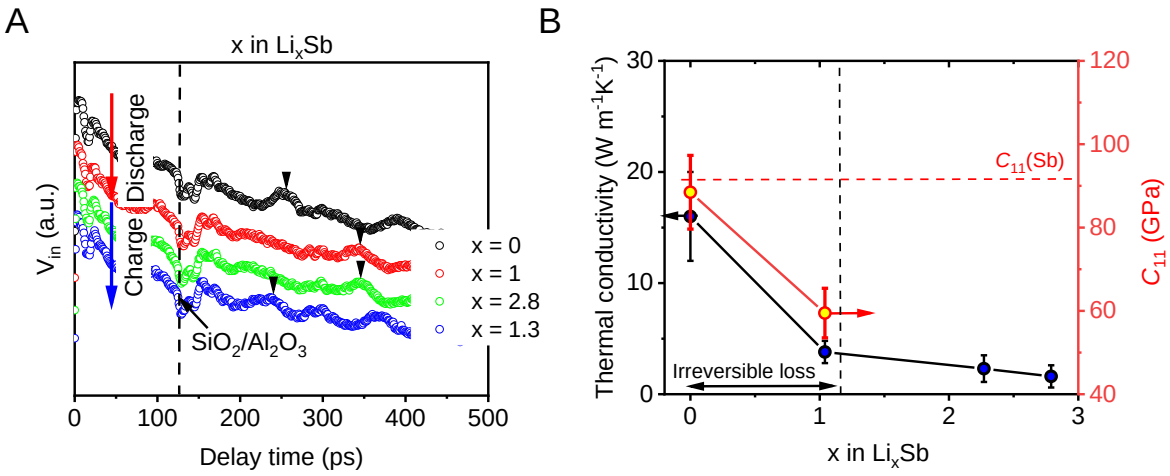

Figure 5.16. Thermal conductivity and elastic modulus of the alloying Sb electrode material with respect to *x*. **A.** Measured in-phase TDTR signal of Sb/Au/Al/SiO_2/sapphire substrate in the solid electrolyte cell under electrochemical reaction with Li^+ ions. *x* was calculated from the volume and the theoretical capacity of Sb (660 mAh g^{-1}). **B.** Thermal conductivity and calculated C_{11} modulus of Sb with respect to *x* during electrochemical cycling with Li^+ ions. Black dashed line indicates the irreversible loss of capacity at the first discharge. Red dashed line indicates the theoretical C_{11} of Sb.

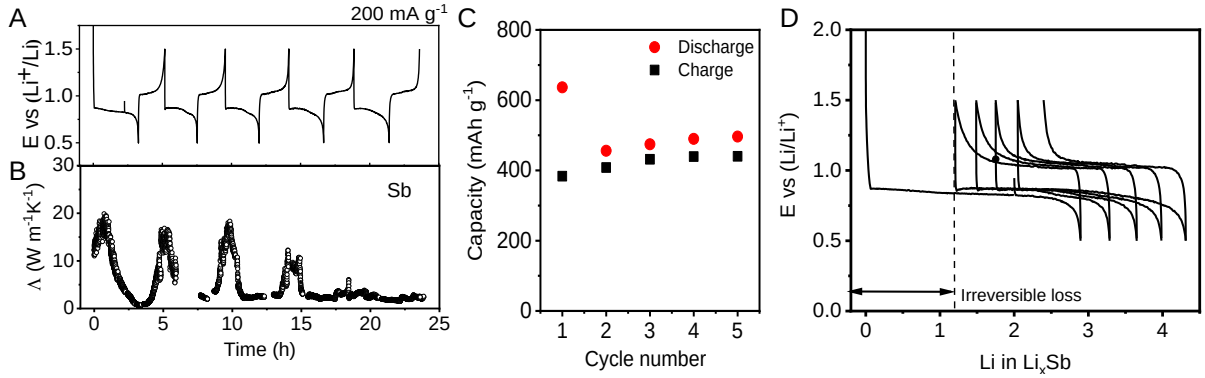

Figure 5.17. *In situ* TDTR analysis of the alloying Sb electrode material. **A.** Voltage (up) and thermal conductivity (down) of Sb during five galvanostatic charge/discharge cycles. **B.** Electrochemical charge/discharge capacity and **C.** potential hysteresis of Sb during five galvanostatic charge/discharge cycles at the current of 200 mA g^{-1} with the voltage window from 1.5 to 0.5 V vs. Li/Li^+.

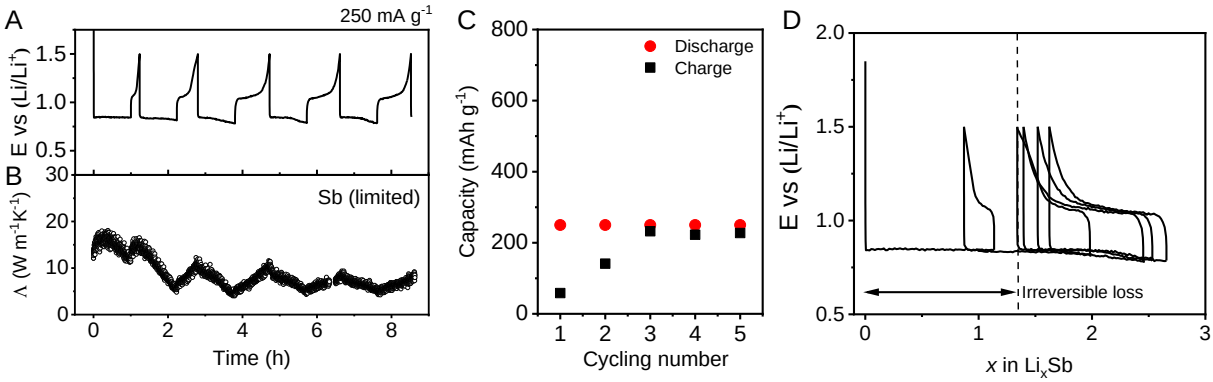

Figure 5.18. *In situ* TDTR analysis of the alloying Sb electrode material with a limited discharge capacity ($x \leq 1.38$, 250 mAh g^{-1}). **A.** Voltage (up) and thermal conductivity (down) of Sb during five galvanostatic charge/discharge cycles. The discharge capacity is limited to the 250 mAh g^{-1}. Sb was charged up to 1.5 V vs. Li/Li^+ at the current density of 250 mA g^{-1}. **B.** Electrochemical charge/discharge capacity and **C.** potential hysteresis of Sb five galvanostatic charge/discharge cycles with a limited discharge capacity.

5.9 REFERENCES

1. H. D. Yoo, E. Markevich, G. Salitra, D. Sharon, D. Aurbach, On the challenge of developing advanced technologies for electrochemical energy storage and conversion. *Mater Today* **17**, 110-121 (2014).
2. V. Etacheri, R. Marom, R. Elazari, G. Salitra, D. Aurbach, Challenges in the development of advanced Li-ion batteries: a review. *Energ Environ Sci* **4**, 3243-3262 (2011).
3. N. Nitta, F. X. Wu, J. T. Lee, G. Yushin, Li-ion battery materials: present and future. *Mater Today* **18**, 252-264 (2015).
4. W. J. Zhang, A review of the electrochemical performance of alloy anodes for lithium-ion batteries. *J Power Sources* **196**, 13-24 (2011).
5. M. Abdel-Rahman *et al.*, Temperature coefficient of resistance and thermal conductivity of Vanadium oxide 'Big Mac' sandwich structure. *Infrared Phys Techn* **71**, 127-130 (2015).
6. A. Paul, A. A. Kodentsov, G. de With, F. J. J. van Loo, Formation of AB2-intermetallics by diffusion in the Au-Sb-Bi system. *Intermetallics* **11**, 1195-1203 (2003).
7. H. Liu, C. P. Grey, Influence of particle size, cycling rate and temperature on the lithiation process of anatase TiO_2. *J Mater Chem A* **4**, 6433-6446 (2016).
8. J. Shin, W. H. Ryu, K. S. Park, I. D. Kim, Morphological Evolution of Carbon Nanofibers Encapsulating SnCo Alloys and Its Effect on Growth of the Solid Electrolyte Interphase Layer. *Acs Nano* **7**, 7330-7341 (2013).
9. V. Aravindan, Y. S. Lee, S. Madhavi, Research Progress on Negative Electrodes for Practical Li-Ion Batteries: Beyond Carbonaceous Anodes. *Adv Energy Mater* **5**, 1402225 (2015).
10. S. H. Yu, S. H. Lee, D. J. Lee, Y. E. Sung, T. Hyeon, Conversion Reaction-Based Oxide Nanomaterials for Lithium Ion Battery Anodes. *Small* **12**, 2146-2172 (2016).
11. X. D. Yan *et al.*, TiO_2 Nanomaterials as Anode Materials for Lithium-Ion Rechargeable Batteries. *Energy Technol-Ger* **3**, 801-814 (2015).

12. M. Wagemaker, G. J. Kearley, A. A. van Well, H. Mutka, F. M. Mulder, Multiple Li positions inside oxygen octahedra in lithiated TiO_2 anatase. *J Am Chem Soc* **125**, 840-848 (2003).
13. M. Wagemaker, W. J. H. Borghols, F. M. Mulder, Large impact of particle size on insertion reactions. A case for anatase Li_xTiO_2. *J Am Chem Soc* **129**, 4323-4327 (2007).
14. C. Delmas, H. Cognacauradou, J. M. Cocciantelli, M. Menetrier, J. P. Doumerc, The $Li_xV_2O_5$ System - an Overview of the Structure Modifications Induced by the Lithium Intercalation. *Solid State Ionics* **69**, 257-264 (1994).
15. K. Palanisamy, J. H. Um, M. Jeong, W. S. Yoon, Porous V_2O_5/RGO/CNT hierarchical architecture as a cathode material: Emphasis on the contribution of surface lithium storage. *Sci Rep-Uk* **6**, 31275 (2016).
16. S. Lany, Semiconducting transition metal oxides. *J Phys-Condens Mat* **27**, 283203 (2015).
17. D. G. Cahill, S. K. Watson, R. O. Pohl, Lower Limit to the Thermal-Conductivity of Disordered Crystals. *Phys Rev B* **46**, 6131-6140 (1992).
18. N. Spinner, L. C. Zhang, W. E. Mustain, Investigation of metal oxide anode degradation in lithium-ion batteries via identical-location TEM. *J Mater Chem A* **2**, 1627-1630 (2014).
19. J. Cho *et al.*, Electrochemically tunable thermal conductivity of lithium cobalt oxide. *Nat Commun* **5**, 4035 (2014).
20. G. H. Zhu *et al.*, Tuning thermal conductivity in molybdenum disulfide by electrochemical intercalation. *Nat Commun* **7**, 13211 (2016).
21. J. S. Kang, M. Ke, Y. J. Hu, Ionic Intercalation in Two-Dimensional van der Waals Materials: In Situ Characterization and Electrochemical Control of the Anisotropic Thermal Conductivity of Black Phosphorus. *Nano Lett* **17**, 1431-1438 (2017).
22. L. Nanai, W. Volken, Sound Speed Anisotropy of V_2O_5 Single-Crystals Determined by Laser Generated Acoustic-Waves. *Solid State Commun* **70**, 223-224 (1989).
23. E. Strelcov, J. Cothren, D. Leonard, A. Y. Borisevich, A. Kolmakov, In situ SEM study of lithium intercalation in individual V_2O_5 nanowires. *Nanoscale* **7**, 3022-3027 (2015).
24. M. de Jong *et al.*, Charting the complete elastic properties of inorganic crystalline compounds. *Sci Data* **2**, 150009 (2015).

25. A. Sood *et al.*, An electrochemical thermal transistor. *Nat Commun* **9**, 4510 (2018).
26. G. Nuspl, K. Yoshizawa, T. Yamabe, Lithium intercalation in TiO_2 modifications. *J Mater Chem* **7**, 2529-2536 (1997).
27. W. J. H. Borghols *et al.*, The electronic structure and ionic diffusion of nanoscale $LiTiO_2$ anatase. *Phys Chem Chem Phys* **11**, 5742-5748 (2009).
28. U. Lafont, D. Carta, G. Mountjoy, A. V. Chadwick, E. M. Kelder, In Situ Structural Changes upon Electrochemical Lithium Insertion in Nanosized Anatalse TiO_2. *J Phys Chem C* **114**, 1372-1378 (2010).
29. C. H. Jiang, I. Honma, T. Kudo, H. S. Zhou, Nanocrystalline rutile TiO2 electrode for high-capacity and high-rate lithium storage. *Electrochem Solid St* **10**, A127-A129 (2007).
30. X. H. Wu, M. El Kazzi, C. Villevieille, Surface and morphological investigation of the electrode/electrolyte properties in an all-solid-state battery using a Li_2S-P_2S_5 solid electrolyte. *J Electroceram* **38**, 207-214 (2017).
31. S. Y. Wang *et al.*, Anisotropic Multicenter Bonding and High Thermoelectric Performance in Electron-Poor CdSb. *Chem Mater* **27**, 1071-1081 (2015).
32. A. Bath, J. G. Gasser, R. Kleim, Electrical-Resistivity of Zn-Sb and Cd-Sb Liquid Alloys in the Compound-Forming Concentration Range. *Phys Lett A* **91**, 355-357 (1982).
33. X. X. Yang, Z. H. Dai, Y. C. Zhao, J. Y. Liu, S. Meng, Low lattice thermal conductivity and excellent thermoelectric behavior in Li_3Sb and Li_3Bi. *J Phys-Condens Mat* **30**, 425401 (2018).
34. S. Lee, K. Esfarjani, J. Mendoza, M. S. Dresselhaus, G. Chen, Lattice thermal conductivity of Bi, Sb, and Bi-Sb alloy from first principles. *Physical Review B* **89**, 085206 (2014).
35. Q. S. Li *et al.*, Temperature dependent thermal conductivity and transition mechanism in amorphous and crystalline Sb_2Te_3 thin films. *Sci Rep-Uk* **7**, 13747 (2017).
36. T. Caillat, J. P. Fleurial, A. Borshchevsky, Preparation and thermoelectric properties of semiconducting Zn_4Sb_3. *J Phys Chem Solids* **58**, 1119-1125 (1997).
37. X. D. Li, J. Carrete, J. P. Lin, G. J. Qiao, Z. Wang, Atomistic origin of glass-like Zn_4Sb_3 thermal conductivity. *Applied Physics Letters* **103**, 103902 (2013).
38. H. Wu, Y. Cui, Designing nanostructured Si anodes for high energy lithium ion batteries. *Nano Today* **7**, 414-429 (2012).

CHAPTER 6: CONCLUSIONS AND PERSPECTIVES

6.1. SUMMARY

In summary, I have shown novel thermal switching materials (TSMs) that can change their thermal conductivity states in response to external stimuli, such as magnetic fields, electromagnetic waves and electrochemical reaction with Li^+ ions. These external stimuli caused physical and chemical property transitions, resulting in atomic and molecular-level transitions associated with thermal conductivity switching between high (Λ_{high}) and low (Λ_{low}) states. Throughout the dissertation, I presented thermal conductivity switching of (i) liquid crystal networks (LCNs) by controlling their mesogen group alignments by magnetic field, (ii) azopolymers by modulating interchain π-π bonding strength by light, and (iii) Li-ion battery electrode materials (Fe_2O_3, NiO, TiO_2, V_2O_5 and Sb) by electrochemical reactions with Li^+ ions.

In Chapter 3, I reported thermal switches based on the control of molecular ordering of liquid crystal networks (LCNs) by a magnetic field. I presented the structure-property relationship connecting the thermal conductivity and the molecular orientation of LCNs with $r = \Lambda_{high}/\Lambda_{low} = 1.5$ and $\Lambda_{high} = 0.34$ W m^{-1} K^{-1} and $\Lambda_{low} = 0.22$ W m^{-1} K^{-1}. This thermal conductivity switching is based on the alignment of the mesogen groups controlled by a magnetic field at above the glass transition temperature (65 ^{o}C) over the switching time τ = 10 min. The switching time is highly dependent to the reorientation kinetics with the relaxation time ~ $2\mu_0\eta/\Delta\chi B^2$, where μ_0 is permeability of vacuum, η is the rotational viscosity, $\Delta\chi$ is the anisotropy of the magnetic susceptibility of the mesogen, and B is the applied magnetic field.

Since the limiting factor for thermal switching is the viscous drag against the collective rotation of mesogen units, I designed a much faster thermal switching system by introducing light-sensitive azobenzene groups to polymer chains (azopolymer) in Chapter 4. The *cis*-*trans* photoisomer transition of azobenzene moieties triggered an unprecedented reversible crystal-to-liquid phase transition of azopolymer under ultraviolet (UV) and green light. The azopolymer showed $r \approx 3.5$ with $\Lambda_{high} = 0.35$ W m^{-1} K^{-1} and $\Lambda_{low} = 0.10$ W m^{-1} K^{-1}. This 3.5-fold thermal conductivity change is attributed to a spontaneous chain alignment modulated by the interchain π-π network transitions. The high thermal conductivity state of the crystalline phase resulted from the formation of well-ordered lamellar and spontaneous alignment of π-π stacked *trans*-azobenzene groups under ambient condition. The low thermal conductivity state was driven by the melting of the *cis*-azobenzene polymer where UV irradiation reduced the strength of the interchain π-π network. Subsequent exposure to green light restored the crystalline order and high thermal conductivity at $\tau = 10$ seconds at room temperature.

In Chapter 5, I described thermal conductivity and elastic modulus change of five Li-ion battery electrode materials. The thermal conductivity of the electrode materials significantly changed with respect to the Li^+ ion contents, the number of charge/discharge cycles and the electrochemical reaction mechanisms: conversion, intercalation and alloying. Conversion electrodes exhibited a volume change of 200 % along with the formation of solid electrolyte interphase (SEI) passivation layer and the irreversible amorphization during the first lithiation caused by Li-ion induced lattice disordering. These structural degradations resulted in a significant, irreversible thermal conductivity loss of $r = 2.5$ (NiO) and 7.5 (Fe_2O_3). After the first lithiation, the thermal conductivity of NiO and Fe_2O_3 remained almost constant regardless of Li^+ ion content.

On the contrary, intercalating TiO_2 and V_2O_5 electrodes showed a reversible thermal switching performance ($r \approx 1.6–1.8$,) up to 5 cycles without loss of the crystalline structure. Interestingly, the largest $r \approx 20$-30 was observed for the alloying Sb electrode between the semimetal (Sb) to semiconductor (Li_3Sb) states for a limited number of cycles. To the best of my knowledge, this is the highest value reported among thermally switching materials. All electrode showed a thermal switching on τ = 1–2.5 hours (C-rate: 0.2–1 C). By subjecting Sb to a limited discharge capacity ($Li_{1.38}Sb$), I observed enhanced cyclability with reversible thermal switching property. Figure 6.1 summarizes the thermal conductivity contrast r and the low thermal conductivity states (mostly lithiated) of electrode materials. As $\Delta\Lambda = (1-r)\Lambda_{low}$, the solid diagonal guidelines in Figure 6.1 help to understand the absolute thermal conductivity changes of each electrode. Intercalating $LiCoO_2$ (*1*), black phosphorous (Li_x-P) (*2*) and bulk and thin MoS_2 (*3*) were plotted for comparison as well.

In conclusion, I presented novel thermal switching materials that exhibited a wide range of thermal switching properties: from the lowest thermal conductivity Λ_{low} = 0.1 W m^{-1} K^{-1} (*cis*-azopolymer), to the highest thermal conductivity Λ_{high} = 18 W m^{-1} K^{-1} (for Sb); from the lowest r = 1.5 (LCNs), to the highest r = 30 (Li_xSb); and from the fastest τ = 10 seconds (*cis-trans* azopolymer transition), to the slowest τ = ~ hours (Li-ion electrode materials with 0.2 C-rate). Figure 6.2 summarizes thermal switching ratio r and switching rate τ^{-1} of thermal switching materials. Note that the thermal switching performance, Q, the normalized thermal conductivity change $\Delta\Lambda/\Lambda_{low}$ at a given time Δt, is defined as

$$Q = \frac{\Delta\Lambda}{\Lambda_{low}}\frac{1}{\Delta t} = \frac{r-1}{\tau} \tag{6.1}$$

The solid diagonal lines in Figure 6.2 provide a guideline to compare the thermal switching performance of each TSMs. For example, azopolymer lies above the line $Q = 10\ s^{-1}$, suggesting that the azopolymer can change the thermal conductivity more than 100% per second while intercalating TiO_2 and $LiCoO_2$ lie on the line $Q = 10^4\ s^{-1}$, indicating that they exhibit thermal conductivity change of ~1% per second.

6.2 PERSPECTIVE OF THERMAL SWITCHING MATERIALS

Contrary to traditional materials having inherently immutable thermal properties, TSMs are novel materials that can change their thermal conductivities responding to external stimuli, such as electric and magnetic fields, and electromagnetic waves. I have shown examples of effective control of the thermophysical properties of polymers and Li-ion battery electrodes which show structural changes in electronic, atomic and/or molecular levels associated with the thermal conductivity. These results could provide insight for the interpretation of preceding studies on thermal properties of materials, broadening our understanding of TSMs for the advance in electronics, material science, and other fields of study.

Possible applications of thermal switching polymers are micro-thermal switches, which can focus cooling power on critical hot spots and enable thermal routing in the device, and thermal energy storage system utilizing the conversion of thermal energy. Study on thermal switching Li-ion battery electrode materials could help to build a database of dynamic thermal properties of electrode materials under electrochemical cycling, providing electrochemical and other pivotal thermo-physical properties of various Li-ion battery electrode materials. Prediction based on the database could offer valuable insights for designing Li-ion batteries with enhanced

thermal management capacity, minimizing any potential problems related to thermal runaway (exothermic breakdown) of Li-ion batteries (*4-7*).

6.3 FIGURES

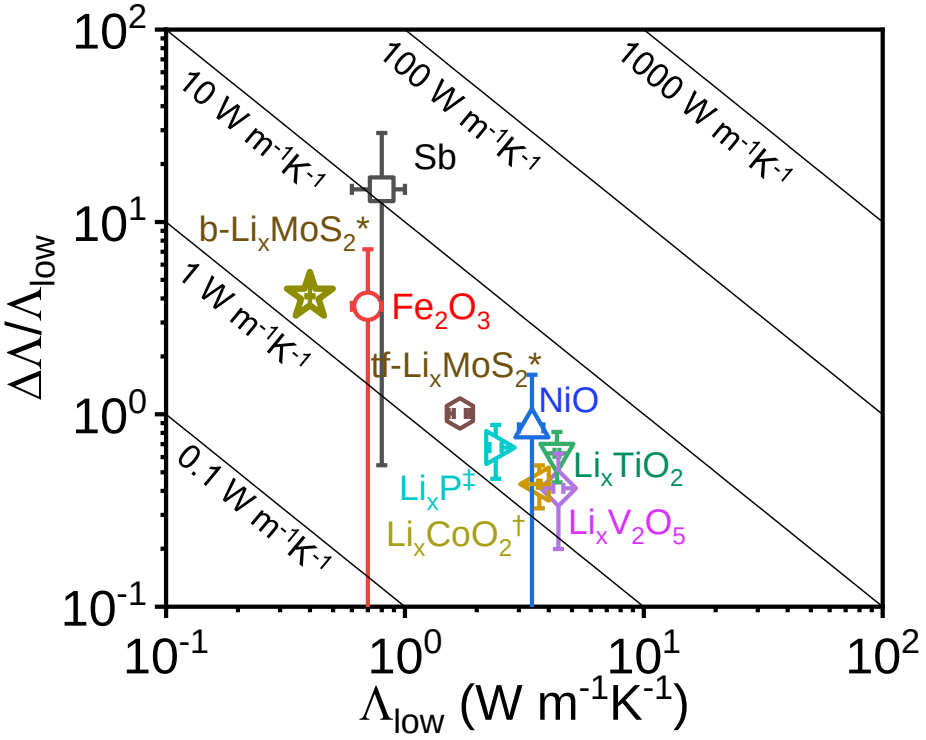

Figure 6.1. Thermal conductivity of the low thermal conductivity state (Λ_{low}) and the switching ratio (r) of the electrode materials. Reference data from †$LiCoO_2$(*1*), ‡Li_xP(*2*) and *MoS_2 (*3*). The solid diagonal lines are contour lines with the absolute thermal conductivity changes, $\Delta\Lambda = \Lambda_{high} - \Lambda_{low}$.

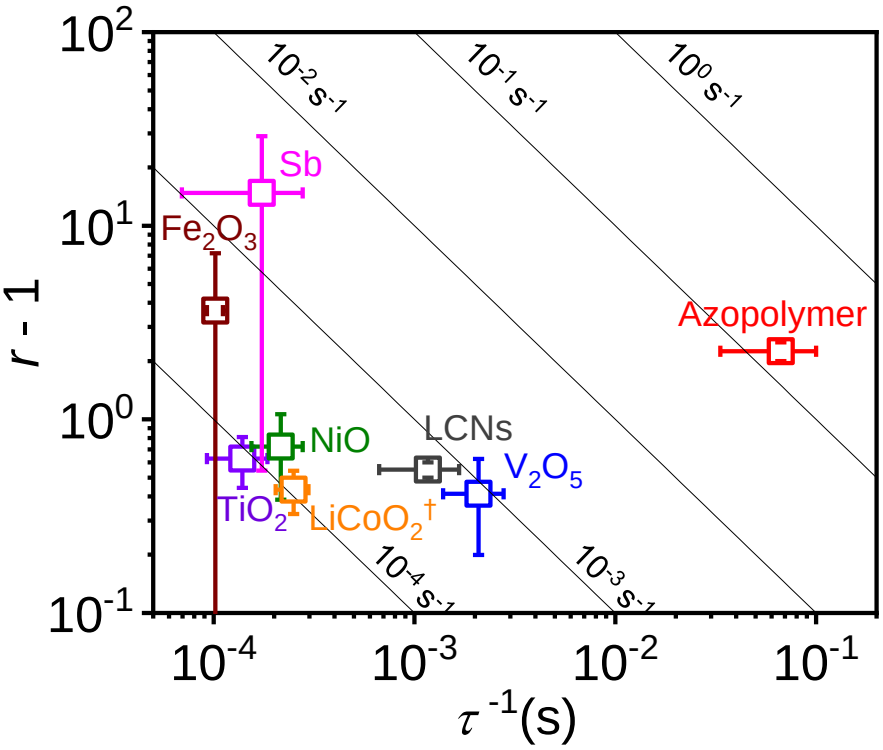

Figure 6.2. Thermal conductivity switching ratio (r) and switching rate τ^{-1} of TSMs studied in this dissertation. The solid diagonal lines are contour lines with the thermal switching performance, $Q = (\Delta\Lambda/\Lambda_{low})\cdot\tau^{-1}$, which is the ratio of thermal conductivity change per second.

6.4 REFERENCES

1. J. Cho *et al.*, Electrochemically tunable thermal conductivity of lithium cobalt oxide. *Nat Commun* **5**, 4035 (2014).
2. J. S. Kang, M. Ke, Y. J. Hu, Ionic Intercalation in Two-Dimensional van der Waals Materials: In Situ Characterization and Electrochemical Control of the Anisotropic Thermal Conductivity of Black Phosphorus. *Nano Lett* **17**, 1431-1438 (2017).
3. G. H. Zhu *et al.*, Tuning thermal conductivity in molybdenum disulfide by electrochemical intercalation. *Nat Commun* **7**, 13211 (2016).
4. M. L. Hao, J. Li, S. Park, S. Moura, C. Dames, Efficient thermal management of Li-ion batteries with a passive interfacial thermal regulator based on a shape memory alloy. *Nat Energy* **3**, 899-906 (2018).
5. Q. S. Wang *et al.*, Thermal runaway caused fire and explosion of lithium ion battery. *J Power Sources* **208**, 210-224 (2012).
6. D. R. Doughty, E. P., A General Discussion of Li Ion Battery Safety. *Electrochem. Soc. Interface* **21**, 37-44 (2012).
7. P. G. Balakrishnan, R. Ramesh, T. P. Kumar, Safety mechanisms in lithium-ion batteries. *J Power Sources* **155**, 401-414 (2006).

APPENDIX A. THERMAL CONDUCTIVITY LIMIT OF THERMALLY SWITCHING POLYMERS

In Chapter 3 and 4, I presented thermal conductivity switching of liquid crystal networks (LCNs) and azobenzene-functionalized polymer (azopolymer). These thermal switching polymers showed thermal conductivity switching near the lower limit of polymers (Λ_{low} = 0.1 – 0.2 W m^{-1} K^{-1}). Therefore, the effective way to enhance *r* is to achieve higher thermal conductivity at the high thermal conductivity state (Λ_{high}). So far, the observed *r* and Λ_{high} of LCNs and azopolymer ≈ 1.5–3.5 are similar to thermal conductivity changes of polydomain *n*-alkanes with comparable lengths (*n* = 9 ~ 19) with $r \approx 2 \sim 3$ (Λ_{high} ~ 0.4 W m^{-1} K^{-1}) during melting transition (*A1, A2*).

With a larger order parameter *S* and smaller isotropic component fraction *Φ*, I expect that *r* could be as high as 100, which is the anisotropic thermal conductivity ratio ($\Lambda_{in\text{-}plane}/\Lambda_{ouf\text{-}of\text{-}plane}$ of polymer fibers(*A3, A4*). However, polymer fibers with the high order parameter (*S* > 0.9) would expense chain mobility, resulting in poor kinetics at room temperature. Practical improvement of *r* could be achieved by a nonthermal solid-liquid phase transition from thermally insulating liquid phase to thermally conducting solid (crystalline) phase, which enables physical displacement and rearrangement of molecules at the liquid phase at a reasonable time scale. So far, Azopolymer is the only system allowing this solid-liquid phase transition at tens of second.

In collaboration with Xingfei Wei and Dr. Tengfei Luo at the University of Notre Dame, we used molecular dynamics (MD) to simulate the theoretical thermal conductivity limit of azopolymer and compared with the effective medium theory(*A5*). MD predicts the thermal conductivity in the side-chain direction of azopolymer crystal as 0.51 W m^{-1} K^{-1}, which is

consistent with the thermal conductivity of azopolymer crystal ($\Lambda_{crystal}$ = 0.48 W m^{-1} K^{-1}) without defects or amorphous phase (Φ = 0). The theoretical thermal conductivity of azopolymer crystal is calculated as (see Chapter 3.5)

$$\Lambda_{crystal} = \frac{\phi}{\Lambda^{-1} - (1-\phi)\Lambda_{amorphous}^{-1}} \quad (A.1)$$

where Λ = 0.35 W m^{-1} K^{-1}, $\Lambda_{amorphous}$ = 0.19 W m^{-1} K^{-1} (see Chapter 4.5) and Φ = 76 % determined by polarized optical microscopy (POM) images of azopolymer spherulites.

A.1. REFERENCES

A1. V. A. Konstantinov, Heat Transfer in Molecular Crystals. *Heat Transfer - Theoretical Analysis, Experimental Investigations and Industrial Systems*, 157-188 (2011).

A2. C. Velez, M. Khayet, J. M. O. de Zarate, Temperature-dependent thermal properties of solid/liquid phase change even-numbered n-alkanes: n-Hexadecane, n-octadecane and n-eicosane. *Appl Energ* **143**, 383-394 (2015).

A3. X. J. Wang, V. Ho, R. A. Segalman, D. G. Cahill, Thermal Conductivity of High-Modulus Polymer Fibers. *Macromolecules* **46**, 4937-4943 (2013).

A4. Y. Lu, J. Liu, X. Xie, D. G. Cahill, Thermal Conductivity in the Radial Direction of Deformed Polymer Fibers. *Acs Macro Lett* **5**, 646-650 (2016).

A5. X. F. Wei, T. Zhang, T. F. Luo, Chain conformation-dependent thermal conductivity of amorphous polymer blends: the impact of inter- and intra-chain interactions. *Phys Chem Chem Phys* **18**, 32146-32154 (2016).